Di-muon measurements for the development of muon chamber and particle production in the CBM experiment at FAIR

THESIS SUBMITTED FOR THE AWARD OF THE DEGREE

OF

Doctor of Philosophy

In

Physics

by

Arun Prakash

Supervisor

Prof. B. K. Singh

Nuclear Physics Section

Department of Physics

Banaras Hindu University

Varanasi-221005

India.

Enrollment No. 301772 June 2014

DEPARTMENT OF PHYSICS
BANARAS HINDU UNIVERSITY
VARANASI - 221 005, INDIA

UNDERTAKING

I hereby declare that I have completed the research work for the full time period prescribed under the clause VIII.1 of the Ph.D. ordinances of the Banaras Hindu University, Varanasi and that the research work embodied in this thesis entitled **"Di-muon measurements for the development of muon chamber and particle production in the CBM experiment at FAIR"** is my own research work.

Date: (Arun Prakash)

ANNEXURE - E

CANDIDATE'S DECLARATION

I, **Arun Prakash**, certify that the work embodied in this Ph.D. thesis is my own bonafide work carried out by me under the supervision of Prof. B. K. Singh for a period of October 2008 to June 2014 at Banaras Hindu University. The matter embodied in this Ph. D. thesis has not been submitted for the award of any other degree/diploma.

I declare that I have faithfully acknowledged, given credit to and referred to the research workers wherever their works have been cited in the text and the body of the thesis. I further certify that I have not willfully lifted up some other's work, para, text, data, results, etc. reported in the journals, books, magazines, reports, dissertations, theses, etc., or available at web-sites and included them in this Ph. D. thesis and cited as my own work.

Date:

Place: Varanasi

(Arun Prakash)

Certificate from the Supervisor

This is to certify that the above statement made by the candidate is correct to the best of my knowledge.

Prof. S. B. Rai
(Head of the Department)

Prof. B. K. Singh
(Supervisor)

ANNEXURE - F

PRE-SUBMISSION SEMINAR COMPLETION CERTIFICATE

This is to certify that Mr. **Arun Prakash**, a bonafide research scholar of this department, has satisfactorily completed the pre-submission seminar requirement which is a part of his Ph. D. programme.

Date: (Head of the Department)

ANNEXURE G

COPYRIGHT TRANSFER CERTIFICATE

Title of the Thesis: **Di-muon measurements for the development of muon chamber and particle production in the CBM experiment at FAIR**

Candidate's Name: **Arun Prakash**

Copyright Transfer

The undersigned hereby assigns to the Banaras Hindu University all rights under copyright that may exist in and for the above thesis submitted for the award of the Ph. D. degree.

(Arun Prakash)

Dedicated

to

My Family

Acknowledgements

During the past six years I have had a chance to work with many people; with some I collaborated during a limited amount of time, others have accompanied me over the whole tenure of my PhD. To all of them I just want to say Thank You !, for a wonderful time and experince I had during my PhD tenure. The PhD tenure of any student starts with his/her supervisor, I am also no exception. I start by addressing a few words to Prof. Dr. Bhartendu Kumar Singh, who supervised me over all these years and consciously guided the various steps during my PhD. I have never ever seen somebody as patient, helpful, constructive and motivating as him. Through his fine sense of communicating with people he manages to always keep an excellent atmosphere within (and also outside) our group. I can only express my sincere thanks to him.

I would like to acknowledge Prof. C. P. Singh, for his generous support and encouragement. I am very much indebted to him for his constant motivation and deep insights and knowledge in the subject. I would like to extend my thanks for his patience with which he dealt me and his critical remarks and valuable suggestions are appreciated. I take this opportunity to express my sincere thanks to Prof. S. B. Rai, Head of the Department, for providing me all the necessary facilities available in the department during my research work. I would also like to thank Prof. R. P. Malik, Prof. B. P. Mandal and Dr. V. Singh for their moral support.

During first few months I had an oppurtunity to visit VECC, Kolkata for CBM simulation workshop where I had a chance of meeting Dr. S. Chattopadhyay. My first impression was that he is student friendly person.The first job he assigned me was

installation of CBM simulation package. I learnt more about the simulation from the infinite knowledge and experience of Dr. Premmoy Ghosh, Scientific Officer, VECC, Kolkata and Partha Pratim Bhaduri, Scientific Officer, VECC, Kolkata. In course of time I visited VECC, Kolkata frequently and worked with Dr. S. Chattopadhyay. He is really a very good teacher, as cool as cucumber, excellent motivator. He always used to help me when I got stuck up in the C++ codes. Also he devoted his valuable time and effort making me understand the basics of particle detectors, heavy-ion collision physics, and analysis of test beam data. I take this oppurtunity to thank him and really "hats off " to such a person. Thanks for your valubale time and the efforts put in for the guidance. I would also like to express my indebtness and gratitude to Partha Pratim Bhaduri, VECC Kolkata for the discussions on the simulations. I also wish to thank Pritwish Tribedy, Scientific Officer, VECC, Kolkata in helping me with the C++ codes.

I also wish to thank Dr. Tapan Nayak Scientific Officer, VECC, Kolkata for constantly motivating me whenever I visited VECC, Kolkata. I wish to thank Dr. Jane Alam, Scientific Officer, VECC, Kolkata for his wonderful lecture series on CBM physics during early days of my PhD. I wish to thank Dr. Bedangadas Mohanty, Associate Professor and Chairman SPS, NISER, Bhubaneswar for the fruitful discussions on CBM physics, experimental techniques on particle physics. I also thank Dr. S. Biswas, Scientific Officer, NISER, Bhubaneswar for his valubale time and discussions on Gas Electron Multiplier detectors. I thank S. Muhri, Scientific Officer, VECC, Kolkata for the help which he extended whenever I was at Kolkata.

I had the pleasure to work with Dr. Anand Kumar Dubey, Scientific Officer, Variable Energy Cyclotron Centre, Kolkata. He helped me to understand the working principle of Gas Electron Multiplier and also on several ocassions I had the oppurtunity for a "hands-on" testing of Gas Electron Multiplier. I really have no words to express my feeling towards him. We had several debates and discussions on the test beam data of CERN-SPS and COSY-Juelich.

I had the oppurtunity to work with Mr. Ram Narayan Singaraju , Scientific Officer, VECC, Kolkata. I learnt lot of electronics from him. Also he assisted me in connecting the required electronics to Gas Electron Multiplier and further we had lot of discussions on the test beam data of CERN-SPS and COSY-Juelich. I am again grateful and thankful to him for his time and valuable advise. I thank J. Saini for the cordial help pertaining to nXYTER and ROC's.

I am grateful to colleagues of CBM collaboration who helped me all throughout my PhD. I thank Peter Senger (Spokesperson of CBM Collaboration),Volker Friese, Ana Senger, Johann Heuser, Florian Uhlig, W. F. J. Muller, Ivan Kisel, Iouri Vasliev, Claudia Hohne, Juergen Eschke, all from CBM collaboration who have helped me at various stage of my PhD. tenure.

I am very grateful to my co-research fellows Mr. Prashant Kumar Srivatava,Mr. Swatantra Kumar Tiwari, Mr. Ashwini Kumar, Mr. Prakhar Garg and Mr.Triloki for their active participation at various stages of my research investigation. I am also thankful to all my fellow friends for being with me in all the good and bad times we had together.

I would also like to thank the organizers of different schools/ conferences/ symposia/ workshops, that I have attended during my research period, for providing me an opportunity to interact with experts of my field and present my research ideas in front of national and international physics community.

I apologise to all whom I have not mentioned. I acknowledge Department of Science and Technology, India , Council for Scientific and Industrial Research, India for having funded most of the present research work. The financial help from Variable Energy Cyclotron Centre, Kolkata is duly acknowledged. The financial help from the CBM collaboration through Prof. Dr. P. Senger to cover my stay at GSI is highly appreciated.

Finally I have no words to thank my family members specially my parents, for their unconditional love, care and patience. Without their blessings and support, this

work could have never been materialized. I am really thankful and indebtful to my elder sisters who have mentally supported me during my PhD.

(Arun Prakash)

Declaration

This dissertation is the result of my own work and includes nothing which is the outcome of work done in collaboration except where specifically indicated in the text. No part of this thesis has previously been submitted for a degree or other qualification at this or any other university.

This thesis is based on the following research papers:

1. *Particle Production at CBM in a Thermal Model Approach*
   A. Prakash, P. K. Srivastava, B. K. Singh
   Advances in High Energy Physics. **2014**, 983861 (2014).

2. *GEM detector development for CBM experiment at FAIR*
   A. K. Dubey, **A. Prakash**, S. Chattopadhyay, M. S. Ganti , R Singaraju, J. Saini, B. K. Singh, Y. P. Viyogi
   Nucl. Inst. and Meth. A **718**, 418-420 (2013).

3. *Di-muon measurements in CBM experiment at FAIR*
   A. Prakash, P. P. Bhaduri, S. Chattopadhyay, A. Dubey, B. K. Singh
   Nuclear Physics A. **862-863**, 493-496 (2011).

Arun Prakash

Banaras Hindu University

June 2014

Preface

The Facility for Antiproton and Ion Research (FAIR) is an accelerator complex under construction near the Gesellschaft Schwerionen (GSI) research centre in Darmstadt, Germany. Its backbone are two superconducting synchrotons (Schwerionen Synchrotron (SIS)-100 and SIS-300) with 100 and 300 Tm bending power respectively, delivering high intense beams of protons (upto 90 GeV), light ions (upto 45 GeV per nucleon) and heavy ions (up to 35 GeV per nucleon). The Compressed Baryonic Matter (CBM) experiment is being constructed to be operated at this facility from 2018. It will investigate nuclear matter under extreme conditions (temperature, density) as produced in relativistic nuclear collisions. The collision energies available with the SIS-100 and SIS-300 accelerators will provide access to the high-density regime of the phase diagram of strongly interacting matter. CBM will search for the landmarks of this phase diagram as predicted by theory, namely the onset of the transition from confined to deconfined matter, the critical point and onset of chiral symmetry restoration. The CBM physics programme is complementary to the heavy-ion research conducted at Relativistic Heavy Ion Collider (RHIC), USA and Large Hadron Collider (LHC), Switzerland, which explore Quantum Chromodynamics (QCD) matter at high temperatures but at almost vanishing net-baryon density. The emphasis of CBM will be the measurement of rare probes giving access to the early stage of the collisions, like charmed hadrons (J/ψ), multi-strange hyperons and leptonic decays of low mass vector mesons (ρ, ω, ϕ). As the expected multiplicities of these observables are extremely low, their measurement requires high interaction rates, which drive the experimental requirements. Consequently, CBM is being designed to cope with the collision rates of up to 10 MHz, unprecedented in heavy-ion experiments so far. Such rates call for a fast and radiation hard detectors and read-out electronics, but also constitute challenges for the data acquisition, online data reduction and processing. The experiment will operate in fixed-target mode and measure charged hadrons, electrons and muons as well as photons.

The plan of thesis is structured as follows :

Chapter 2 starts with the general introduction to the CBM experiment at FAIR. The measurements of bulk hadrons, multistrange hyperons, hypernuclei, charmonium and low mass vector mesons in nuclear collisions requires a large acceptance, high rate detector system. The proposed detectors of this experiment are Silicon tracking System (STS), Micro Vertex Detector (MVD), Time of Flight (TOF) detector, Ring Imaging Cherenkov (RICH) detector, Transition Radiation Detector (TRD) , Muon Chamber (MUCH), Electromagnetic Calorimeter (ECAL) and Projectile Spectator Detector (PSD).

The STS will measure the trajectories of the produced particles in the magnetic dipole field, determine their momenta and reconstruct it. MVD will be used for the high precision measurement of the decay vertices of the charmed hadrons. TOF consisting of multi-gap resistive plate chambers will help in identification of pions, kaons and protons. RICH will serve for identification of electron-positron pairs from the decay of low mass vector mesons. TRD will be used to match tracks reconstructed in the STS to the TOF measurement. MUCH will be used for detection of muons from charmonium and low mass vector mesons. ECAL for the measurement of photons from low mass vector mesons. PSD for the determination of the collision centrality and the reaction plane by the measurement of projectile spectators.

Chapter 3 starts with the introduction to the Muon Chamber (MUCH). One of the important aspects of the CBM experiment is to look for rare probes like charmonia (J/ψ,ψ' etc.) having extremely low production cross section in the FAIR energy regime. Charmonia as well as low mass vector mesons (ρ, ω, ϕ) can be measured via their decay in di-muons. Thus a Muon Chamber is needed to detect these dimuons. The MUCH system consists of six alternating layers of absorbers and triplets of tracking chambers.

The first few tracking chambers will be of Gas Electron Multiplier (GEM) detectors. Simulations were performed for the optimization of the detector design and to study the feasibility of the di-muon measurement. The feasibility studies are done within the CBM simulation framework which allows full event simulation and reconstruction. The ingredients used for the simulation are : a) PLUTO generator for phase space decay of the vector mesons taking multiplicities from HSD. b) UrQMD generator for background particles. c) GEANT3 for transport of the generated particles through the setup. d) Kalman Fitter (KF) for tracking. The detection procedure involves the reconstruction of the track parameters in STS and extrapolation to muon detecting stations through the absorbers. Selection of the number of muon stations decides the identification of muons from low mass vector mesons (LMVM) and charmonia. While the LMVM muons travel shorter distances, J/ψ muons cross the thick absorber and reach till the end. We have therefore taken tracks travelling through 15 layers and 18 layers as valid muon candidates from LMVM and charmonia respectively. Our studies indicate that both low mass vector mesons and charmonia can be identified above the combinatorial background which is dominated by muons from weak pion decays.

Chapter 4 starts with the introduction to Gas Electron Multiplier (GEM) detector. A large acceptance, high-granularity and high rate muon detection system (MUCH) is proposed to be built in the CBM experiment for carrying out the measurements of charmonium(J/Ψ) and low mass vector mesons by their muonic decay channels in high energy heavy ion collisions. Current design of the muon system consists of six sets of alternating layers of absorbers and detector triplets. For the first few stations, where the particle rates reach 1 MHz/cm^2, GEM based detectors are being developed as tracking chambers. The advantage of using the GEM are: The detector should be able to cope up with a high collision rate of $\sim$ 10 MHz. This high luminosity facilitates the measurement of rare probes mentioned above. Detector granularity should be high to cater to a hit of about 1 hit/ cm^2. The detector should be resistant to high dose of neutrons,

photons and heavy ions. Large acceptance detector should have modular arrangement. Collecting data in a self triggered mode, which is the data taking mode for all CBM detectors. Several technology options have been considered. Owing to a harsh radiation environment and large size of the chambers required option of using silicon detectors for MUCH would not be practicable. Use of detectors based on semiconductor technology is also not a suitable option as ageing can be a serious issue due to high luminosity. Gas based detectors are most suited for this purpose. However, the conventional wire chambers cannot cope up with the specified high rates, as the gain is known to drop at such high rates. Gas detectors based on micropattern technology, i.e. GEM (Gas Electron Multiplier), THGEM and micromegas are known to have stable gains at high rates. GEM based detectors are already employed or being implemented in many high energy physics experiments such as COMPASS, HBD, LHCb, CMS.
The testing of GEM's at CERN-SPS H4 beam line area with muon beams will be discussed. The GEM detectors performance in terms of efficiency, number of cells fired and gain will also be discussed.

Chapter 5 deals with the study of particle production mechanism at CBM energies using different models such as statistical thermal model and transport models.The main motivation of this study is to show what one should expect in context to particle multiplicities and particle ratios at CBM energy range i.e. 10 A GeV to 40 A GeV lab energies (4.43 GeV to 8.71 GeV center-of-mass energies) , in view of equilibrated statistical as well as transport models. We have also compared the model results with available experimental data of Alternating Gradient Synchrotron (AGS) and Super Proton Synchrotron (SPS) energies.

The Compressed Baryonic Matter (CBM) experiment planned at Facility for Antiproton and Ion Research (FAIR) will provide a major scientific effort for exploring the properties of strongly interacting matter in the high baryon density regime. One of the important goal behind such experiment is to precisely determine the equation of state

(EOS) for the strongly interacting matter at extreme baryon density. We have employed a thermal model EOS incorporating excluded volume description for the hot and dense hadron gas (HG) for our study. We then predict different particle ratios and the total multiplicity of various hadrons in the CBM energy range. Our main emphasis is to estimate the strange particles enhancement as well as increase in the net baryon density in CBM experiment. We have also compared our results with the results obtained from various other theoretical approaches existing in the literature such as hadron string dynamics (HSD) model and ultra-relativistic quantum molecular dynamics (UrQMD) etc.

In **Chapter 6**, we present a summary and conclusion drawn from this work and provide some insights in this area for future research work.

Contents

Figures

Tables

Chapter 1

Introduction

The strong interaction is one of the basic force of nature which plays a crucial role in the evolution of the universe and in the synthesis of elements. Strongly interacting matter constitutes 99 % of the visible mass in our world. The fundamental theory describing the mutual strong interactions of quarks, gluons and antiquarks is Quantum Chromodynamics (QCD) [1]. Quantum Chromodynamics (QCD) a non-abelian gauge theory describes the dynamics of quarks and gluons. It exhibits a remarkable property that the interaction between two particles, quarks and gluons, becomes weak as the separation between them is reduced. This phenomenon is known as "asymptotic freedom" [2, 3]. Another salient feature is that at large distances, comparable to the size of nucleon, the interaction between two quarks becomes strong. This phenomenon is known as "confinement", the fact that only hadrons are observed while isolated quarks and gluons are not. The origin of hadron mass is still unsettled till date. The masses of up and down quarks the main constituents of the visible matter are very small when viewed at a short distance scale. The proton for example, is roughly 50 times heavier than the sum of the masses of its three basic constituents, the up and down quarks. A quantitative understanding of this enormous mass generation within QCD has not yet been achieved.

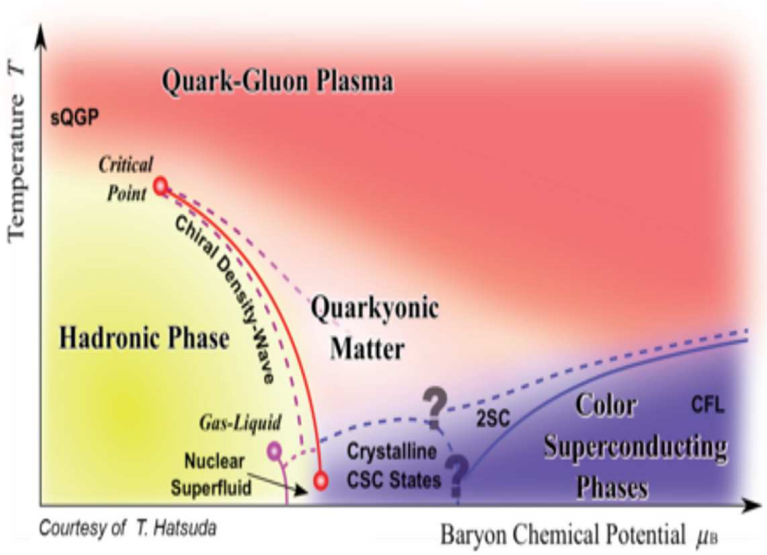

Figure 1.1. Conjectured phase diagram of strongly interacting matter [4]

1.1 Phase diagram of strongly interacting matter

A conjectured phase diagram of QCD matter is shown in Fig. 1.1 in the plane of temperature T and baryo-chemical potential μ_B [4]. Based on the fundamental property of asymptotic freedom, one expects at least three different regions: the hadronic phase (at low μ_B and low T), the quark gluon plasma QGP (at high T) [1] and the color-superconducting region (at high μ_B , low T). For high temperatures and/or high baryon densities, we expect a deconfined phase. Possible phases and the precise location of the phase transitions and critical points are currently studied also from a theoretical side. Theoretically, a first-order phase transition is expected at high baryon densities and low temperatures. In general, first-order phase transitions exhibit a discontinuity in the first derivative of the free energy with respect to a thermodynamic variable. The phase coexistence curve between the hadron gas and QGP may end in a critical point, in which the phase transition is of second order. The existence as well as the exact position of the critical point in the phase diagram are currently being debated. Recent lattice

QCD calculations predict the phase transition in the region of highest temperature to be neither of first nor of second order. In this region, it is expected that variables like the energy density change quickly but continuously in the vicinity of T_c . Thus, a transition in this region is called crossover [5]. Since the existence of the critical point and of a first-order phase transition are not yet confirmed, the phase transition may also remain a crossover all along. Depending on the curvature of the critical surface in the μ - m_u, d - m_s space (with the quark masses m_u , m_d , m_s and the quark density μ), a QCD chiral critical point may be present or not [6]. While the theoretical assumptions are still ambiguous, it is widely accepted that given the existence of a first-order phase transition at finite baryon density terminating in a critical endpoint, a crossover is expected at $\mu_B = 0$. At very high densities and very low temperatures, correlated quark-quark pairs (Cooper pairs) are predicted to form a color superconductor [7]. This color- superconductive phase has already been conjectured early in the study of quark matter [8]. The transition from a hadron gas to a QGP is also interesting for cosmology and astrophysics. Today it is believed that in the Big Bang scenario for the origin of the universe the elementary particles were produced in the freeze-out from a QGP phase with high temperature and low baryon density around 1 μs after the Big Bang. Furthermore, it can be seen in the phase diagram that a phase transition to the QGP, or even to more exotic states of matter at zero temperature, is expected for large baryon densities. It is assumed that these densities are reached in the center of neutron stars [9]. Here, the possible super conducting phase and the QGP can play an important role in the stability of neutron stars. In this context, it might even be possible to use astrophysical observations to rule out or confirm expected phases [10]. Almost the entire μ_B region can be explored by varying the collision energy of the colliding nuclei.

1.2 Relativistic Heavy Ion Collisions

A challenging field of modern physics is the investigation of nuclear matter under extreme conditions and the exploration of the phase diagram of strongly interacting matter with high-energy nucleus-nucleus collisions. Classical experiments for investigating the atomic structure, e.g. via excitation with electron collisions, require typical energies of a few eV. For the examination of the next smaller units, the atomic nuclei, already energies of some MeV are required. With increasing energies even smaller dimensions can be explored. This relation can be understood through the uncertainty principle of Heisenberg:

$$\Delta p_x \, \Delta x \approx \hbar \tag{1.1}$$

Consequently, probes with a minimum momentum of p $\approx \hbar/\Delta$l are required to resolve the structures of the size Δl. Therefore, very high particle energies are necessary for elementary particle physics to resolve the structure of matter. Dense matter with properties similar to those in nucleus-nucleus collisions is expected to have existed in the early universe until about 10 μs after the Big Bang. In order to study the bulk properties of that matter the largest possible volume of that matter is required. It is important to understand its collective behavior and not only point-like interactions. That is why the study of high-energy collisions of the heaviest nuclei is preferred to the investigation of more elementary systems like interactions of protons and leptons. Up to now, the largest physical systems studied in the laboratory are collision systems of lead (Pb) and gold (Au). Besides Pb and Au, the future Facility for Antiproton and Ion Research (FAIR) [11] will also accelerate uranium (U) ions (see Chapter 2), which are even heavier, but the non-spherical shape of these ions exacerbates the production of central collisions and the determination of the collision centrality. When atomic nuclei collide at very high energies, such that the kinetic energy exceeds significantly their rest energy, dense hadronic matter is produced. In such relativistic heavy-ion collisions, the energy density of hadronic matter typically exceeds a value of $\epsilon = 1 \; GeV \; fm^{-3} = 1.8 \times 10^{15} \; g \; cm^{-3}$

, and the corresponding relativistic matter pressure is P $\simeq$ 1/3 ϵ = 0.52 x 10^{30} bar [12]. Although genuine phase transitions are not expected to develop in finite physical systems, it is possible to experimentally explore the properties of the phase transition involving the dissolving of hadronic particles. The reason for this is that relativistic systems are investigated in which the ability to produce particles from energy and the presence of virtual fluctuation effects greatly enhance the number of physical states accessible. Hence, it is possible to identify a phase transition from the nuclear, hadronic phase to a matter phase consisting of quarks and gluons in collisions of relativistic heavy-ions. Experimental results have shown that in relativistic heavy-ion collisions a dense hadronic fireball can be formed, well localized in space, with an energy density exceeding 1 GeV/fm^3 [12]. Due to the high internal pressure, this fireball explodes rapidly: the lifetime is characterized by the size of the system $\tau \simeq$ 2R/c. In relativistic heavy-ion reactions, the collision energy is shared among numerous newly produced hadronic particles. In the final state much more low-energy particles than high-energy particles are produced, the latter mainly stemming from hard, elementary interactions. The conversion of kinetic collision energy into high particle multiplicity can be examined using statistical mechanics. This description does not require a complete knowledge of the microscopic production and dynamics of particles. It is also expected that very high baryon densities which are comparable to those in the core of neutron stars can be reached in heavy-ion collisions. Complementary to the activities at the Relativistic Heavy Ion Collider (RHIC) at BNL and the Large Hadron Collider (LHC) at CERN, which concentrate on high temperatures and very low net baryon densities, the approach of the Compressed Baryonic Matter (CBM) experiment is the exploration of the phase diagram in the region of highest baryon densities. The CBM research program aims at the exploration of the structure of high-density matter, particularly the question of deconfinement and chiral phase transitions.

Fig.1.2 which depicts results of transport code calculations for central Au + Au collisions. According to these calculations, densities of up to 7 times saturation density

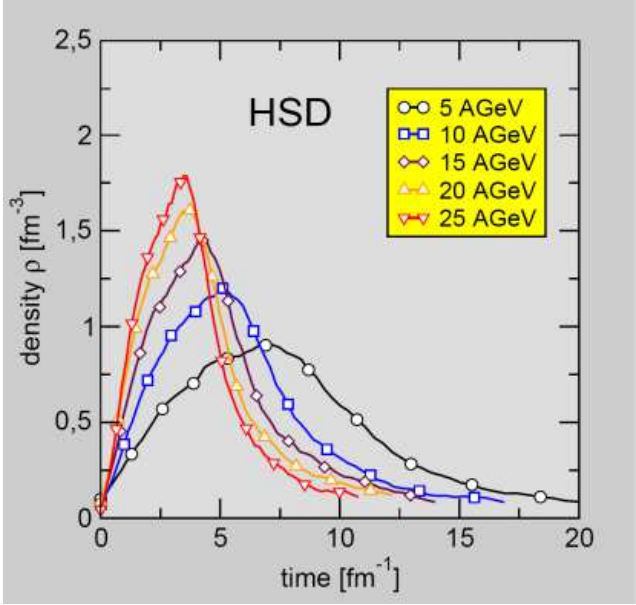

Figure 1.2. Baryon density as a function of elapsed time for central Au + Au collisions at different energies as calculated with the HSD transport code [13].

can be already produced at beam energies of 10 A GeV. Under these conditions the nucleons overlap, and theory predicts a transition to a mixed phase of baryons and quarks. Details about the CBM experiment can be found in Chapter 2.

The relativistic heavy ion collisions can be divided in to two separate regimes: the stopping regime where baryons stemming from the projectile and the target are fully or partly stopped by each other, forming a fairly baryon rich matter in the middle of the reaction zone, and the transparent region where initial target and projectile baryons are so far apart in the phase space that the heavy ion collision cannot slow them down completely. The boundary between these two regions is not very sharp and experimentally not known yet.

1.2.1 Stopping region

As indicated by the first results from the SPS at CERN and AGS at BNL, up to 60 A-GeV there is almost complete stopping in reactions with S and Si projectiles. Some theoretical estimates predict that with lead beams even 200 or 800 A GeV collisions will result in stopping of the baryons in the middle of the reaction zone and of the phase space [14]. Thus, these reactions provide a tool to study very highly excited baryon rich matter, or eventually baryon rich quark gluon plasma. This area has also astrophysical relevance associated with possible hybrid stars, i.e. neutron stars with dense quark matter core. The Compressed Baryonic Matter experiment at the future FAIR, Germany, a fixed target experiment, will be devoted for the exploration of matter at high baryon density.

1.2.2 Transparent region

If we increase the energy further the theoretical expectation is that the initial baryon charge from the projectile and target will not be slowed down completely. The quanta carrying this baryon charge will essentially keep their initial velocities and the middle zone in the reaction will be baryon free. Of course energy will be deposited in this region also. The large energy density matter in the central region may form a baryon free quark gluon plasma, which is of large theoretical interest. The theoretical model calculations are more straightforward for this form of matter than for baryon rich quark gluon plasma, and furthermore,this form of high energy density and low baryon density matter is the one which was present in the early universe before hadrons were formed. The heavy ion accelerators which would be able to reach this energy region are: the Large Hadron Collider (LHC) at CERN and the Relativistic Heavy Ion Collider (RHIC) at BNL. The TEVATRON at Fermilab can be mentioned as a proton antiproton collider relevant to this research.

1.2.3 Heavy ion Experiments

In low energy nuclear physics, the most frequent event is an elastic collision, where the target and projectile maintain their integrity and even their internal quantum state. In low energy inelastic processes, one or both of the outgoing particles may be in excited states, and even some extra third (or fourth) particle(s) are created. But in any case the final multiplicity is rather small. Consequently it is satisfactory at these energies to measure one or at most two outgoing particles. Although in principle there exist a reaction plane in these reactions it cannot be reliably identified in low multiplicity events particularly if some of the particles are not measured (like neutrals). Thus it is customary to measure azimuth averaged cross sections in low energy nuclear and particle collision experiments. In relativistic heavy ion collisions the multiplicities are large. Already at 100 A MeV beam energy we can have about 10-100 secondaries, while at 100 A GeV the number of produced particles may exceed 1000, i.e., it can be much more than the number of initial nucleons. This large multiplicity leads to special experimental requirements not known before in nuclear physics. These multiplicities exceed even the multiplicities of highest energy particle physics experiments. To a general characterization of the event, first of all event by event detection is desirable, and it is also advantageous if we can measure all emitted particles in an event simultaneously. Obviously these requirements led to the introduction of highly segmented detector arrays, like the MSU 4π detector [15], the BEVALAC Plastic Ball [16], or the large detector arrays at the CERN-SPS and BNL- AGS heavy ion experiments. Another alternative is a large volume track detector like the streamer chamber, time projection chamber (TPC) or stacks of nuclear emulsion. Nowadays heavy ion detectors are using cutting edge technology. With these advanced detectors, the increasing multiplicity does not seem to be an obstacle at the first sight, but the track recognition problem becomes increasingly difficult at very large multiplicities. Recently new techniques are experimented with, like neural networks, to solve the track recognition problem.

1.3 Chiral Symmetry Restoration

Chiral symmetry is a symmetry of QCD in the limit of vanishing quark masses. We know,however, that the current quark masses are finite. But compared with hadronic scales, the masses of the two lightest quarks, up and down, are very small, so that chiral symmetry may be considered an approximate symmetry of the strong interactions [17]. Long before QCD was known to be the theory of strong interactions, phenomenological indications for the existence of chiral symmetry came from the study of the nuclear beta decay. There one finds, that the weak coupling constants for the vector and axial-vector hadronic-currents, C_V and C_A , did not (in case of C_V) or only slightly (25% in case of C_A) differ from those for the leptonic counterparts. Consequently strong interaction 'radiative' corrections to the weak vector and axial vector 'charge' are absent. The same is true for the more familiar case of the electric charge, and there we know that it is its conservation, which protects it from radiative corrections. Analogously, we expect the weak vector and axial vector charge, or more generally, currents, to be conserved due to some symmetry of the strong interaction. In case of the vector current, the underlying symmetry is the well known isospin symmetry of the strong interactions and thus the hadronic vector current is identified with the isospin current. The identification of the axial current, on the other hand is not so straightforward. This is due to another, very important and interesting feature of the strong interaction, namely that the symmetry associated with the conserved axial vector current is 'spontaneously broken'. By that, one means that while the Hamiltonian possesses the symmetry, its ground state does not. An important consequence of the spontaneous breakdown of a symmetry is the existence of a massless mode, the so called Goldstone-boson. In our case, the Goldstone boson is the pion. If chiral symmetry were a perfect symmetry of QCD, the pion should be massless. Since chiral symmetry is only approximate, we expect the pion to have a finite but small (compared to all other hadrons) mass. This is indeed the case! The fact that the pion is a Goldstone boson is of great practical importance. Low

energy/temperature hadronic processes are dominated by pions and thus all observables can be expressed as an expansion in pion masses and momenta. This is the basic idea of chiral perturbation theory, which is very successful in describing threshold pion physics. At high temperatures and/or densities one expects to 'restore' chiral symmetry. By that one means, that, unlike the ground state, the state at high temperature/density possess the same symmetry as the Hamiltonian (the symmetry of the Hamiltonian of course will not be changed). As a consequence of this so called 'chiral restoration' we expect the absence of any Goldstone modes and thus the pions, if still present, should become as massive as all other hadrons. To create a system of restored chiral symmetry in the laboratory is one of the major goals of the ultra-relativistic heavy ion experiments including the CBM experiment.

1.4 Experimental Signatures of Phase Transition

Many signals have been proposed and are still under discussion, although the hope for finding a striking and convincing has not yet become true. The discovery of the critical endpoint or signals of a first order phase transition would be such a direct indication for the existence of a new phase. Theoretical investigations suggest that particle density fluctuations occur in the vicinity of the critical endpoint, which might be observed experimentally as non statistical event-by-event fluctuations of observables [19]. This phenomenon was also seen in lattice QCD calculations [10]. The fluctuation signal should show up around a certain beam energy. In this section we will briefly review the existing data which are relevant for the study of the high baryon density region of the QCD phase diagram which is the program for the future CBM experiment at FAIR. We outline main signatures of QGP and discuss what features of the phase transition, they mainly point out.

1.4.1 Di-leptons

A precise measurement of the dilepton invariant mass spectrum up to about 1 GeV provides information on the in-medium properties of the vector meson spectral function as a signal of the chiral symmetry restoration in the hot and dense matter. At higher invariant masses the spectrum contains a substantial contribution from thermal dileptons from the early partonic phase. The different origin of the dileptons is also reflected in the inverse slope of their transverse momentum spectra. The experimental determination of dileptons emitted from the high-density phase of the collision requires the measurement (and subtraction) of contributions from very early nucleon-nucleon collision, from the dilute corona, and from freeze-out.

The HADES collaboration has performed precision measurements of the invariant-mass spectra of electron-positron pairs in nuclear collisions at beam energies of 1A - 2A GeV. The excess of di-lepton yield in C + C collisions in the invariant- mass range 0.2 - 0.7 GeV/c^2 as reported by the DLS experiment was confirmed [20]. However, it was shown that the spectrum measured in C + C corresponds to a superposition of lepton pairs from p + p and p + n collisions [21]. In contrast, heavier systems like Ar + KCl show a di-lepton excess yield relative to the nucleon-nucleon reference data [22]. At SIS-100, the HADES di-electron programme will be continued towards larger collisions systems and to higher energies, where the net-baryon densities are substantially higher and the in-medium effects can thus be expected to be more pronounced. In particular, the precise and systematic measurement of the in-medium mass distribution of the short-lived ρ meson is expected to provide information on the conditions and degrees of freedom inside the hot fireball produced in heavy-ion collisions. While HADES at SIS-100, being limited by detector granularity, will investigate collision systems up to Ni+Ni, the measurement of di-electron spectra in heavier systems is a central part of the CBM physics programme at SIS-100.

1.4.2 Charm production

Particles containing heavy quarks like charm are produced in the early stage of the collision. At FAIR, open and hidden charm production will be studied at beam energies close to the kinematical threshold, and the production mechanisms of D and J/ψ mesons will be sensitive to the conditions inside the early fireball. The anomalous suppression of charmonium due to screening effects in the Quark Gluon Plasma (QGP) was predicted to be an experimental signal of the QGP [23]. J/ψ mesons were measured via their decay into muon pairs in heavy-ion collisions at top CERN-SPS energies by the NA50 experiment. It was found that the J/ψ yield decreases relative to the Drell-Yan yield with increasing collision centrality [24], the so called J/ψ suppression, which was considered as a signal for the QGP discovery. The interpretation of the NA50 results is subject of an ongoing debate as the data can be explained also within hadronic scenarios.Data on open charm will be useful for pinning down the source of the J/ψ suppression, and provide an independent probe of the QGP. The next generation experiments aim at the measurement of open charm which will provide further constraints. Moreover, the effective masses of D-mesons - a bound state of heavy charm quark and a light quark - are expected to be modified in dense matter similarly to those of kaons. Such a change would be reflected in the relative abundance of charmonium ($c\bar{c}$) and D-mesons [25]. D-mesons can be identified via their decay into kaons and pions (D0 $\rightarrow \pi$K, D$\pm \rightarrow \pi\pi$K). The experimental challenge is to measure the displaced vertex of kaon-pion pairs with an accuracy of better than 100 μm in order to suppress the large combinatorial background caused by promptly emitted kaons and pions

1.4.3 Strangeness in dense matter

One of the early predictions for a QGP signal was an increased production of strangeness in the deconfined phase resulting in an enhanced yield of strange particles after hadronization [26]. This effect was expected to be even more pronounced for multi-

strange hyperons. Indeed, the NA57 experiment observed that the multiplicity of Ξ and Ω hyperons per participant is higher in nucleus-nucleus collisions than in proton-proton (or proton-Beryllium) collisions [27]. Moreover, the enhancement increases according to the s- hierarchy. Again, the interpretation of these results is still under discussion. An intriguing finding is that the slope of the kinetic energy distribution of Ω is steeper than expected. This indicates that the Ω hyperon - which consists only of strange quarks - might freeze out very early. Recently, data on the excitation function of strangeness production measured by NA49 have evived the discussion on the role of strangeness as a signature for a deconfinement phase transition [28]. Of particular interest is the peak (so called horn) in the dependence of the K^+ / π^+ ratio on the projectile energy, which appears at 20 - 30 A GeV and is not reproduced within statistical and transport models. This peak coincides with the increase of the event-by-event kaon to pion ratio fluctuations at lower SPS energies. Whether these observations are connected to the critical point of the QCD phase diagram requires further studies.

1.4.4 Hadron yields and phase-space distributions

The excitation function (from 2 - 45 A GeV) of hadron yields and phase space distributions (including multi- strange hyperons) will provide information about the fireball dynamics and the nuclear matter equation-of-state over a wide range of baryon densities. A non-monotonic behavior of the inverse slope as function of beam energy would signal a change in the nuclear matter properties at a certain baryon density. The inverse-slope distribution as a function of particle mass is related to the particle freeze-out time, and, hence, may help to disentangle the early from the late collision stages.

1.4.5 Hypernuclei

Nuclei containing at least one hyperon in addition to nucleons, offer the fascinating perspective to explore the third, strange dimension of the chart of nuclei. Their investi-

gation provides information on the hyperon-nucleon and even on the hyperon-hyperon interaction, which play an important role in neutron star models. In heavy-ion collisions at FAIR (even double-lambda) hypernuclei will be produced via coalescence of Λ with nucleons or light nuclei in the final state of the reaction.

1.4.6 Collective Flow

The collective motion of the final-state hadrons resulting from heavy-ion reactions contains important information on the collision dynamics. The isotropic, radial flow allows to characterise the collision system at kinetic freeze-out, i.e. when elastic collisions of the produced particles cease. Anisotropic flow results from the conversion of anisotropies in the density distribution into pressure gradients, and thus gives access to the equation of state of dense nuclear matter. Moreover, the flow of strange particles and anti-baryons is determined by their in-medium potential and hence allows to address the restoration of chiral symmetry in the dense medium. Flow measurements at SIS-18 and AGS provided first insight into these topics, but left a number of features to be addressed by a second-generation experiment. At AGS, the experiment E895 measured the proton elliptic flow and reported a transition from out-of-plane to in-plane emission at about 6 A GeV [29]. The data indicate an evolution from a stiff equation-of-state below 2 A GeV to a softer one at higher beam energies. Such a softening of the EOS was suggested to be indicative for a phase transition to a deconfined state [30]. Flow measurements of the FOPI collaboration at SIS-18, however, seem to exclude a stiff equation of state [31, 32], a conclusion which is in line with earlier results of KaoS and FOPI on kaon production [33, 34]. Data on strange particle flow at SIS-100 energies are scarce; the KaoS collaboration reported different emission patterns for K^- and K^+ in Au + Au collisions at 1.5 A GeV, which could be reproduced by a microscopic transport model assuming an attractive K^- N in-medium potential [35]. The sideward flow of K^0 in Au+Au collisions at 6 A GeV, measured by the E895 collaboration [36],

shows a pattern which is quite distinct from that observed at lower energies and is not yet reproduced by model calculations. In order to conclusively address the degree of thermalisation, the equation of state, and the in-medium properties of strange particles, multi differential flow measurements for a large variety of hadron species, in particular strange hadrons and anti-baryons, are mandatory for a variety of collisions systems and beam energies in the SIS-100 energy range.

1.4.7 Fluctuations and Correlations

Lattice calculations indicate large variations of the baryon, charge and strangeness susceptibilities in the vicinity of the QCD critical endpoint. These phenomena can be related to event-by-event fluctuations of conserved quantities such as net baryon number, net charge, and net strangeness. Fluctuations of the kaon, pion and proton multiplicities, in particular of their higher moments, measured as a function of beam energy, are expected to be sensitive indicators for the location of the critical point. A promising experimental task is the search for fluctuations and correlations caused by a first-order phase transition, focussing on the fact that bulk matter is unstable inside the associated spinodal region. Event-by-event fluctuations are an important observable to be studied at the future CBM experiment at FAIR. CBM will investigate the intermediate region of the QCD phase diagram in great detail searching for the first order phase transition line and the expected critical endpoint. It is therefore important to investigate the sensitivity of the CBM detector to particle ratio fluctuations in Au + Au collisions at 10 - 45 A GeV beam energy.

1.5 Organization of Thesis

Chapter 2 starts with the general introduction to the CBM experiment at FAIR. The measurements of bulk hadrons, multistrange hyperons, hypernuclei, charmonium and

low mass vector mesons in nuclear collisions requires a large acceptance, high rate detector system. The proposed detectors of this experiment are Silicon tracking System (STS), Micro Vertex Detector (MVD), Time of Flight (TOF) detector, Ring Imaging Cherenkov (RICH) detector, Transition Radiation Detector (TRD) , Muon Chamber (MUCH), Electromagnetic Calorimeter (ECAL) and Projectile Spectator Detector (PSD).

Chapter 3 starts with the introduction to the Muon Chamber (MUCH). One of the important aspects of the CBM experiment is to look for rare probes like charmonia (J/ψ,ψ' etc.) having extremely low production cross section in the FAIR energy regime. Charmonia as well as low mass vector mesons (ρ, ω, ϕ) can be measured via their decay in di-muons. Thus a Muon Chamber is needed to detect these dimuons. The MUCH system consists of six alternating layers of absorbers and triplets of tracking chambers. The first few tracking chambers will be of Gas Electron Multiplier (GEM) detectors.

Chapter 4 starts with the introduction to Gas Electron Multiplier (GEM) detector. A large acceptance, high-granularity and high rate muon detection system (MUCH) is proposed to be built in the CBM experiment for carrying out the measurements of charmonium(J/Ψ) and low mass vector mesons by their muonic decay channels in high energy heavy ion collisions. Current design of the muon system consists of six sets of alternating layers of absorbers and detector triplets. For the first few stations, where the particle rates reach 1 MHz/cm^2, GEM based detectors are being developed as tracking chambers. The advantage of using the GEM are: The detector should be able to cope up with a high collision rate of $\sim$ 10 MHz. This high luminosity facilitates the measurement of rare probes mentioned above. Detector granularity should be high to cater to a hit of about 1 hit/ cm^2. The detector should be resistant to high dose of neutrons, photons and heavy ions. Large acceptance detector should have modular arrangement. Collecting data in a self triggered mode, which is the data taking mode for all CBM

detectors. The testing of GEM's at CERN-SPS H4 beam line area with beams of muon will be discussed. The GEM detectors performance in terms of efficiency, number of cells fired and gain will also be discussed.

Chapter 5 deals with the study of particle production mechanism at CBM energies using different models such as statistical thermal model and transport models.The main motivation of this study is to show what one should expect in context to particle multiplicities and particle ratios at CBM energy range i.e. 10 A GeV to 40 A GeV lab energies (4.43 GeV to 8.71 GeV center-of-mass energies) , in view of equilibrated statistical as well as transport models. We have also compared the model results with available experimental data of Alternating Gradient Synchrotron (AGS) and Super Proton Synchrotron (SPS) energies.

In **Chapter 6**, we present a summary and conclusion drawn from this work and provide some insights in this area for future research work.

1.6 Summary and Conclusions

I wish to summarize the introduction chapter as put foreword by Frank Wilczek in the CBM physics book [37] *"Why study compressed baryonic matter, or more generally strongly interacting matter at high densities and temperatures? Most obviously, because its an important piece of Nature. The whole universe, in the early moments of the big bang, was filled with the stuff. Today, highly compressed baryonic matter occurs in neutron stars and during crucial moments in the development of supernovae. Also, working to understand compressed baryonic matter gives us new perspectives on ordinary baryonic matter, i.e. the matter in atomic nuclei. But perhaps the best an-*

swer is a variation on the one George Mallory gave, when asked why he sought to scale Mount Everest: Because, as a prominent feature in the landscape of physics, its there. Compressed baryonic matter is a material we can produce in novel, challenging experiments that probe new extremes of temperature and density. On the theoretical side, it is a mathematically well-defined domain with a wealth of novel, challenging problems, as well as wide-ranging connections."

Chapter 2

The CBM experiment

2.1 Facility for Antiproton and Ion Research

The future FAIR accelerator facility comprises a multifaceted science program, with beams of stable and unstable nuclei as well as antiprotons in a wide range of intensities and energies and excellent beam qualities [38]. A sketch of the future FAIR together with the existing GSI facilities is presented in Fig.2.1.

FAIR comprises two synchrotrons (SIS 100/300) with a circumference of about 1,000 m and with magnetic rigidities of 100 Tm and 300 Tm, respectively. In conjunction with an upgrade for high intensities, the existing GSI accelerators UNILAC and SIS 18 serve as injectors for the new synchrotrons. Adjacent to the double-synchrotron is a complex system of storage-cooler rings and experimental stations, including a superconducting nuclear fragment separator (Super-FRS) and an antiproton production target. Beyond, there is the storage ring for antiprotons (high-energy storage ring (HESR), the collector ring (CR), and the new experimental storage ring (NESR). On the one hand, FAIR provides beams of rare isotopes and antiprotons with an unparalleled intensity and quality and on the other hand, the facility is designed to provide particle energies twenty times higher than those achieved at GSI so far. Up to now, this energy regime has only been explored at the AGS up to about 14 A GeV. Due to the intrinsic cycle times of the accelerator and storage-cooler rings, up to four research programs can be run in parallel. The experimental facilities include the CBM experiment investigating

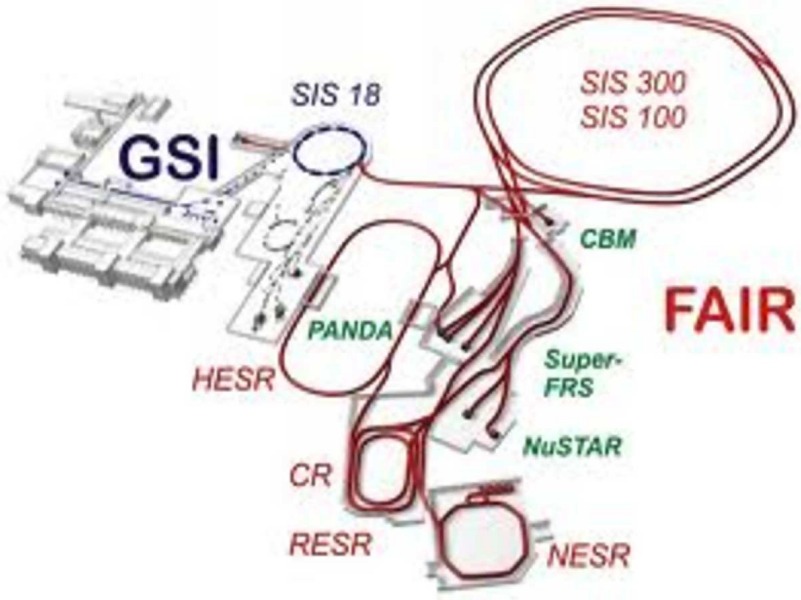

Figure 2.1. Schematic of the future FAIR facility.

nucleus-nucleus collisions at highest baryon densities, the PANDA detector for hadron physics experiments using cooled high-energy antiproton beams, the NUSTAR detectors used for experiments on the structure of unstable nuclei and on nuclear astrophysics as well as experimental set ups for plasma physics and atomic physics. In order to meet the demands of all experiments, the FAIR accelerator facility has to fulfill a set of very different requirements. FAIR is expected to provide beams of all ion species, from hydrogen to uranium, as well as antiprotons covering a large energy regime (from particles at rest up to several tens of A GeV energy in the laboratory frame). In order to achieve highest baryon densities and enable charm production in high-energy nucleus-nucleus collisions, the SIS 300-synchrotron is designed for beam energies of up to 35 A GeV for U^{92+}. A unique feature of the FAIR facility, which is the major advantage for heavy-ion physics, compared to RHIC and CERN at the same energy, is the possibility of providing extremely high beam intensities. For primary beams, the intensity increase aimed for is a factor of several hundred for the heaviest ion species compared to present installations at GSI.

2.1.1 Schwerionen Synchrotron (SIS) 300

The beams for CBM will finally be provided by the SIS 300 synchrotron. The two synchrotrons SIS 100 and SIS 300 will be built on top of each other in an underground tunnel. They are equipped with rapidly cycling superconducting magnets. Both heavy-ion and proton beams can be compressed to very short bunch lengths required for the production and subsequent storage and efficient cooling of exotic nuclei and antiprotons. These short ion bunches are also needed for plasma-physics experiments.The available kinetic beam energy per nucleon depends on the bending power B . r provided by the dipole magnets: E/A = $\sqrt{(0.3.B.r.Z/A)^2 + m^2}$ - m, with B . r = 300 Tm for the maximum beam rigidity of SIS 300. A is the atomic mass, Z is the atomic number, and m is the average mass of a nucleon. According to the above equation, the SIS 300 provides high-energy ion beams of maximum energies around 45 A GeV for Ne^{10+} beams and close to 35 A GeV for fully stripped U^{92+} beams. The highest available proton energy for a beam rigidity of 300 Tm is 89 GeV. The maximum intensities in this mode are 10^{13} ions/s for protons and close to 10^9 ions/s for Au ions. These high-energy beams are extracted over periods of 10 - 100 s in quasi-continuous mode. According to the current FAIR schedule, beams in the SIS 100 might become available as of 2014, and the SIS 300 synchrotron will be completed at the earliest in 2016.

2.2 The CBM experiment

The CBM experiment will conduct a comprehensive research programme on nucleus-nucleus collisions at FAIR. The aim of the CBM project is to investigate the largely unexplored QCD phase diagram at highest net baryon densities and moderate temperatures, complementary to the heavy ion programmes at RHIC and at LHC that address the physics of the early universe at low densities and high temperatures. With projectile energies between 10 and 45 A GeV SIS-300 will provide intense beams in the range where

the highest net baryon densities are predicted to reach about 10 times that of ground state nuclear matter. This will enable the CBM programme to focus on signatures of the expected first order phase transition from partonic to hadronic matter, ending in a critical point, and on modifications of hadron properties, e.g. their masses, in the dense nuclear medium as a signal of chiral symmetry restoration [39–41]. The CBM experimental strategy is to perform systematically both integral and differential measurements of almost all the particles produced in nuclear collisions (i.e. yields, phase-space distributions, correlations and fluctuations) with unprecedented precision and statistics. These measurements will be performed in nucleus-nucleus, proton-nucleus, and - for baseline determination - proton-proton collisions at different beam energies. The identification of multi-strange hyperons, hypernuclei, particles with charm quarks and vector mesons decaying into lepton pairs requires efficient background suppression and very high interaction rates. In order to select events containing those rare observables, the tracks of each collision have to be reconstructed and filtered online with respect to physical signatures. This concept represents a paradigm shift for data taking in high-energy physics experiments: CBM will run without hierarchical trigger system. Self-triggered read-out electronics, a high-speed data processing and acquisition system, fast algorithms, and, last but not least, radiation hard detectors are indispensable prerequisites for a successful operation of the experiment.

2.2.1 The Experimental Challenge

The experimental challenge is to measure multi-differential observables and particles with very low production cross sections such as multi-strange (anti-) hyperons, particles with charm and lepton pairs with unprecedented precision. The situation is illustrated in Fig. 2.2 which depicts the product of multiplicity times branching ratio for various particle species produced in central Au+Au collisions at 25 A GeV. The data points are calculated using either the HSD transport code [12] or the thermal model based on

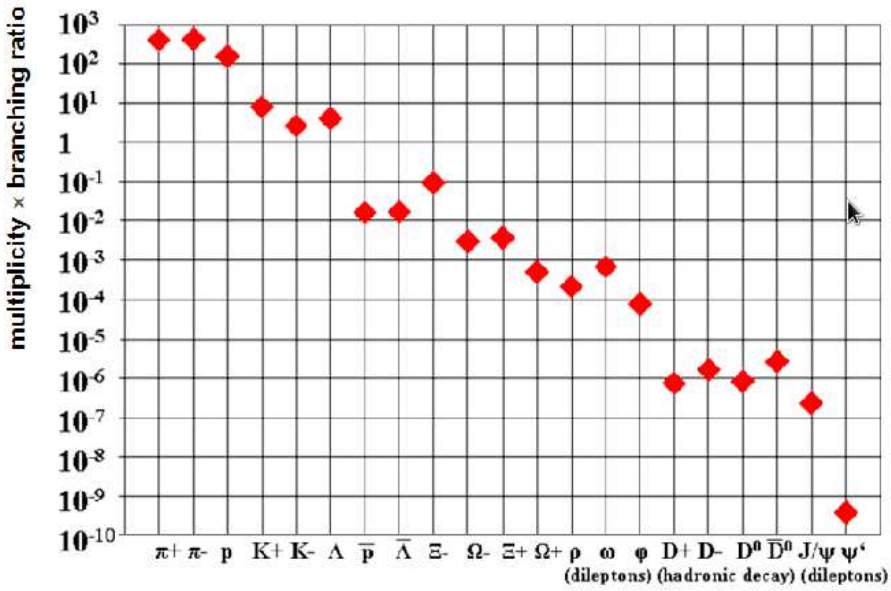

Figure 2.2. Particle multiplicities times branching ratio for central Au+Au collisions at 25 A GeV as calculated with the HSD transport code [12] and the statistical model [14]. For the vector mesons (ρ, ω,ϕ, J/ψ, ψ') the decay into lepton pairs was assumed, for D mesons the hadronic decay into kaons and pions.

the corresponding temperature and baryon-chemical potential [14]. Mesons containing charm quarks are about 9 orders of magnitude less abundant than pions (except for the ψ' meson which is even more suppressed). The dilepton decay of vector mesons is suppressed by the square of the electromagnetic coupling constant $(1/137)^2$, resulting in a dilepton yield which is 6 orders of magnitude below the pion yield, similar to the multiplicity of multi-strange anti-hyperons. In order to produce high statistics data even for the particles with the lowest production cross sections, the CBM experiment is designed to run at reaction rates of 100 kHz up to 1 MHz [18]. For charmonium measurements where a trigger on high-energy lepton pairs can be generated reaction rates up to 10 MHz are envisaged. The CBM experiment is planned to provide two different setups. The first setup is dedicated to measurements based on electron/positron pairs and to open charm physics. This setup is shown in figure 2.3. It contains a Silicon Tracking System (STS) formed by a micro vertex detector based on silicon pixel detectors and by a tracker based on silicon strip detectors. The STS is located in the field of a dipole magnet with a bending power of roughly 1 T m. Together with a time of flight (TOF) hadron identification system, which is formed by a diamond start detector and resistive plate chambers (TOF-Wall), the STS serves for open charm measurements. The very good electron identification abilities required for the reconstruction of hadrons decaying into electron/positron pairs is provided by a Ring Imaging CHerenkov detector (RICH) and additional Transition Radiation Detectors (TRD). The RICH is used to identify low and medium energy electrons and supports open charm measurements by identifying fast pions. The electron identification abilities of the RICH shrink with increasing electron energy. The system is thus complemented by TRDs, which provide an efficient identification of very fast electrons. The measurement chain for electron positron pairs is completed by an electro-magnetic calorimeter. Besides those detectors, Projectile Spectator Detector is also there at the end. This calorimeter is intended to characterize the event centrality by measuring the energy taken away by spectator fragments, which did not participate in the collision. The second setup aims for a reconstruction

Table 2.1. Yields of particles for central Au + Au at 25 A GeV.

Particle	J/ψ	ρ_0	ω	ϕ
Mass(MeV)	3095	770	782	1020
Multiplicity	1.95×10^{-5}	23	38	1.28
Branching ratio of dimuon channel	6	4.6×10^{-5}	9×10^{-5}	2.9×10^{-4}
Number per event	1×10^{-6}	1×10^{-3}	3.4×10^{-3}	3.7×10^{-4}

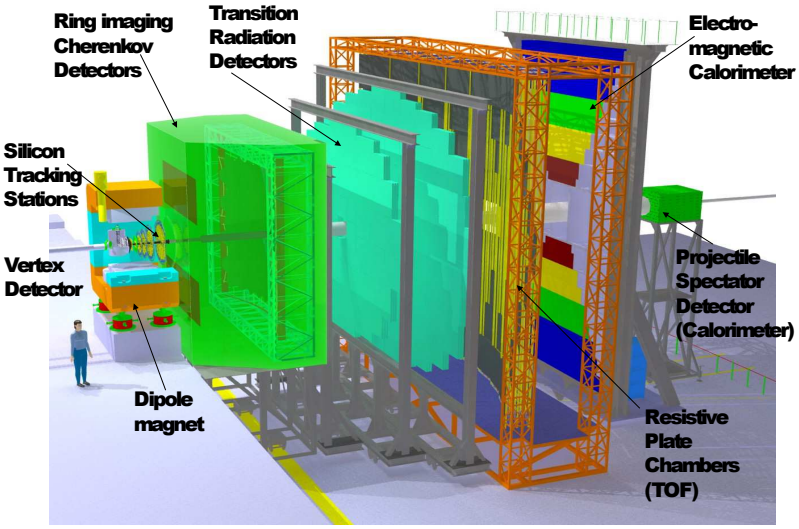

Figure 2.3. Schematic of future CBM experiment for electron identification.

of hadrons decaying into dimuon pairs, which is shown in figure 2.4. This setup is formed by the STS and a muon detector based on a sandwich of tracking detectors and metal layers, which are to stop electrons and hadrons. This detector replaces the RICH detector. The next few sections describes in detail the detectors which will be used in the CBM experiment

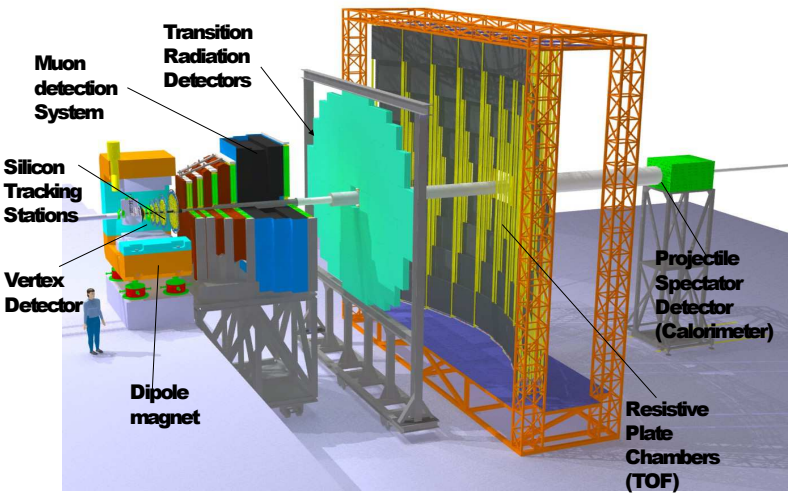

Figure 2.4. Schematic of future CBM experiment for muon identification.

2.3 Superconducting Dipole Magnet

The magnet hosts the Silicon Tracking System (STS), and provides a magnetic field integral of 1 Tm which is needed to obtain a momentum resolution of Δp/p=1 % for track reconstruction at FAIR beam energies. The magnet gap has a height of 140 cm and a width of 250 cm in order to accommodate the STS with a polar angle acceptance of $\pm 25^o$ and a horizontal acceptance of $\pm$ 30^o. The magnet is of the H-type with a warm iron yoke/pole and cylindrical superconducting coils in two separate cryostats like the SAMURAI magnet at RIKEN. The potted coil has 1749 turns. The wire similar to the wire used in CMS experiment has Nb-Ti filaments embedded in a copper matrix, and is soldered in a copper stabilizer with a total Cu/SC ratio of about 13 in the conductor. The operating current and the maximal magnetic field in the coils are 686 A and 3.25 T, respectively. The coil case made of stainless steel contains 40 l of liquid helium. The vertical force in the coils is about 250 tons. The cold mass is suspended from the room temperature vacuum vessel by six suspension links. Six cylindrical support struts

compensate the vertical forces. The energy stored in the magnet is about 5 MJ. The magnet will be self-protecting. However, in order to limit the temperature rise to 100 K in case of a quench, the energy will be dumped in an external resistor.

2.4 Micro Vertex Detector (MVD)

The determination of the decay vertices of open charm particles (c = 123 μm/c for D0 mesons and c= 314 μm/c for D$\pm$ mesons) requires detectors with excellent position resolution and a very low material budget in order to reduce multiple scattering [42]. These requirements are met by Monolithic Active Pixel Sensors (MAPS). The pixel size will be between 18 $\times$ 18 μm^2 and 20 $\times$ 40 μm^2. A position resolution of σ = 3.5 - 6.0 μm can be achieved depending on the pixel size. The goal of the detector development is to construct vacuum compatible MAPS detector stations with a total thickness of about 300 500 μm silicon equivalent for sensors and support structures, depending on the size of the stations. The MVD consists of 3 MAPS layers located 5, 10 and 15 cm downstream the target in the vacuum. A 4^{th} MAPS station might be located at 20 cm behind the target. This detector arrangement permits to determine the secondary decay vertex of a D-meson with a resolution of about (50-100) μm along the beam axis.

2.5 Silicon Tracking Stations (STS)

The detector system's task is to measure the trajectories and momenta of charged particles originating from the interactions of heavy-ion beams with nuclear targets [43]. Up to 1000 charged particles are produced per interaction, at rates up to 10 MHz to enable CBM physics with rare observables. The track reconstruction has to be achieved with 95 % efficiency and a momentum resolution Δp/p = 1 %. These requirements can be fulfilled with a tracking system of 8 low-mass layers of silicon microstrip sensors located at distances between 30 cm and 100 cm downstream of the target inside the

magnetic dipole field. The sensors are mounted onto light weight mechanical support ladders and read out through multi-line micro-cables with fast self-triggering electronics at the periphery of the stations where cooling lines and other infrastructure can be placed. The micro-cables will be built from sandwiched polyimide-Aluminum layers of several thickness. The microstrip sensors will be double-sided with a stereo angle of 7.5^o , a strip pitch of 58 μm, strip lengths between 20 and 60 mm, and a thickness of 300 μm of silicon. According to the CBM running scenario the maximum non-ionizing dose for the sensors closest to the beam 1×10^{14} n_{eq} cm^{-2}. The STS is operated in a thermal enclosure that keeps the sensors at a temperature of about - 5^o C. The heat dissipated in the read-out electronics is removed by a CO_2 cooling system. The mechanical structure of the detector system including the service and signal connections is designed such that single detector ladders can be exchanged without disconnecting and removing more than one detector station [44].

2.6 Muon Detection System (MUCH)

As an alternative approach to the dielectron measurement the possibility of detecting vector mesons, like ρ, ω, ϕ and J/ψ, via their decay into dimuons is currently under investigation. For this measurement, hadrons would be suppressed with several absorber layers located behind the STS. A possible setup for the Muon Chamber System (MuCh) is presented in Fig. 3.1.(chapter 3). Like in the electron setup (as seen in the Fig. 2.2), the momentum of these tracks is determined with the STS. Subsequently, all charged particles are tracked through the absorber in order to match the muons, which pass the absorber, to the STS tracks. This can be achieved by highly granulated and fast detectors which are located in each gap between the absorber layers. The current design of the muon detection system foresees 18 detector stations and 6 segmented iron absorbers. In this case, the total material budget would correspond to 13.5 times the nuclear interaction length. Promising candidates for the fast and highly granulated

detectors, located in the five gaps between the absorber layers, are gaseous detectors based on GEM technology, straw tubes, and one of the TRD stations. The total area of the muon chambers would cover an area of about 70 m^2 . The solution offering the most comprehensive research program would be to build both setups which can be used alternately. In that case, the RICH has to be temporary removed and the last 3 detectors of the MuCh can correspond to tracking detectors which will anyway be in place in order to cover the gap between STS and TOF. The TRD, for example, could be used for this purpose, too. Of course, the ECAL cannot be used in conjunction with the muon detection system.

2.7 Ring Imaging Cherenkov Detectors (RICH)

The task of the RICH detector is to identify electrons from lowest momenta up to 8 to 10 GeV/c. This identification has to be achieved with a pion suppression of at least 100 in order to ensure a high quality of the measurement of di-electrons as there are low-mass di-electrons, charmonium but also the reconstruction of photons using γ-conversion pairs [45]. These requirements can be fulfilled with a gaseous RICH detector using CO_2 as radiator gas. The Cherenkov light will be focussed as rings by spherical glass mirrors with a reflective Al and protective MgF_2 coating onto a photon detector array. As photon detector multi-anode photomultiplier tubes are foreseen. They provide sufficient granularity, very good noise performance, a stable operation and fast response to allow running at 10 MHz interaction rate which is the maximum CBM is aiming for. The RICH detector will be placed next to the dipole magnet housing the Silicon Tracking System of CBM and in front of the Transition Radiation Detectors system which provides additional electron identification and tracking towards the time-of-flight detector. Its mechanical structure including the service and signal connections is designed such that the whole detector can be moved out of the CBM setup in order to allow a muon-detector system to move in for a complementary measurement of di-

leptons in the di-muon channel.

2.8 Transition Radiation Detectors (TRD)

The TRD [46] contributes to the electron identification and tracking of charged particles. Transition radiation (TR) is produced when a relativistic particle traverses an inhomogeneous medium, in particular the boundary between materials with different dielectric constants . For the expected particle momenta, TR is produced only by electrons and positrons ($\gamma > 1,000$), and this offers the possibility of separating them e.g. from pions. Currently, the TRD is envisaged to be a system composed of three stations with three to four layers each. These stations will be located at distances of 5 m, 7.25 m, and 9.5 m from the target. They cover a total active area of about 600 m^2 . Each layer consists of a radiator, in which the TR is produced by electrons, and of a gaseous detector, in which the deposited energy of charged particles and the TR can be measured. The gas mixture of the readout detector is based on Xe in order to maximize the absorption of TR. A very fast readout detector is required to cope with the high interaction rates of up to 10^9 Hz. Also the large multiplicities pose a challenge. For a fixed-target experiment such as CBM, in particular in the inner part of the detector, covering forward emission angles, high counting rates are expected. The central part of the TRD will be exposed to counting rates of up to 100 kHz/cm^2 . Thus, in order to minimize possible space charge effects, the gas volume must be sufficiently thin. At the same time, the aim is to achieve a high pion suppression factor of the order of 100 at an electron efficiency of 90% for the entire TRD. In addition, the TRD will be used for tracking of all charged particles with a position resolution of 300 - 500 μm in both directions, x and y, perpendicular to the beam direction. By way of example, this can also be realized with a position resolution of 300 - 500 μm in one direction and 3 - 30 mm in the other direction when rotating every second layer by 90^o. Up to now, two design options have been under consideration for such a detector: either a detector built from straw

tubes or a multiwire proportional chamber (MWPC) with pad readout. Such a design based on straw tubes has already been developed for the Transition Radiation Tracker (TRT) in the ATLAS experiment at LHC. It provides very good spatial resolution of about 200 μm even at rates of 4.5 MHz/cm^2. The other layout based on MWPC's with pad readout is comparable to the TRD based on drift chambers developed for the ALICE experiment at LHC [47]. This design has the advantage of providing an unrivaled electron/pion separation. It also provides sufficient tracking capability. Due to the much higher rates in CBM, this layout has to be modified in order to reduce the drift distance, i.e. going towards thinner gas volumes. Both TRD versions have been investigated as alternative designs. At present, the straw tubes are not considered as an option for the TRD anymore. Nevertheless, they are still possible as pure tracking chambers for the last three stations of the muon detection. The straw tube option looks quite promising for this application because of the good coordinate resolution of such detectors (200 μm in the drift direction) and the fact that this detector technology is rather simple and has shown to be reliable.

2.9 Time of Flight Detector (TOF)

A time-of-flight (TOF) measurement can be used to identify charged particles: the determination of the particle mass is based on the measurement of the time of flight, the particle momentum and the particle track length. The TOF wall consists of approximately 60,000 independent cells providing a resolution of $\sigma_{TOF} \leq 80$ ps. The TOF stop detector of CBM has an active area of about 150 m^2 located at a distance of 10 m from the target [48]. A diamond pixel (or micro-strip) detector provides the start signal for the TOF measurement. It directly counts the beam particles at intensities of up to 10^9 ions/s. The requirements for the TOF detector can be satisfied by a tRPC (timing Resistive Plate Chamber) with 25 - 30^o coverage in θ ($\sim$ 150 m^2). In order to cope with the high beam luminosity, the tRPC must handle rates of up to 20 kHz/cm^2

, while the Front End Electronics (FEE) must process the GHz signals from the tRPC at an interaction rate of up to 10 MHz. The current development of tRPCs shows very good performance in terms of high rate capability, low resistivity material, long term stability, and the possibility to build large arrays with sufficient timing performance. First prototypes with glass electrodes have already been built and tested. With an efficiency of 95% they showed a time resolution of 120 ps at rates of 18 kHz/cm^2. With an overall efficiency of 80% to 90%, a separation of kaons and pions can be achieved up to laboratory momenta of about 3.5 GeV/c, while protons can be identified up to 7 GeV/c.

2.10 Electromagnetic Calorimeter (ECAL)

In order to reconstruct photons, a shashlik type calorimeter shall be installed which consists of modules with granularities of 3×3 cm^2 , 6×6 cm^2 and 12×12 cm^2 [49]. Each module will be composed of 140 layers of 1 mm lead and 1 mm scintillator. Such techniques are commonly used, e.g. in the HERA-B experiment at DESY, in the PHENIX experiment at RHIC, and in LHCb at LHC. The electromagnetic calorimeter is designed to give the most precise and important measurement of particles energies. It can measure energies between a few tens of MeV up to 100 GeV. It measures the energies and positions of electrons, positrons and photons, and helps to discriminate between electrons and hadrons. The electromagnetic calorimeter will be used to measure real photons, neutral mesons decaying into photons, electrons and muons. Particular emphasis is put on a good energy resolution and spatial resolution for reconstruction of short-lived heavy particles (like J/ψ, D) decay products.

2.11 Projectile Spectator Detectors (PSD)

The Projectile Spectator Detector (PSD) is a compensating, modular lead-scintillator calorimeter, which is used to determine the collision centrality [49]. Good knowledge of the impact parameter is particularly important for analyzing event-by-event fluctuations, and in order to study collective effects like flow for which a well defined reaction plane is important. The PSD will measure nucleons from the projectile nucleus which did not interact. It is composed of 12×9 modules, each consisting of 60 lead/scintillator layers with a surface of 10×10 cm^2. The photons produced in the scintillator are measured via wavelength shifting by Multi-Avalanche Photo-Diodes (MAPD) of the size of 3×3 mm^2 and with a pixel density of 10^4 /mm^2. By using this layout, within a simulation of Au+Au collisions at 10 AGeV, an impact parameter resolution of Δb/b = 0.1 was determined for peripheral collisions and worsens to Δb/b = 0.5 for most central collisions. Note that the resolution is dominated by the physical fluctuations of the number spectators.

2.12 Data Acquisition System (DAQ)

High statistics measurements of particles with very small production cross sections require high reaction rates [50]. The CBM detectors, the online event selection systems, and the data acquisition will be designed for event rates of 10 MHz, corresponding to a beam intensity of 10^9 ions/s and a 1% interaction target, for example. Assuming an archiving rate of 1 GByte/s and an event volume of about 10 kByte for minimum bias Au+Au collisions, an event rate of 100 kHz can be accepted by the data acquisition. Therefore, measurements with event rates of 10 MHz require online event selection algorithms (and hardware) which reject the background events (which contain no signal) by a factor of 100 or more.The event selection system will be based on a fast on-line event reconstruction running on a high-performance computer farm equipped with many-core

CPUs and graphics cards (GSI GreenIT cube) [51]. Track reconstruction, which is the most time consuming combinatorial stage of the event reconstruction, will be based on parallel track finding and fitting algorithms, implementing the Cellular Automaton and Kalman Filter methods. For open charm production the trigger will be based on an online search for secondary vertices, which requires high speed tracking and event reconstruction in the STS and MVD. The highest suppression factor has to be achieved for J/ψ mesons where a high-energetic pair of electrons or muons is required in the TRD or in the MUCH. For low-mass electron pairs no online selection is possible due to the large number of rings/event in the RICH caused by the material budget of the STS. In the case of low-mass muon pairs some background rejection might be feasible.In order to still further suppress the background from 0 Dalitz decays and conversions topological cuts on track pairs reconstructed only in the STS are applied. In addition a thin, 0.1% interaction length target (or 1% interaction length segmented target) will be used for low-mass dielectrons. Under those conditions, 0.23 background tracks per central Au + Au collision at 25 A GeV contribute to the low- mass dielectron spectra. 60% of those electrons stem from π_0-Dalitz decays, 29% from γ-conversions, 4% from misidentified pions and 7% from secondary electrons. For background suppression in the high mass range, i.e. the J/ψ analysis, a cut on transverse momentum (1 GeV/c) is sufficient[51a].

2.13 Summary and Conclusions

The comparison of high precision data with theoretical models has demonstrated that dilepton pairs emitted in energetic heavy-ion collisions provide valuable information on the evolution and on the properties of the hot and dense fireball. It was shown, that the in-medium mass distribution of short-lived vector mesons decaying in lepton pairs is modified both due to their coupling to baryon resonances, and by their interaction with the chiral condensate. A careful analysis of the measured dilepton excess yield - i.e. the

dilepton mass distribution with the contribution from vector mesons subtracted - allows to extract the thermal radiation, and, hence, the temperature evolution of the fireball. At top SPS energies, the dilepton mass distribution in the intermediate mass range is dominated by radiation from a deconfined phase. The comparison of charmonium yields measured in proton-nucleus and nucleus-nucleus collisions has led to the observation of an anomalous dissociation of charmonium in central collisions of heavy nuclei which was explained by color screening in the quark-gluon phase. Till today, this observation till has remained one of the most convincing experimental facts hinting towards the existence of partonic degrees of freedom in the fireball at top SPS energies. The dilepton measurements at the CERN-SPS have been performed mainly at 158 A GeV, except for one spectrum taken in Pb+ Au at 40 A GeV by the CERES collaboration where even an increased excess yield has been observed [20]. A systematic beam energy scan in order to search for the onset of in-medium mass modifications of vector mesons or for partonic contributions to the dilepton yield has not been performed yet. With the dilepton measurements in heavy-ion collisions at FAIR energies the CBM collaboration will open a new era of dilepton experiments. Moreover, CBM will enter terra incognita: in the beam energy range between 2 and 40 A GeV where the highest net- baryon densities can be created in the laboratory, no dileptons have been measured in heavy ion collisions. The CBM collaboration will systematically measure both dielectrons and dimuons in p+p, p+A and A+A collisions as a function of beam energy and size of the collision system. The dielectron and dimuon high-precision data will complement each other, and will provide a complete picture on dilepton radiation off dense baryonic matter. Therefore, the CBM experiment has a large discovery potential both at SIS 100 and SIS 300.

Chapter 3

Feasibility studies of the CBM Muon Chamber

The compressed baryonic matter (CBM) experiment at the future FAIR accelerator center in Darmstadt, Germany, aims at the investigation of baryonic matter at highest net baryon densities but moderate temperatures, by colliding heavy-ions at beam energies from 10 to 45 A GeV. The research program comprises the exploration of basic landmarks of the QCD phase diagram like transitions from hadronic to partonic phase, the region of first order de-confinement as well as chiral phase transition, and the critical end point. The proposed key observables include the measurement of low mass vector mesons and charmonia, which can be detected via their decay into the di-lepton channel. As the leptons leave the hot and dense fireball without further interactions, hence they provide almost unscathed information about the interior of the collision zone where they are being created. In this chapter, we discuss the physics motivation, simulation methods, and the feasibility studies of the di-muon measurements for central Au + Au collisions.

3.1 Motivation for dimuon measurements at FAIR energies

Lepton pairs emitted in heavy-ion collisions are very sensitive diagnostic probe of the conditions inside the fireball because they are not affected by final-state interactions. The most interesting sources of lepton pairs are:

Low-mass vector mesons, in particular the ρ_0 meson which has a short lifetime and decays inside the fireball, change their properties in the hot and dense medium. Such in-medium modifications are expected when chiral symmetry is (partly) restored.

Thermal electromagnetic radiation - converted into lepton pairs - reflects the temperature of the fireball. Thermal lepton pairs are emitted all over the course of the collision, and, hence, provide integrated information on the temperature evolution.

Charmonium dissociation due to color screening in a deconfined medium was predicted as a signature of the Quark-Gluon Plasma [23]. Up to date, no dilepton data have been measured in heavy-ion collisions in the FAIR energy range, i.e. between about 2 AGeV (with DLS at LBL [53] and HADES at GSI [22]), and 40 A GeV (with CERES at CERN-SPS [52]). The experimental challenge in dilepton measurements is to suppress the huge combinatorial background of lepton pairs. In the case of muon measurements, the muon background is generated by weak decays of pions and kaons, by mismatches of hadrons upstream and muons downstream the hadron absorber, and by hadrons punching through the absorber.

3.2 The muon detection system (MUCH)

One of the major experimental challenges of muon measurements in heavy-ion collisions in the FAIR energy regime is the identification of low momentum muons, originating from the decay of low-mass vector mesons, in a very high particle density environment.

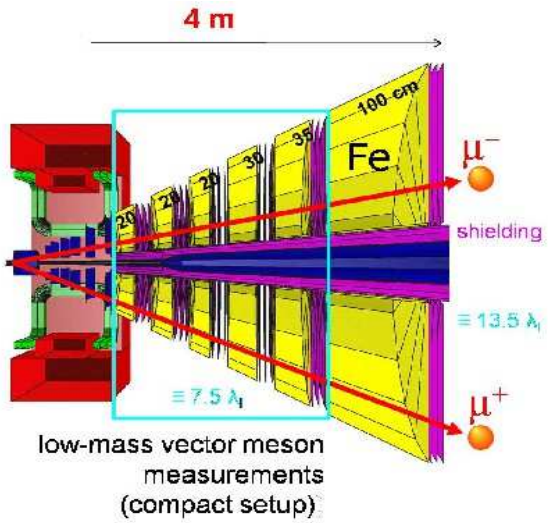

Figure 3.1. Schematic of Muon Chamber.

The novel feature of the muon detection system for the CBM [54] experiment, as compared to the muon detectors in other HEP experiments, is that the total absorber is sliced and chambers are placed in between absorbers to facilitate momentum dependent track identification. This is to improve the capturing of low momentum muons, which would have been otherwise stopped by a single thick absorber. The high efficiency for detection of low momentum muons is a prerequisite to reconstruct the low mass vector mesons in the muon chambers (MUCH). The layout of the MUCH system, i.e. the number, thickness and material of the absorber slices, and the number and granularity of the tracking detectors, has been optimized by simulating the response of the Au+Au collisions at 25 A GeV beam energy having input particles generated by the UrQMD [55] event generator. The incident particles are transported through the absorbers and the tracking chambers using the GEANT3 [56] transport engine.

3.3 Simulation methodology of MUCH

The simulation chain performed using the UrQMD event generator for input and the GEANT3 transport consists of following fundamental blocks: (a) geometry implementation and transport (b) segmentation and digitization (c) hit formation (d) track propagation in MUCH chambers and (e) selection of tracks as muon candidates. The final identification of muon tracks is part of the di-muon analysis.

3.3.1 Geometry implementation and transport

MUCH aims to study the propagation of tracks inside the segmented absorbers. The study of geometry therefore involves the implementation of conical absorbers of varying sizes placed around the conical beam pipe. Conical absorbers are used to accept the forward focused particles. The detector modules are of square profiles that are placed behind each absorber block. For effective tracking, each tracking station consists of 3 layers of tracking chambers. Each tracking layer consists of a thin support structure and an equal number of square modules are placed on two faces of the support structure. For reducing the dead-space, modules on two faces are placed in such a way that a border of the module on one side has overlap with an active zone of the module on the opposite side. The number of stations, their shape, size and number of modules are varied for optimization of efficiency and signal to background ratio (S/B) for detecting low-mass vector mesons and charmonia.

3.3.2 Digitization

GEANT3 provides the position of energy deposition inside the detector module. These locations along with the energy depositions taken together are called MUCH points. To account for realistic detector geometry, the readout planes of the modules are segmented in pads for obtaining final detectable response. The procedure of distributing the MUCH

points to pads, known as digitization involves the detailed procedure of implementing the response of the gas detector to the energy deposition inside the chamber as described in detail later. The digitization scheme is explained in detail later in this chapter. The pad dimensions are varied to reduce the pad occupancy and the multi-hit probability in a pad. In the simple digitization scheme, points falling inside a given pad area are added together to obtain a digit, and in the advanced digitization scheme, MUCH points are subjected to create primary ionization, multiplication and signal generation inside the gas volume. For the results presented here, simple digitization scheme has been used.

3.3.3 Clustering and Hit Finder

Digits are grouped into clusters using a suitable clustering algorithm. Based on the particle multiplicity and associated cluster overlap, the clusters are either broken into several sub-clusters which have been treated as hits (advanced hit finder) or each cluster is treated as one hit (simple hit finder). The centroids of the sub clusters in case of advanced hit finding or of the main cluster in case of simple hit finder is assigned to be the location of MUCH-hits which are then taken as candidates for track propagation.

3.3.4 Track propagation

Tracks reconstructed in STS are propagated using the Kalman Filter technique to pass through the MUCH layers. MUCH hits located around the propagation point are taken as the candidates of the propagated track. For final analysis, χ^2 of track fitting, number of STS and MUCH layers associated to the propagated tracks are taken as track validation parameters.

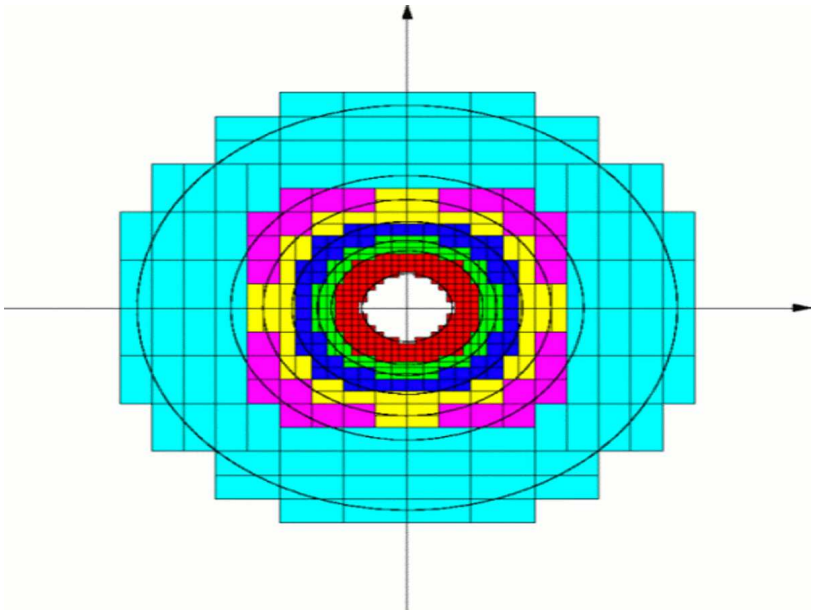

Figure 3.2. Schematic of sector in Muon Chamber simulations.

3.4 Detector segmentation, digitization, clustering and hit formation

3.4.1 Concept

system (= MUCH)

station (1-255)

sector (1-32767)

The sector is the smallest controllable unit. The schematic of sector is depicted in fig.3.2. The digitization procedure is defined by the sector type and its parameters [57]. Only one sector type (GEM detectors) is implemented yet. The channel number is fixed to 128. The station is (currently) the smallest unit represented in MC transport. This allows us to simulate different detector responses without having to run the full transport each time. In transport, a MuCh station is identified by its name

(e.g. "muchstation05"), given in the geometry file. In the digitization, the station is identified by its unique number given in the digitization file. The matching of the two is implemented by hardcoding the former naming convention. The digitization of a CbmMuchPoint is performed on the sector level by first looking up the station (through MC volume ID from TGeo), then searching for the sector the point is in. In this sector, the corresponding channel number is calculated and a CbmMuchDigi object is created.

3.4.2 The task: CbmMuchDigitize

The task performing the MuCh digitization is CbmMuchDigitize. It produces CbmMuchDigi objects out of CbmMuchPoint objects. It is instantiated with name and verbosity level:

The task has a member of type CbmMuchDigiScheme, which provides the geometry and digitization parameters on the station and sector level. The digitization scheme is initialized in the Init() function of the task.

3.4.3 Input and Output

The input for the MuCh digitization is an array of CbmMuchPoint, provided by the transport simulation. The output is an array of type CbmMuchDigi (branch name MuchDigi). The digi class contains the following information:
station number: GetStationNr();
sector number: GetSectorNr();
channel number: GetChannelNr();
The presence of a CbmMuchDigi in its array means that the respective channel is active in this event. For the coupling to Monte-Carlo data, an additional data class CbmMuchDigiMatch is created (branch MuchDigiMatch). It contains the indices of CbmMuchPoint objects (up to three) having activated a channel. There is a one-to-one

correspondence of Digi and DigiMatch by index in the respective array.

3.4.4 Procedure

Only one sensor type is implemented yet (GEM). The x and y coordinates of the point are discretised on the respective edges of the sector. The channel number is then calculated by the prescription
iChan = iRow × nColumns + iColumn

3.4.5 The Digitization Scheme

The class CbmMuchDigiScheme gives easy access to all information necessary for MuCh digitization and hit finding. The stations (class CbmMuchStation) can be accessed by index in the array (GetStation), by station number (GetStationByNr) or by MC volume ID (GetStationByMcId). There is also direct access to one sector of a station (GetSector). The CbmMuchStation knows its position in the global coordinate system, the thickness and inner and outer radia as well as the rotation around the station centre with respect to the global system. In addition, it manages an array of its sectors, accessible both by index (GetSector) and by sector number (GetSectorByNr). CbmMuchSector is the main entity for digitization. Its parameters are type, centre position and rotation in the global c.s., sector extension in x and y, pad extension in x and y. The main functionality is provided by the method GetChannel(x, y), which returns the channel number corresponding to a given coordinate pair (x,y). The digitization scheme is initialized by a call to the method Init, giving as parameters objects of type CbmGeoMuchPar and CbmMuchDigiPar.

3.4.6 Digitization Parameters

The input and output of the digitization parameters is handled by the class CbmMuchDigiPar, which is derived from CbmParSet. Similar to the digitization scheme, it holds an array of CbmMuchStationDigiPar objects, which in turn manage their CbmMuchSectorDigiPar members. The differences between CbmMuchSectorDigiPar and CbmMuchSector are:

1) The DigiPar classes are streamed to and from file (ASCII, ROOT or ORACLE).

2) The DigiPar parameters are in the coordinate system of the mother, while the DigiScheme converts these into the global coordinate system on initialization.

3) The DigiScheme classes provide functionality necessary for digitization through member functions.

The file format for ASCII I/O of CbmMuchDigiPar is:

a) one line containing [CbmMuchDigiPar].

b) a line for each station containing:

i) the station number (identifier).

ii) its rotation w.r.t the global coordinate system.

iii) the number of its sectors.

iv) followed by one line for each sector with sector number (identifier), sector type (1 - GEM), x and y coordinates of sector centre in the station c.s., rotation of the sector w.r.t the station, sector size in x and y, pad size in x and y.

3.4.7 Algorithms

There are two algorithms for producing Digis are realized. The simple algorithm and more advanced one. In the simple algorithm every pad located under the center of a track is fired (see Fig.3.3).

However such case is far from reality. The advanced algorithm for digitizing the MuCh system takes into account that one track can cause firing of several pads, if the

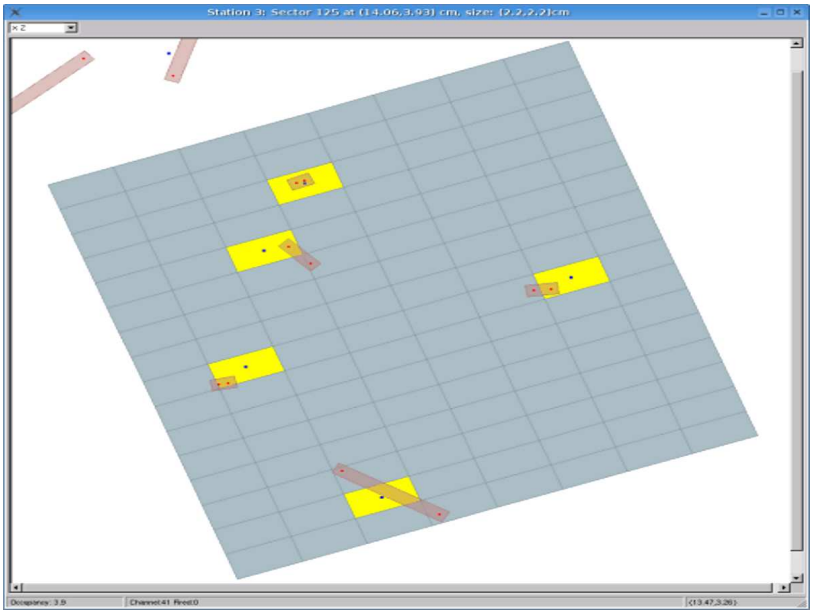

Figure 3.3. Schematic of simple digitization scheme.

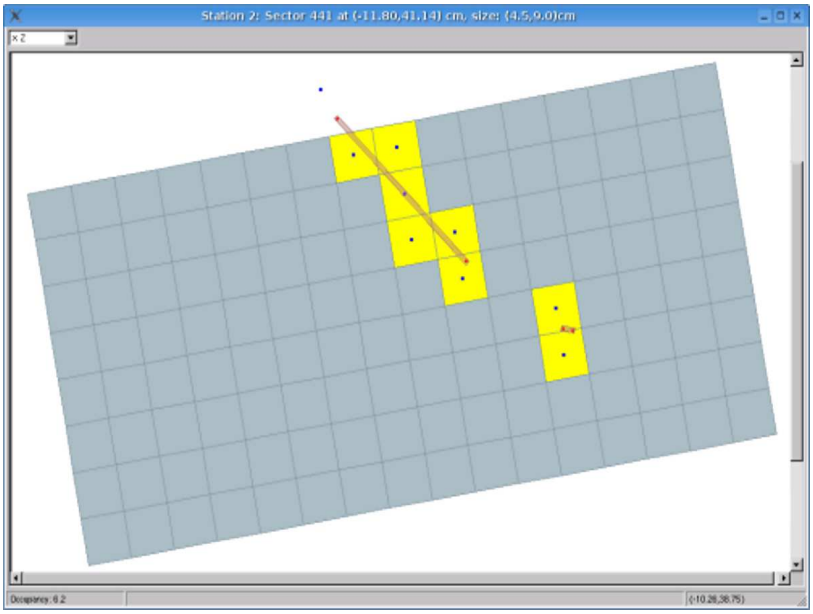

Figure 3.4. Schematic of advanced digitization scheme.

track is inclined enough (see Fig.3.4).

Whether to use the advanced algorithm or the simple one can be set by the switch SetUseAvalanche. By default the simple algorithm for digitizing the MuCh system is used.

3.5 MUCH Track Reconstruction

The main challenge of the track recognition in the CBM-MUCH detector results from the large multiplicity in heavy-ion collisions. About 1000 charged particles are produced in central Au + Au collisions at top CBM energies. This high charged particles multiplicity leads to a high track and hit density in the MUCH detector, especially on the first detector planes. Figure 3.5 shows the schematic of tracking in MUCH. The developed track reconstruction algorithm in MUCH is based on track following using reconstructed tracks in the STS as seeds. The STS track reconstruction is based on the cellular automaton method [58] and STS track parameters are used as starting point for the subsequent track prolongation. This track following is based on the standard Kalman filter technique [59] and is used for the estimation of track parameters [60] and trajectory recognition. Main logical components are track propagation, track finding, track fitting and finally selection of good tracks. Each of the steps will be described in the following in some more detail.

3.5.1 Track Propagation

The track propagation algorithm estimates the trajectory and its errors in a covariance matrix while taking into account three physics processes that influence the trajectory, i.e. energy loss, multiple scattering and the influence of the magnetic field. The influence of the material on the track momentum is taken into account by calculating the expected average energy loss due to ionization (Bethe-Bloch formula) and bremsstrahlung

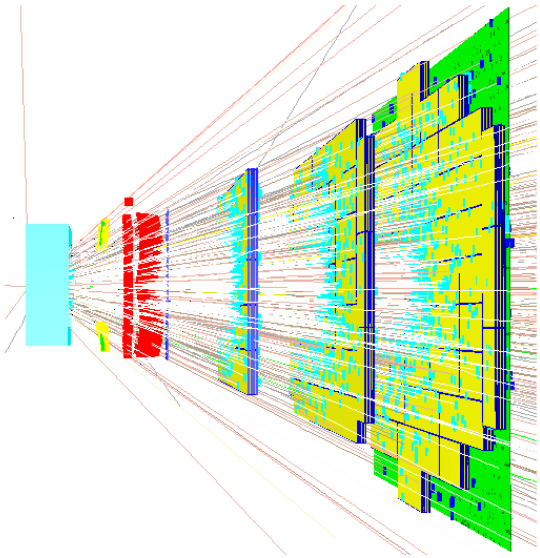

Figure 3.5. Schematic of tracking in MUCH.

(Bethe-Heitler formula) [61]. Adding process noise in the track propagation includes the influence on the error, i.e. the covariance matrix due to multiple scattering. Here, a Gaussian approximation using the Highland formula [61] is used to estimate the average scattering angle. The propagation of the trajectory is done according to the equation of motion. If the track passes a magnetic field, the equation of motion for a charged particle is solved applying the 4th order Runge-Kutta method [62]. For passing a field free region, a straight line is used for propagation and the transport matrix calculation. The transport matrix is calculated by integrating the derivatives along the so-called zero trajectory [63]. A detailed description of the developed track propagation can be found in [64].

3.5.2 Track finding and fitting

In the track finding algorithm hits are attached to the propagated track at each detector station using two different methods. Either just the nearest hit is attached to the track,

or all hits within a certain environment are included. For the first method, only one track is further propagated, the branching method allows several track branches to be followed, one for each attached hit. Common techniques to these methods are the above described track following, the Kalman Filter and the calculation of the validation region for hits. Assignment of new hits is done step by step at each detector station. After the track propagation to the next station, possible hits are attached and track parameters are updated by the Kalman Filter. For the attachment of hits a validation gate is calculated to allow a high degree of confidence in the hit-to-track assignment. The validation gate is defined based on the residual vector r (distance between the fitted track and the hit) and the residual covariance matrix R. In the context of Kalman-based tracking filters, a validation gate can be expressed as $\nu = r\ R^{-1}\ r^T < d$. The cut value d is chosen such that a defined probability of rejecting the correct hit is achieved. Here this probability is chosen to be 0.001. Values for d can be taken from χ^2 tables as a function of the on the number of effective degrees of freedom. Here the effective degree of freedom is 1 for a straw tube detector hits and 2 for pixel hits from pads in a GEM detector. The algorithm takes into account provision of missing hits due to detector inefficiencies, dead zones in the detector, inefficiency of hit finder algorithm among others. Two methods which can be chosen for hit assignment to tracks differ in the way how a situation is dealt with in which several hits lie within the validation gate. In case of the branching method, a new track branch is created for each hit lying within the validation gate. Since the number of branches can grow exponentially, the χ^2 value is calculated for each track branch and unlikely ones are rejected. Also for each input track seeds, number of created branches is calculated and if it exceeds the limit then the tracking continues using nearest neighbour approach. For the second method no track branches are created. The nearest neighbor method attaches the hit with the smallest ν, if lying in the validation region at all.

3.5.3 MUCH Reconstruction Performance

After track finding, the so called clone tracks (consisting of a very similar set of hits) and ghost tracks (consisting of a random set of hits) have to be rejected while keeping correctly found tracks with high efficiency. The selection algorithm works in two steps. First, tracks are sorted by their quality which is defined by the track length and χ^2. Then, starting from the highest quality tracks all hits belonging to a track are checked. In particular, the number of hits shared with other tracks is calculated and the track is rejected if more than 15 % of the hits are shared. The results presented here are based on studies performed with standard simulations for central Au + Au collisions at 25 A GeV beam energy. Events were generated with the UrQMD event generator [55]. In order to enhance statistics and investigate the MUCH response to primary muons, the J/ψ particles decaying into μ^+ μ^- pair were embedded into each UrQMD event. The performance of the algorithms was obtained by using information from the Monte Carlo input. During the efficiency calculation, the level of correspondence between the found and simulated tracks is estimated. A track is defined as correctly found if it has more than 70 % of hits from one Monte-Carlo track, otherwise a track is defined as ghost track. The track reconstruction efficiency is defined as Efficiency = $\mathrm{N}_{reconstructed}/N_{accepted}$. $\mathrm{N}_{reconstructed}$ is the number of correctly found tracks after reconstruction, $N_{accepted}$ is the number of reconstructable tracks in the MUCH acceptance, i.e. tracks that have at least 6 detected hits in the MUCH. Results shown here are for muon tracks since these are the most important for the muon simulations.

Fig. 3.6 and Fig. 3.7 shows the track reconstruction efficiency as a function of the momentum for MUCH and global tracking efficiency for STS-MUCH for 25 AGeV beam energy. The MUCH track reconstruction efficiency integrated over the momentum range 0-10 GeV/c is 95.9 % for nearest neighbour method and 95.8 % for branching method. The mean efficiency for tracking in STS-MUCH is 95.1 % for nearest neighbour and 94.9 % for branching method. Both methods show the same efficiency but the nearest

neighbor approach has some advantages: it is easier to implement and it is faster. This method was used by default in event reconstruction.

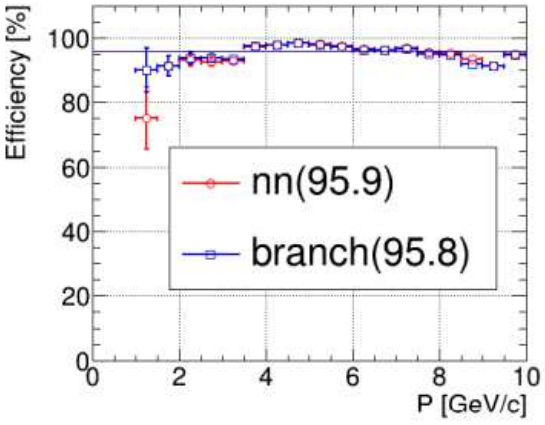

Figure 3.6. MUCH tracking efficiency. Track reconstruction efficiency for primary muon tracks from J/ψ as a function of momentum for two tracking algorithms: nearest neighbor (red) and branching (blue). Horizontal lines represent numbers integrated over momentum.

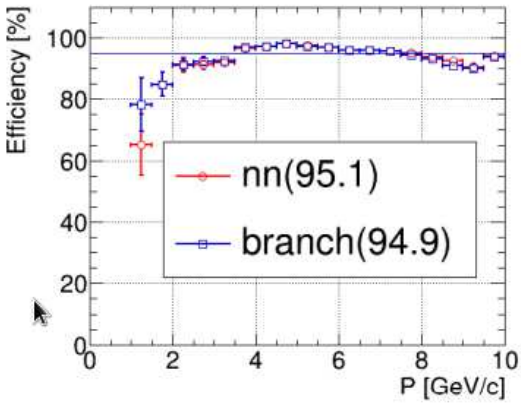

Figure 3.7. STS-MUCH tracking efficiency. Track reconstruction efficiency for primary muon tracks from J/ψ as a function of momentum for two tracking algorithms: nearest neighbor (red) and branching (blue). Horizontal lines represent numbers integrated over momentum.

3.6 Muon identification and analysis

From the global reconstructed tracks, we apply a set of cuts at the analysis level to identify muons. The aim is to reduce background due to non-muonic tracks and muons from weak decays of pions and kaons. The cuts which have been used on reconstructed tracks for selection of muon candidates are (a) from STS: number of hits in STS and χ^2 of the STS segment of the track and (b) from MUCH segment of the track: number of much layers, χ^2 of the MUCH segment of the track. Additionally, a cut on χ^2

vertex is also applied. Based on the separation power of these cuts between signal and background, we obtain a set of final cuts that have been used in this analysis for selection of muon candidates. It should be noted that for selection of muons from low-mass vector mesons and charmonia, the numbers of MUCH hits in a track are taken to be different. For example, while for low-mass vector mesons the number of MUCH layers can be up to 15, however, for charmonium it should have more than 15 MUCH hits in order to ensure that the corresponding track has traversed the thick absorber.

3.7 Optimization of cuts

We have performed various tests using MC data to evaluate the performance of MUCH. One of the first tests performed was to test the survival of different types of primary and secondary particles with the variation of cut values. As there is no muon from UrQMD output, decay muons are present only in the secondary samples. It is seen that, for a fixed reasonable cut on MUCH hits, the use of cuts using 6 STS hits and χ^2 less than 2.0 remove most of the pions and other particles without removing muons significantly. The cuts of 6 STS hits and χ^2 less than 2.0 reduce the background considerably. The use of stricter cuts (like 7 sts hits and $\chi^2 < 1$) reduces both background and signal, and does not help to improve the signal to background ratio. It should be mentioned that, for the following discussions, final efficiency results are obtained after the use of final cuts that is aimed at reducing the background in addition to increase of efficiency. The cuts used therefore works as the effect of absorbtion in addition to acceptance and track finding.

3.8 Feasibility Studies

The signals such as LMVM and J/ψ decayed into dimuon channels are generated by PLUTO [65] event generator are embedded on background events generated by the

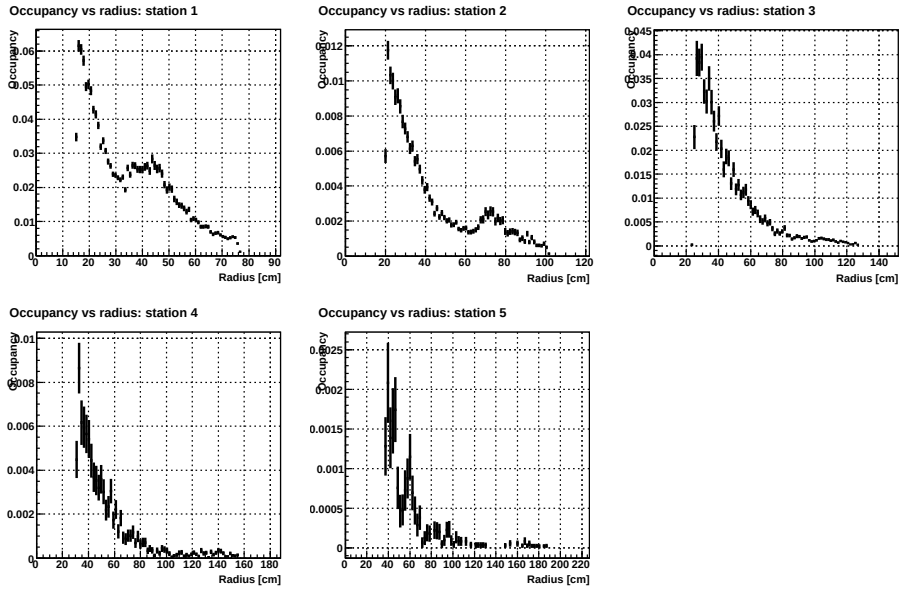

Figure 3.8. Occupancy plot for the first five stations of the muon chamber.

UrQMD [55] event generator. Both the signal and background tracks are transported through detector setup using GEANT3 within the CBMROOT [66, 67] simulation framework. The track should be reconstructed both in STS and Muon Chamber for being classified as a muon track. We have segmented the detector into pads of varying size from 4 mm $\times$ 4 mm to 3.2 cm $\times$ 3.2 cm for track reconstruction as shown in the Table 3.1. The study of segmentation is important for a) the determination of occupancy, which eventually determines the feasibility of tracking and the efficiency of muon measurements; b) the total number of pads, which influences the cost; and c) the smallest pad size, important from the point of view of fabrication and signal strength.The occupancy plot is shown in fig. 3.8 for the first five stations of muon chamber.

The reconstruction efficiency of ω and signal to background ratio were calculated in a $\pm$ 2 σ window around the signal peak and are presented in Table 3.2. for central Au-Au collisions at 8, 25 and 35 A GeV beam energies [68]. We also explored the possibility to perform muon detection with reduced (9 layer) and intermediate(12 layers) geometry (see Table 3.4) [69]. The reduced geometry consists of 3 hadron absorber layers (iron

Table 3.1. Summary of Segmentation Scheme.

Segmentation	Min Pad Size	Max Pad Size	Total no of pads
1	4mm × 4mm	3.2cm × 3.2cm	791040
2	2mm × 4mm	3.2cm × 3.2cm	989184
3	5mm × 5mm	3.2cm × 3.2cm	567459

Table 3.2. Reconstruction Efficiency and (S/B) ratio of ω in central Au-Au collision at 8,25 and 35 A GeV beam energies for different segmentations (Input events: 10k UrQMD+PLUTO) and 18 layers geometry case.

Energy (A GeV)	Efficiency (%)			S/B		
	Seg-1	Seg-2	Seg-3	Seg-1	Seg-2	Seg-3
8	0.86	0.86	0.78	1.41	1.03	0.94
25	1.58	1.61	1.43	0.49	0.497	0.3
35	1.81	1.82	1.7	0.31	0.34	0.28

plates of thickness 30 cm, 95 cm and 100 cm) and 9 layers (made of GEM) located in triplets behind each absorber (see Fig. 3.8). Here the definition of LMVM track is that it should pass through 2 layers of absorber (125 cm). The intermediate geometry consists of 4 hadron absorber layers (iron plates of thickness 30 cm, 30 cm, 65 cm and 100 cm) and 12 detector layers made of GEM and is located in triplets behind each absorber (see Fig. 3.9). Here the definition of LMVM track is that it should pass through 3 layers of absorber (125 cm). The signal to background and reconstruction efficiency for both cases were similarly calculated as for 18 layers (see Fig. 3.10) case and are shown in Table 3.3. It is evident from the Table 3.2 that different geometries with same absorber thickness but varying number of detector layers give comparable values for the reconstruction efficiency. The S/B ratio, however, is drastically different for the different geometries. Reduction in the number of stations results in a huge reduction of the signal-to-background (S/B) ratio for ω mesons, even at the lowest energy. Thus our studies indicate that as far as the measurement of low-mass vector mesons is concerned, there is practically no cheaper version of the muon detection system other than the

Table 3.3. Reconstruction Efficiency and Signal to Background ratio of ω for various energies and geometries (Input events: 10k UrQMD+PLUTO).

Energy (A GeV)	Efficiency			S/B		
No. of layers	9	12	18	9	12	18
8	0.94	0.91	0.86	0.05	0.088	1.41
25	1.77	1.95	1.58	0.00098	0.0003	0.49
35	1.85	2.13	1.82	0.00059	0.00162	0.34

Table 3.4. Specifications for the 9,12 and 18 layers geometry .

No. of stations	3	4	6
No. of layers	3×3	3×4	3×6
Total absorber thickness (cm)	225	225	225
	(30+95+100)	(30+30+65+100)	(20+20+20+30+35+100)
Distance betwen layers (cm)	10	10	10

standard geometry, which effectively comprises 15 layers for LMVM detection. Fig. 3.11 and Fig. 3.12 shows the invariant mass spectra of J/ψ and ω via dimuon channel. The mass peak of J/ψ (clean signal) and ω is only visible for 18 layers geometry case. Fig. 3.11 shows the invariant mass spectra of J/ψ. The combinatorial background is calculated using Super Event (SE) analysis technique where tracks having opposite charges from different UrQMD events are combined. The green line shown in the fig. 3.11 is exponential fitting to the background. Our studies indicate that both low mass vector mesons and charmonia can be identified above the combinatorial background, which is dominated by muons from weak pion decays.

3.9 Summary and Conclusions

We have done a systematic study pertaining to the geometry and pad sizes of the muon chamber. Designs are mostly defined by requirements of Low Mass Vector Me-

Table 3.5. Reconstruction Efficiency and (S/B) ratio of J/ψ and ω in central Au-Au collision at 8, 25 and 35 A GeV beam energies (Input events: 10k UrQMD+PLUTO) and 18 layers geometry case. The optimized segmentation scheme 1 as shown in Table 3.1 has been used for the estimation of reconstruction efficiency and (S/B).

Energy (A GeV)	Efficiency (%)		S/B	
	J/$\psi\rightarrow\mu^+\mu^-$	$\omega\rightarrow\mu^+\mu^-$	J$\psi\rightarrow\mu^+\mu^-$	$\omega\rightarrow\mu^+\mu^-$
8	4.9	0.86	3.3	1.41
25	13	1.58	7	0.49
35	13	1.82	11	0.34

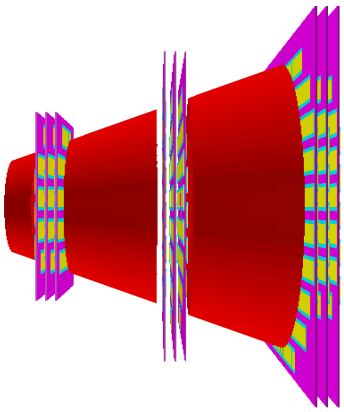

Figure 3.9. Schematic of nine layers geometry.

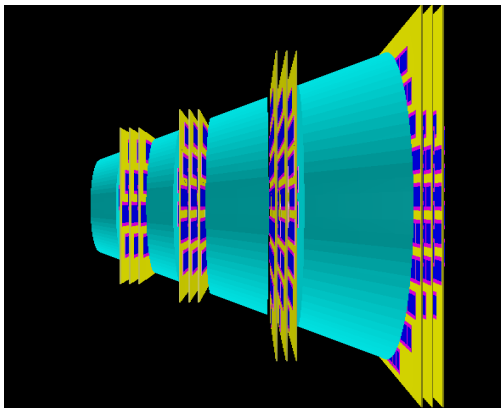

Figure 3.10. Schematic of twelwe layers geometry.

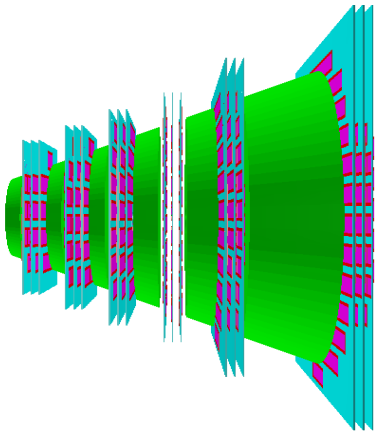

Figure 3.11. Schematic of eighteen layers geometry.

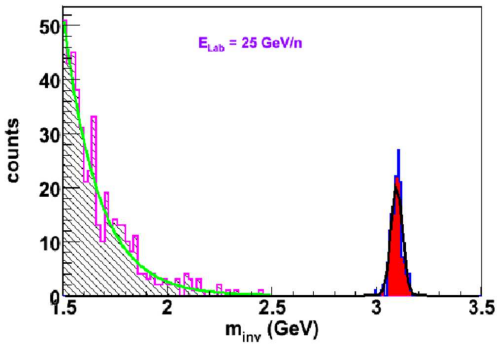

Figure 3.12. Invariant mass spectrum of J/ψ at 25 A GeV.

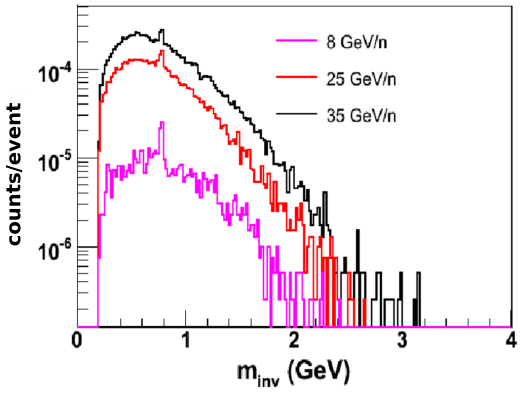

Figure 3.13. Invariant mass specta of ω at various energies.

son (LMVM) measurements. Charmonium measurements (with additional 1 m Iron absorber) are less sensitive to the configuration details. Simulations of both lowest (minimum boost) and highest energy (maximum multiplicity) are performed. Even at the lowest energy there seems to be no inexpensive version capable for measurements of low mass vector mesons (LMVM). Segmentation with minimum pad dimension 4 mm $\times$ 4 mm is a suitable choice, given the fact that pads of this size are relatively easy to fabricate.

Chapter 4

Gas Electron Multiplier for CBM Muon Chamber

In the last chapter we have dealt with optimization of the pad sizes and geometry for the muon chamber. For the simulation studies we have used gas electron multiplier (GEM) for the stations of the muon chamber. Gas electron multiplier have been proposed for the first few stations of muon chamber in the CBM experiment. We begin this chapter with the interaction of particles with matter. Next, this chapter illustrates the research and development on GEM and addresses the analysis of measurements of cosmic muons as well as X-rays from a Fe^{55} source. The first prototype has been built with the intention of learning about development and commissioning of such a detector from the very beginning. The following section illuminates the testing of triple GEM using self triggered electronics in terms of efficiency, cell multiplicity, timing and pulse height spectra.

4.1 Interaction of Particles with Matter

4.1.1 Charged Particles

Charged particles, traversing a gaseous medium, lose energy mainly by the electromagnetic interaction since it is orders of magnitudes more probable than strong or weak interactions. Incoherent Coulomb interactions between the electromagnetic fields of the

traversing charged particles and of the material lead to both excitation and ionization of the atoms of the medium. The energy loss due to other electromagnetic processes, such as transition radiation, Cherenkov radiation and bremsstrahlung can be neglected [70].

With the aid of relativistic quantum mechanics Bethe and Bloch described the average differential energy loss per unit length by excitation and ionization with the following expression [71]:

$$-\frac{dE}{dx} = 2\pi N_A r_e^2 m_e c^2 \frac{(z)^2}{\beta^2}[\ln(\frac{2mc^2\beta^2\gamma^2 W_{max}}{I^2}) - 2\beta^2 - \delta - \frac{2C}{Z}] \tag{4.1}$$

r_e : classical electron radius, m_e : electron mass, N_A : Avogadros number, I: mean excitation potential, Z: atomic number of absorbing material, A: atomic weight of absorbing material, ρ: density of absorbing material, z: charge of incident particle in units of e, β = v/c of the incident particle,$\gamma = \frac{1}{\sqrt{1-\beta^2}}$, δ: density correction considering the shielding effect of polarized molecules, C: shell correction accounting for effects arising if the particle velocity is comparable to or smaller than the orbital velocity of the bound electrons, W_{max} : maximum energy transfer in a single collision.

However, the Bethe-Bloch formula does not apply to electrons and positrons, because their small mass leads to a domination of bremsstrahlung at high energies. Furthermore, the indistinguishability of the electrons in the shell of the target atom is a reason for this invalidity of the Bethe-Bloch equation for electrons. This can also be seen in figure 4.1, where electrons show a complete different behavior in contrast to the other particles following the Bethe-Bloch formula. The Bethe-Bloch formula describes the average differential energy loss per unit length, around which the actual energy loss per path length δx is statistically distributed. This distribution follows a Landau distribution with its maximum below the average.

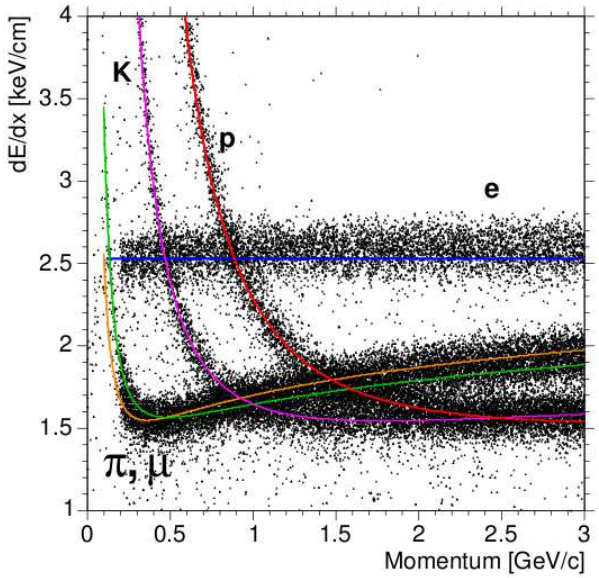

Figure 4.1. Specific energy loss for charged particles.

4.1.2 Photons

There are three predominant processes, in which high energetic photons can interact with matter: the photo effect (complete absorption of a photon by an electron of the atomic shell), the Compton scattering (elastic scattering by a quasi free atomic electron), and the pair production (production of an e^+ e^- pair in the Coulomb field of the atomic nucleus). Thus, the interactions of photons with matter basically differ from ionization processes of charged particles, since the photon either loses its energy all at once (photo effect, pair production) or is scattered under relative huge angles (Compton scattering) at each photon interaction process and its energy is consequently well localized.

The probability for a photon to interact in one of these ways depends on the atomic number of the absorbing material and on the energy of the incoming photon. For energies $>$ 10 MeV pair production prevails, for 100 keV $<$ E_γ $<$ 10 MeV the Compton scattering preponderates, and for $E_\gamma <$ 100 keV the photoeffect is dominant. For the radioactive source Fe^{55} with an energy of $E_\gamma = 5.89$ keV used for measurements

in this work and the chosen detector gas Argon/CO_2 70/30, the photo effect dominates.

The intensity of a photon beam gets weakened in material according

$$I = I_0 e^{\mu x} \tag{4.2}$$

Here, I_0 is the original intensity, x is the distance in material and μ is the mass absorption coefficient with $\mu = N/A\sigma$, where A is the mass number, N_A the Avogadro number and σ is the cross section [72].

4.1.3 The photo effect in Argon-Carbon dioxide gas mixture

The triple GEM detector used for the studies in this work is filled with Ar/CO_2 with a mixture ratio of 70% Argon to 30% CO_2 . Therefore, the physical processes in Argon will be discussed. A photon with an energy E_γ, hitting a gaseous atom, will kick out a shell electron, whose binding energy E_B in comparison to the other electrons is marginal smaller than the energy of the photon E_γ . For the used Fe^{55} source with $E_\gamma = 5.9$ keV or the copper X-ray tube with mainly E = 8.0 keV and Argon as detector gas in both cases, an electron from the K-shell with $E_B = 3.2$ keV will be released. Then this electron gets a kinetic energy of 2.7 keV or 4.8 keV and produces further ionization. There are two possibilities for the excited atom to return to its ground state. Either the transition of an electron of a higher shell into the K-shell by emitting a fluorescence-photon. This photon has an energy less then E_B and therefore has a broad reach. Thus it is possible that this photon leaves the detector without any interaction. This process takes places with a probability of 15 %. The more probable solution for the excited atom is an internal rearrangement involving several electrons from the lower shells, with the emission of an electron of an energy very close to but smaller than E_B . This process is called Auger-Effect and with 85 % it is much more probable than fluorescence. The Auger-electron and the primary ionized electron have together nearly the whole energy,

deposit by the photon in the detector.

Both physical processes can be shown in histogram, represent together the spectrum of the iron source Fe^{55}. This spectrum includes two maxima, the main peak, with a weighting of 85 % and a second one, the escape peak. This smaller maxima, shifted to a lower energy level and weighted with 15 %, represents the fluorescence process. Such spectra recorded with the triple GEM detector are presented later in this chapter. The total number n of ionized particles can be expressed by

$$n = \frac{\Delta E}{W_i} \tag{4.3}$$

with ΔE being the total energy loss in the gas volume considered and W_i being the effective average energy to produce one pair. Due to the fact that in gases beside ionization also excitation, i.e. electrons are lifted to higher shells without creation of an electron-ion pair, occurs, the effective ionization potential to produce one electron-ion pair is larger than the ionization energy. For instance for Argon, W_i = 26 eV and the ionization energy is 15.8 eV. Here, a weighted average value of W_iAr and $W_i CO_2$ was used for W_i : With the given ratio of Argon/CO_2 of 70/30 and W_iAr = 26 eV and $W_i CO_2$ = 33 eV [70] follows: $W_i = 0.7\ W_i\text{Ar} + 0.3\ W_i CO_2 = 28.1$ eV.

Thus, a photon of the Fe^{55} source creates ionized particles as

$$n = \frac{5.9\ keV}{28.1\ eV} \approx 210 \tag{4.4}$$

4.2 Gas Electron Multiplier (GEM)

A new concept of gas amplification, the Gas Electron Multiplier was developed by Fabio Sauli at CERN in 1997 [74]. It is a micro pattern gas detector, which has been developed to an efficient tracking device suiting to high count rates and achieving very

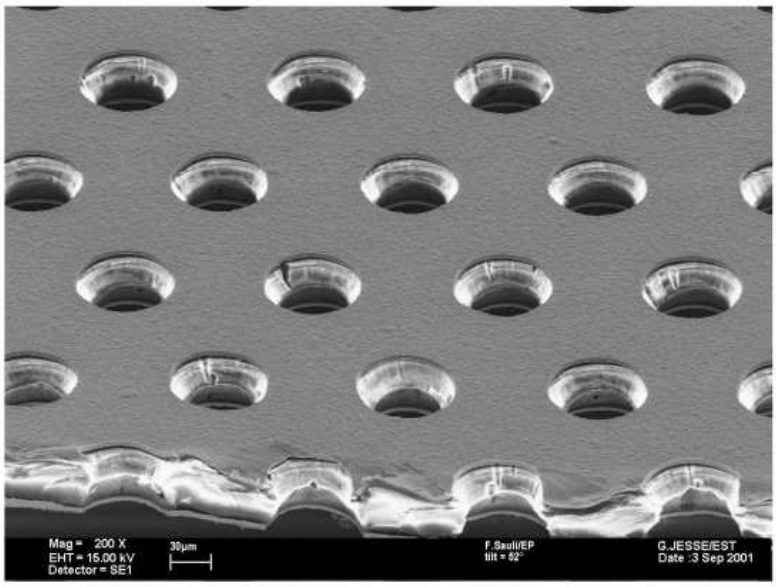

Figure 4.2. Electron microscope picture of a standard-design GEM with a hole.

precise spatial resolution. The GEM foil consists of a thin electrically insulating foil, which is covered with a very thin metal layer on both sides. It is perforated by a large number of regularly arranged circular holes. Typically, the isolating foil is a 50 μm thick Kapton [75] foil coated on both sides with a 5 μm thin copper layer. Figure 4.2 shows the schematic view of the geometric parameters of a GEM with standard-design. The outer hole diameter D is 75 μm, the distance between the holes, the pitch P, is 140 μm and the inner diameter d is 65 μm. There are about 10^4 holes per cm^2 . The GEM foils are manufactured at CERN with the help of lithographic methods [76] . In order to create those holes in the foil, their pattern is first engraved in the metal surface and then etched from both sides with a Kapton specific solvent resulting in the double conical shape of the holes. The so produced Kapton tips prevent shortcuts between the two copper electrodes. An electron microscope image of a GEM foil with such a standard geometry used at COMPASS and in the triple GEM detector can be seen in Figure 4.2.

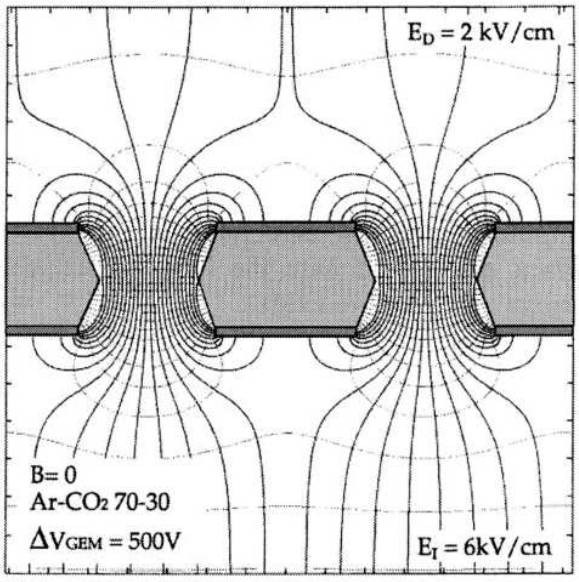

Figure 4.3. Field lines inside GEM holes.

4.3 Operation of the GEM Foils

If a sufficiently high potential difference is applied between the two copper electrodes of the GEM foil, a high electric field is produced inside the holes making gas amplification possible. With a typical voltage difference of $\approx$ 400 V one can reach a field of $\approx$ 50 kV/cm [77]. If the GEM, applied with voltage, is placed in a homogeneous electric field perpendicular to its surface created by two external electrodes with a suitable high voltage, one gets a single stage gas amplifier with a drift field between cathode and GEM, an amplification region inside the GEM holes and an induction field between GEM and anode. In figure 4.3 one can see a calculation of the electric field lines inside the GEM holes with an asymmetric external field configuration, a low drift field and a higher induction field. An electron produced in the drift region above the GEM foil by an ionizing particle, that shall be detected, drifts along the field lines into a hole of the GEM, where due to the high electric field inside the GEM holes gas amplification takes place. The created cloud of electrons leave the GEM on the other side following the

field lines of the external field. Then, the produced electrons can either be amplified by a further GEM foil or collected for detection. For this, a readout plane with pickup electrodes can be used as anode below the last GEM. The movement of the extracted electron cloud drifting along the field lines between the last GEM in a GEM stack and the readout plane induces a negative current signal in the readout electrodes. Since most of the ions created by the amplification in the GEM holes are collected onto the GEM electrodes, they do not contribute to the induced signal. Thus, the signal is mainly determined by electrons leading to a fast rise time because of the high drift velocity of electrons. With a single GEM foil gas amplification with a gain above 10^3 can be realized [78]. By increasing the GEM voltage, one could even reach a higher gain. But the stability of a GEM decreases and the discharge probability increases with a higher GEM voltage. By using multiple GEM structures - a so called GEM stack -, one can achieve high gains while the voltage applied on each single GEM is on a same level and so the discharge probability is reduced. A gain in the order of 10^4 can be reached with the detector being stable by such a multiple structure of GEMs [79]. The electric fields between the GEM foils are called transfer fields.

4.4 Why GEM's ?

GEM's have advantage over traditional wire amplification. The main advantage is that there are no wires to break. Another advantage is that GEM's prevent positive ions from drifting in to the detection region and causing field distortion by the accumulation of static charge. GEM's have the advantage that their electric field is more uniform than the field from a trditional wire detector. The electric field from a wire is E $\propto$ 1/r, whereas electric field in GEM is roughly uniform except the perturbations from the holes. Figure 4.4 illustrates how this is implemented in the case wire chambers and GEM's [80]. Another advantage of GEM's is that they can be cascaded to achieve gains 10^4 at stable operating conditions.

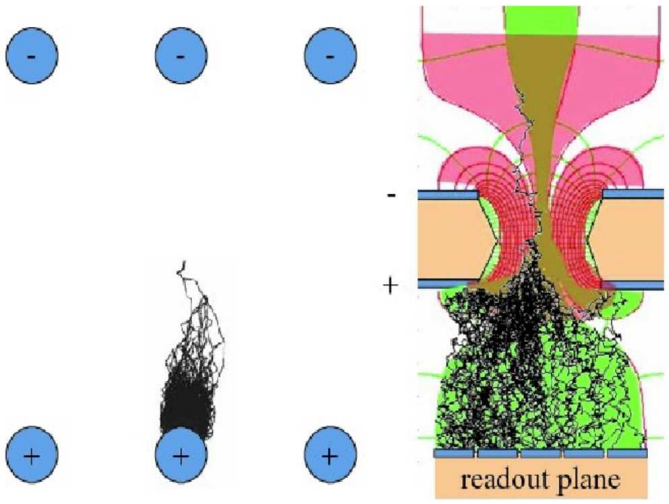

Figure 4.4. Working principle of MWPC(left) and GEM(right). Electron avlanches as simulated by Garfield [81] are shown for both the technologies; black paths are electron trajectories, the drift ions is not indicated.

4.5 GEM in past, present and future experiments

Originally GEM's were used as a preamplification stage for MSGC's, but nowadays GEM's are used as detectors themselves, read out by strips, pads or a metal plane. GEM's still suffer from discharges, but this can be considerably improved by cascading the GEM's and permitting all of them to work at a lower gain (3 GEM's with gain 20 yield a total gain of 8000). A big advantage of GEM's is that they conserve the original ionisation pattern. Because of this, the readout system can be designed independently from the GEM structure and in such a way that it suits best the use of the detector. Hexaboard read-outs, cartesian and non-cartesian strip structures have been used for this purpose and even a combination of both will be implemented in the new TOTEM [82] detectors. The decoupling of the amplifying structure and the read-out board is also one of the big GEM advantages. This construction protects the electronics from discharge damage. GEM's also have the natural tendency of suppressing

ion feedback, making them very interesting for Time Projection Chamber. Despite the good results obtained with the multi-wire proportional chambers in high-energy experiments, their limits were, like mentioned before, more or less reached in the 80s. At that moment the new generation of gaseous detectors was not yet developed and thus the future detectors were unlikely to be found in the gas detector family. Even the micro-strip gas chamber would probably not have saved the day, since it is quite vulnerable to discharges. Therefore at that moment, new detectors with improved resolution and radiation hardness were developed: the silicon micro-strips. Space coordinates with microns accuracy suddenly became available. An additional advantage of silicon detectors was the concurrent development of low cost, highly integrated electronics. nMOS and CMOS-technology were used to design low-noise and low-power signal processors for the new generation of experiments. The design studies for the Large Hadron Collider (LHC) at CERN also started in the eighties and therefore it seems logical that the LHC experiments mainly use solid-state detectors. Gaseous detectors have nevertheless still their use in todays experiments. The excellent performance of silicon detectors also carries an impressive price tag along. Due to their spatial resolution of a few micrometers and their high rate capability, they are very well suited for the area close to the interaction point. However, at large radius where also large areas have to be covered, like in the muon chambers, gaseous detectors are still the best option. At intermediate distance, silicon detectors and the micro-pattern gas detectors seem to be almost interchangeable, since they fulfill both the requirements for precision, rate capability and radiation hardness. Therefore the LHC experiments did not cast out gaseous detectors completely. ATLAS [86], CMS [87], LHC-b and ALICE [88] all use gaseous detectors for their muon chambers, since these have to cover a large surface. Also for particle tracking the gaseous detectors still play an important role. Some examples of gaseous detectors used in the LHC experiments are the ATLAS Transition Radiation Tracker (TRT), the ALICE Time Projection Chamber and the Muon Cathode drift Chambers. Figures 4.5 - 4.10 demonstrates GEM's being used in various experiments. GEM de-

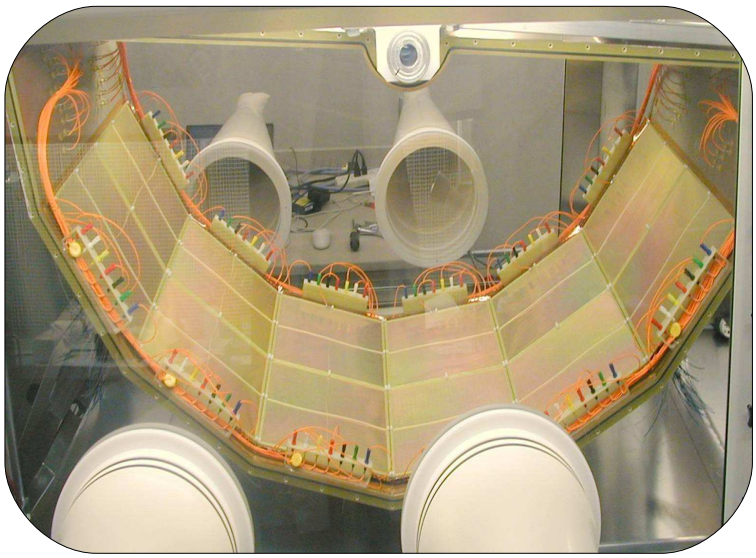

Figure 4.5. PHENIX HBD detector [83].

tectors in particular are used in two of the relatively more recent CERN experiments. TOTEM, which will measure the total proton-proton cross section, will use GEMs for tracking. LHC-b [89] uses triple-GEM detectors in the innermost region of the muon detectors because of the higher beam intensity there. In the rest of the muon chambers MWPCs are still used.

GEM's were first used in a fixed target experiment, COMPASS [84], at CERN. COMPASS uses a triple-GEM detector in the small-area-tracker. After 4 years of operation, the detectors still seem to work perfectly. An other high-energy experiments using GEM's is the PHENIX upgrade at Brookhaven National Laboratory. The main future use of GEM's seems to lay in Time Projection Chambers (TPC's). The reduced ion back flow in GEM detectors, together with increased robustness, fast signals and better two-track resolution, seems to favor this kind of detectors for these applications. Some experiments (like LEGS and BoNuS) already adapt or plan to adapt GEM-TPC's and the concept is also heavily under study for the the next generation of linear colliders, like the International Linear Collider (ILC).

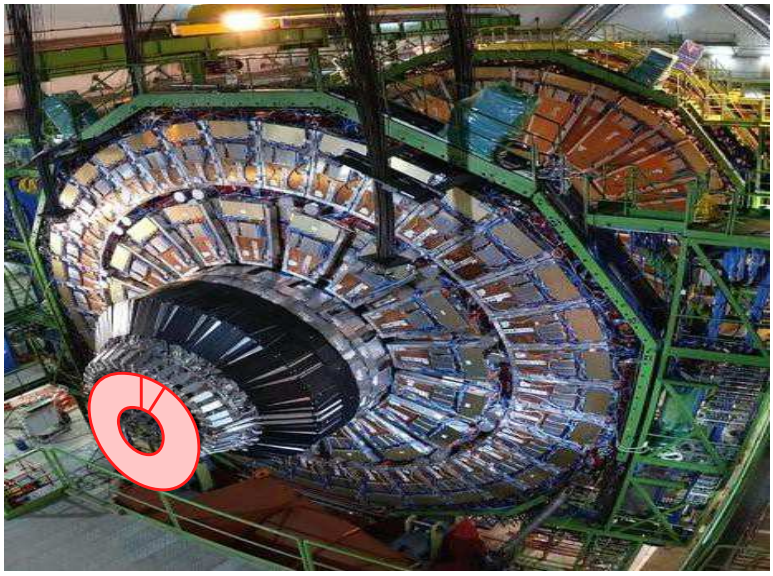

Figure 4.6. The CMS muon system upgrade.

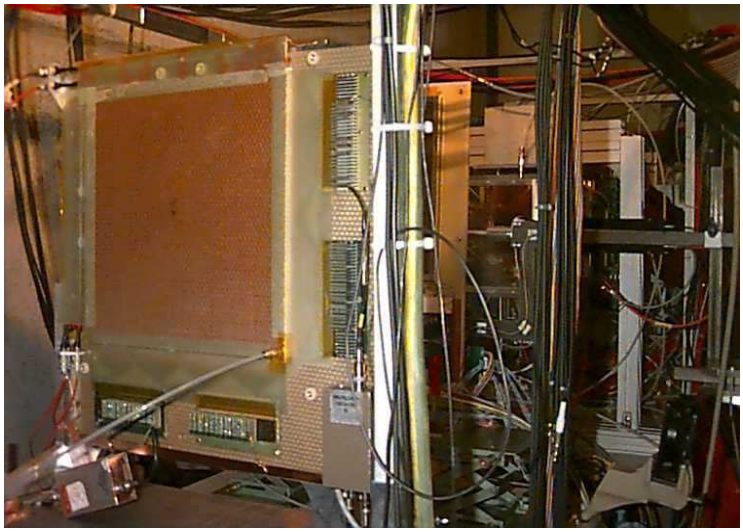

Figure 4.7. COMPASS GEM detector [84].

Figure 4.8. The NA61 GEM detector [85].

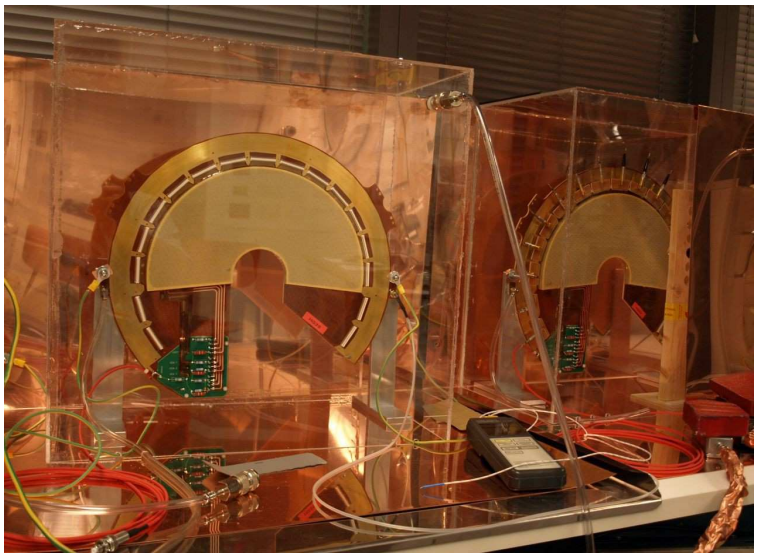

Figure 4.9. The TOTEM GEM detector [82].

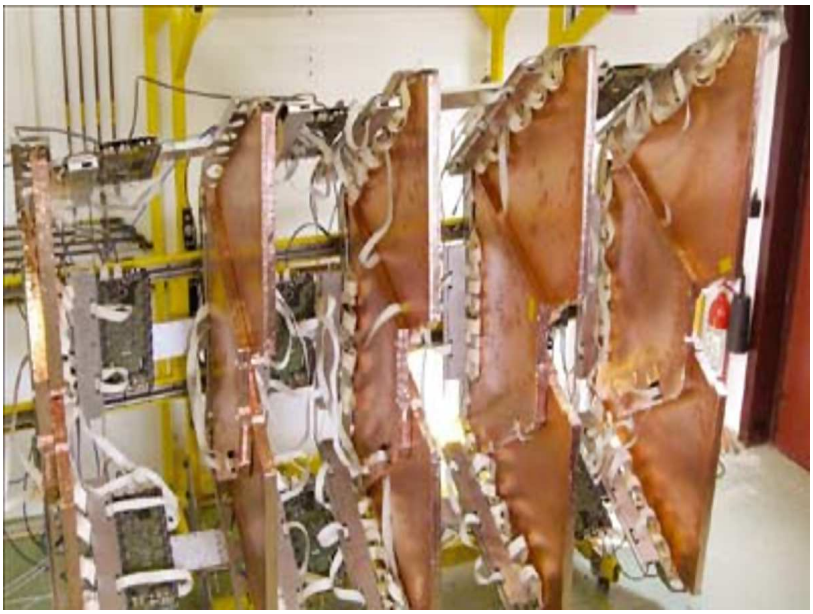

Figure 4.10. A T1 quarter of TOTEM [82].

4.6 Testing of triple GEM using conventional NIM electronics

Several multistack GEM chambers have been built and tested at VECC. We started our GEM R&D with a 10 cm × 10 cm CERN-made foil and carried out the stretching locally at VECC,Kolkata,India employing thermal stretching technique using infrared lamps. A double GEM stack thus built was successfully tested with X-ray source [90]. Subsequently, for the rest of the studies using triple GEM prototypes, we have used framed GEM foils of identical active area, procured from CERN. We report the performance test of such a triple GEM chamber using Fe^{55} source and cosmic muons. One of the desired criteria of the muon detector is that the charged particle detection efficiency has to be higher than 90 %. The cosmic-ray test in VECC lab was aimed at determining this efficiency using minimum ionizing particle (MIP). The schematic of the triple GEM chamber assembly carried out at VECC, is shown in Fig. 4.19. Three GEM frames were stacked in a 12 cm × 12 cm × 10 mm perspex frame. The readout

plane consisted of segmented pads, each of 4 mm × 4 mm, spanning in total an active area of ≈ 10 cm × 10 cm. All the pads were shorted together to obtain a single output from the chamber. The GEM layers and drift plane was powered using a resistive chain which was located outside the gaseous volume and kept very close to the perspex frame. The GEM's were biased in a symmetric configuration where in each GEM had the same ΔV across the top and bottom surfaces for any particular HV setting. The experimental setup for the cosmic ray test at VECC are shown in fig. 4.11 and fig. 4.12.

Figure 4.11. GEM detector under test with cosmic MIP's at VECC.

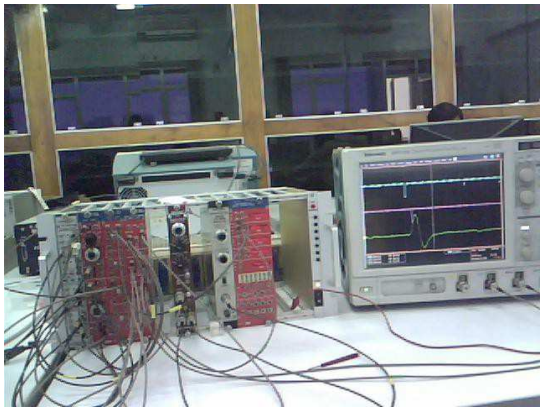

Figure 4.12. NIM modules and Oscilloscope used for testing of GEM using cosmic muons.

The detector signal was coupled to conventional NIM electronics (Ortec 142 IH preamplifier and Ortec 572A amplifier). A single channel analyzer (SCA) was used to produce the corresponding analog and logic signals.The analog output was fed to a multichannel analyzer (MCA). Suitable threshold was put on the SCA window for noise reduction. A premixed gas mixture of Ar/CO_2 in the ratio of 70/30 was used for all our tests.

4.6.1 Testing with Fe ^{55} X-ray source

Fig. 4.13 shows the schematic of testing of triple GEM with Fe^{55} X ray source. Fig. 4.14 (left) shows the Fe^{55} spectrum from a triple GEM chamber as acquired using a MCA.

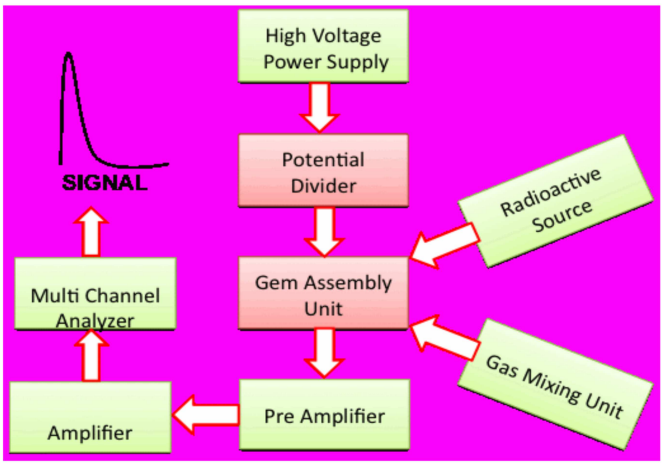

Figure 4.13. Schematic of testing of triple GEM with Fe^{55} X ray source.

Two X-ray peaks are clearly visible, with the one at higher channel corresponding to 5.9 keV. The effective detector's gain G_{eff} is the ratio between the number of electrons at the end of the triple-GEM amplification process and the number of the primary ones. $G_{eff} = N_{el} / N_p$, where N_{el} is the amount of the electrons in the induction gap, which generate the outgoing signal and N_p is the amount of primary electrons, produced in the drift zone by ionization. The gain of the chamber is seen to vary exponentially with the voltages across the GEMs as shown in Fig. 4.15 (right) and reaches about 8 $\times$ 10^4 at the highest voltage studied. A drift gap of 3 mm, transfer gap of 1 mm and an induction gap of 1.5 mm were the configuration parameters for this chamber.

4.6.2 Testing with cosmic muons

For the tests with cosmics, an assembly of three paddle scintillators was set up. A separate triple GEM test chamber consisting of 512 pads was built for these tests. The drift gap, transfer gap and induction gap for this prototype chamber was 5 mm, 1

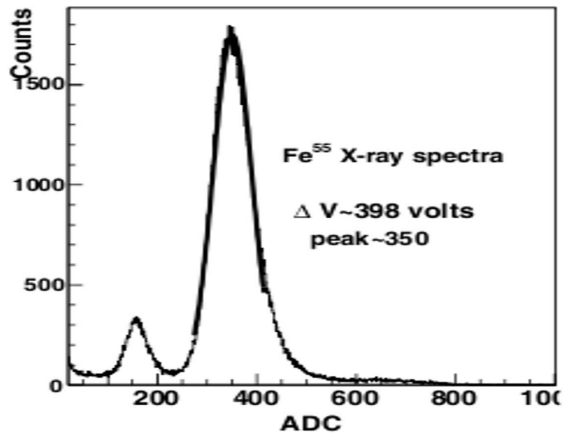

Figure 4.14. Fe^{55} Spectra of triple GEM.

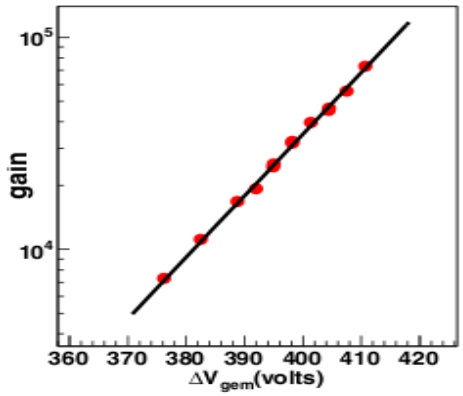

Figure 4.15. Gain of triple GEM with ΔV_{GEM}.

mm, 1.5 mm, respectively. One of the scintillators having an area of 5 cm × 5 cm kept very close to the detector determined the actual overlap area. The three fold coincidence from the scintillators provided the cosmic muon trigger, while the detector signal coupled to this produced a 4-fold coincidence. The two coincidence outputs were then fed to a scaler. The ratio of the 4-fold to 3-fold coincidence counts gave the efficiency of the chamber. A typical pulse height spectra corresponding to cosmic muons (MIP) and fitted to a Landau distribution for a particular voltage setting is shown in Fig 4.16. Fig.4.17 shows the variation of efficiency with total bias voltage. The maximum efficiency achieved is around 95 % and is found to saturate around ΔV_{GEM} of 426 V. The typical transfer and induction fields at this setting were 1.55 kV/cm and 2.84 kV/cm respectively. It needs to be mentioned that the optimization of the gaps in CBM-MUCH is a matter of further study.

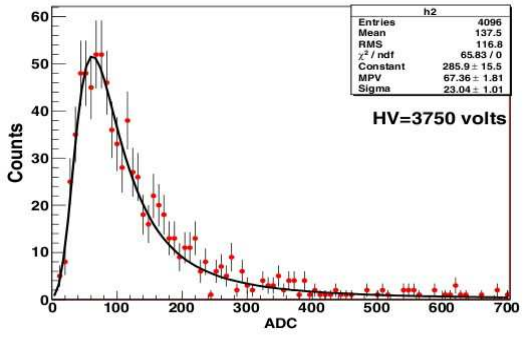

Figure 4.16. Typical pulse height spectra of cosmic muons for HV = 3750 V.

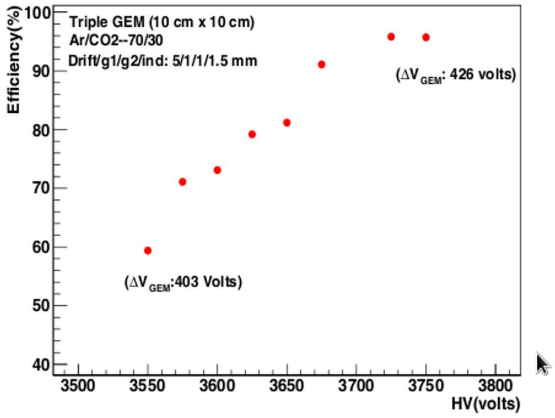

Figure 4.17. Efficiency of triple GEM with Voltage.

4.7 Testing of triple GEM using self triggered electronics

In CBM experiment at FAIR, muons will be detected by a system of six absorber layers of varying thickness and each absorber is followed by a tracking layer triplet.The details of the muon chamber are discussed in Chapter 3. A set of silicon tracking stations (STS) placed inside a dipole magnet reconstruct the charged tracks. The tracks are then projected outside the magnetic field onto the muon chambers to identify muons. Unlike other conventional muon detection systems in high energy physics experiments, the absorbers in CBM-MUCH is sliced to track muons of varying momenta including very low momentum muons.

The CBM experiment at FAIR aims at understanding the nuclear matter at highest baryonic density expected to be produced in high energy heavy ion collisions. The focus of CBM is to probe the matter with the heavy flavour quarkonia states produced at the early stage of the collisions. The low production cross-section of such states at FAIR energy demands an unprecedentedly high beam intensity at FAIR so that a reasonable statistics could be obtained at a short data taking period. Additionally, the

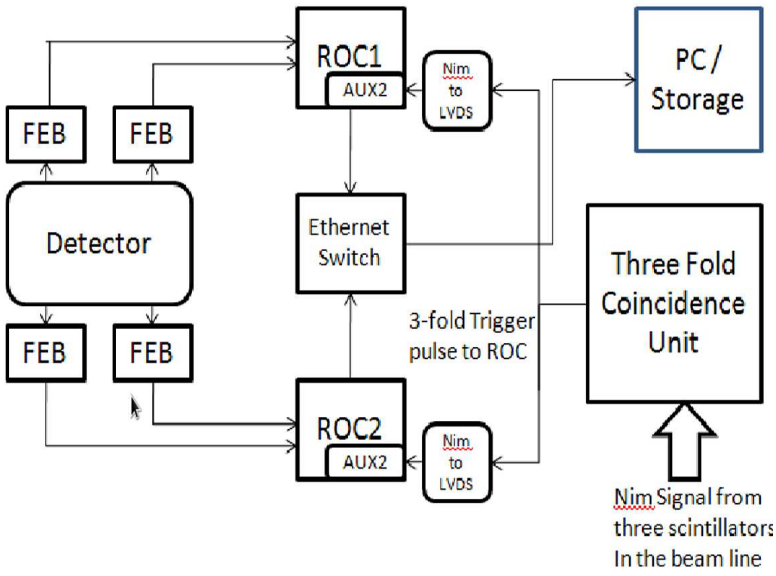

Figure 4.18. Schematic of the readout and DAQ setup.

particle multiplicity of the high energy heavy ion collisions at FAIR energy is high and those particles while passing through the absorber generate secondaries resulting the tracking chambers to face particles of $1/cm^2$ rate. At CBM heavy ion collisions, the first muon chamber will require to operate at a particle rate of 10 MHz/cm^2 . Considering he reported usefulness of the GEM chambers in such an environment, it has been decided to use triple GEM detectors in first few stations of MUCH. It has been reported earlier that the triple GEM chambers can be operated in pion beam at a rate of 10^5 Hz/mm^2 giving 95 % efficiency. The reported spark probability at such an operating voltage is 10^{-11} . With the advent of the single-mask GEM technology, large size GEM chambers each of 50 cm in width and 1 m in length could be produced, which are suitable for the applications in CBM muon system. In addition to the above mentioned detector-specific requirements, operation of CBM-MUCH at high interaction rate (10MHz) requires the use of a self-triggered readout electronics. This requirement is guided by the fact that at this high rate of interaction, a good fraction of events are likely to be missed during the time to be taken for trigger decision. In this type of readout system, no external event

trigger is applied and all hits above a predefined threshold are recorded alongwith their corresponding arrival time stamps. For testing a detector using such a readout system, signals from the coincidence of the trigger detectors along with their time stamps are also recorded separately. While the time stamps of the detector hits generated by trigger particles will be correlated to the time stamp of the coincidence trigger but the hits generated by noise will not be correlated. For most of the detector tests at CBM, a self-trigger readout system based on a 128-channel ASIC, called nXYTER [92] which was used earlier by the DETNI collaboration is being used. This ASIC has two independent pulse-processing channels with different peaking times, the fast channel of 30 ns peaking time constant provides the time-stamp of the hits after the discriminator and the slow channel of 140 ns peaking time constant is used for signal amplitude measurement using a peak detection and hold circuit. The ASIC shows a time-jitter smaller than 4 nano-seconds for 8 X 10^3 electron input charge improving to 2 ns at 10^4 electron input. A 12-bit ADC of 25 fC dynamic range is used on the Front End Board (FEB) each of which houses one nXYTER ASIC. The block-diagram of the readout system is shown in Fig. 4.18, in which the detector is directly connected to the Front End Board. The data transfer and control operations are performed by a ReadOut Controller (ROC) board. One ROC board can handle at the most two FEBs. As a part of the R&D effort for CBM-MUCH, we have built several triple GEM chambers of varying design parameters. The chamber described in [90] is a gas-tight enclosure, in which different electrode layers are housed inside a perspex frame as shown in Fig. 4.19. The top plane, known as the drift plane, is made of single-sided copper-clad kapton foil affixed on a FR4 frame which was placed as top lid. Three framed GEM foils each of 10 cm $\times$ 10 cm size, procured from CERN were placed inside the perspex container. The readout anode plane is made of a PCB, in which the inner side is etched into 512 cells each of 3 mm $\times$ 3 mm size. The cell-dimensions of the prototype chamber corresponds to the optimized smallest allowed cell-size in the first GEM station at CBM as obtained by detailed simulation in the CBM framework. The readout plane was a 4-layer PCB,

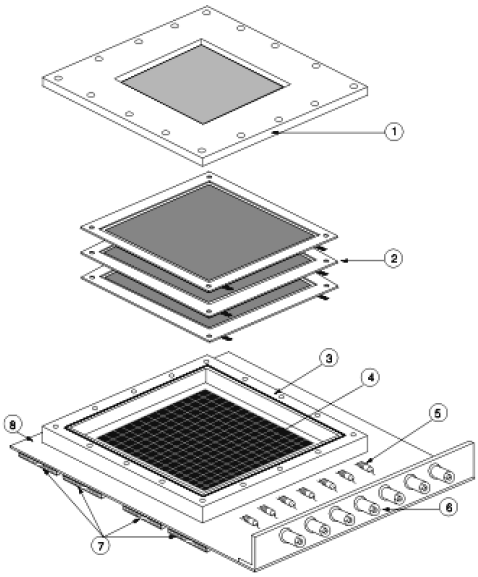

Figure 4.19. Schematic of a assembly of triple GEM chamber. (1) top chamber lid with drift plane (2) triple GEM foils stretched in FR4 frames (3) gas tight housing frame with 'O' ring seal (4) readout plane (5) GEM series resistors (6) SHV connectors for individual GEM foil bias (7) input connectors to FEB (8) readout PCB.

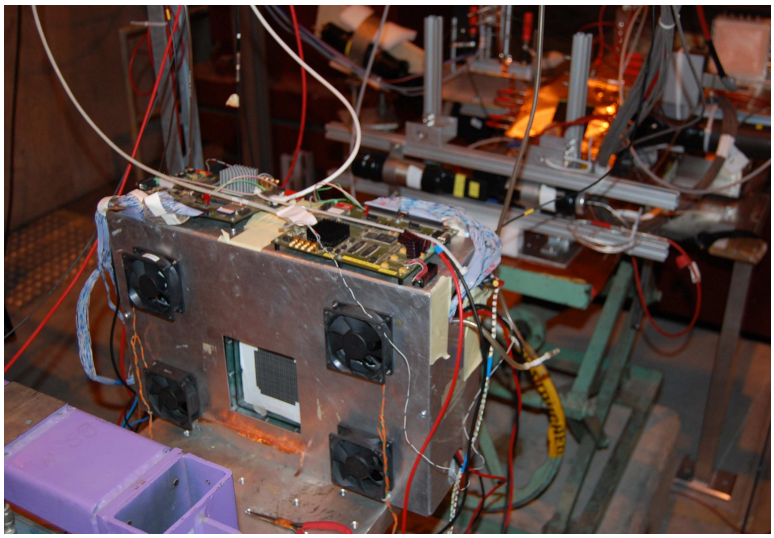

Figure 4.20. CERN-SPS beam test of the GEM.

in which tracks are guided into 4 groups each connected to one FEB using two 68-pin connectors affixed on the side of the chamber. Out of the four layers in the readout PCB, one was used exclusively for ground connections. One such chamber which is shown in Fig. 4.20, has been tested at the H4 beamline at CERN in October 2011. The triple GEM chamber tested at CERN had a conversion gap of 3 mm, gaps between each GEM foil-pair was 2 mm and the gap between the last GEM foil and the readout plane is 2 mm. Such a chamber coupled to the conventional electronics was tested earlier using radioactive sources and cosmic rays as reported in [90]. In the following section, we present the results obtained by the self-triggered readout system in CERN test beam. For all the measurements reported here, the High voltages for different channels were applied through a resistive chain and the gas mixture used was of Ar-CO_2 in the ratio of 70:30 in an atmospheric pressure [91].

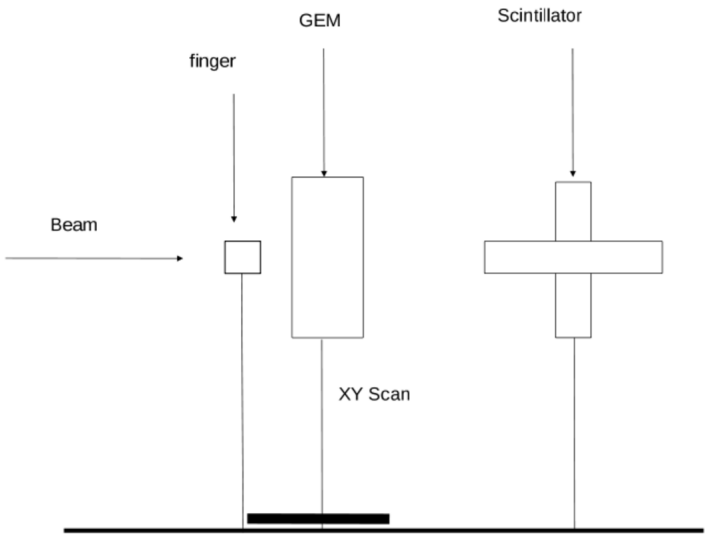

Figure 4.21. Schematic of CERN-SPS test beam set up.

4.8 Test beam experimental setup

The schematic layout of the test beam setup at CERN H4 line shown in Fig.4.21 is used to test the chamber with muon beams. Two downstream scintillators each of active area 10 cm × 10 cm in coincidence with an upstream 3 mm x 3 mm finger scintillator placed very close to the chamber formed the trigger. The nXYTER- based readout discussed earlier was used in the test run. Two ROC's were used to read four FEB's, each connected to 128 channels. The coincidence trigger signal was distributed to the ROC auxiliary channels to record the trigger time-stamps. The GEM-hit time stamps were recorded by the nXYTER and only the hits produced by beam particles are time-correlated with the trigger. We have varied the threshold on nXYTER at different runs, but for the results presented here, a threshold corresponding to 1 fC was applied.

4.9 Results

First step of analysing the data from such a self-triggered system is to obtain the distribution of intervals between the time-stamps of the GEM-hits and the coincidence trigger signal. Fig. 4.22 shows the time-difference distribution for a muon run when the

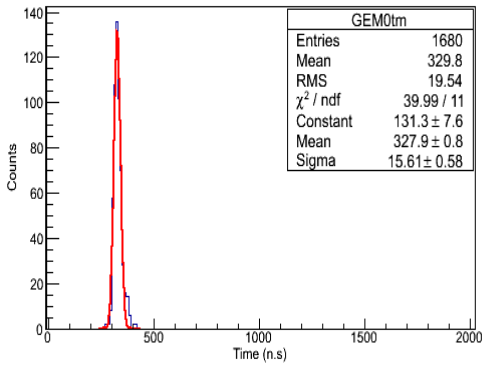

Figure 4.22. Distribution of the time difference between GEM hits and triggers.

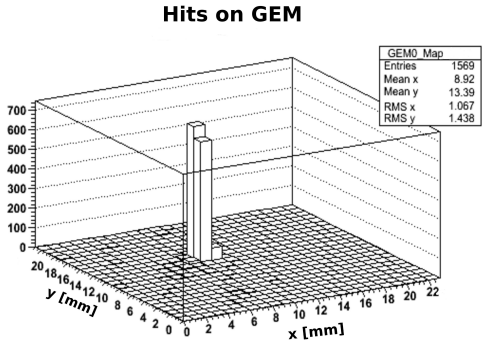

Figure 4.23. Typical beam spot of muon concentrated mainly in one pad.

chamber was operating at a total voltage V_{Total} of 2900 V corersponding to ΔV_{GEM} of 350 V. The distribution shows a well-defined Gaussian shape with a width of 17.9 ns. The width is related to the time resolution of the chamber which improves with the applied voltage reaching a saturation of 15 ns at Δ V_{GEM} of 360 V. It should be noted that the actual time resolution would be some what better after the subtraction of the time-jitter due to trigger scintillator. A complete absence of entries on both sides of the time-correlation peak shows that in the muon run the chamber had no significant uncorrelated noise. The GEM-hits within the time-correlation peaks are considered to be beam-related hits and the coordinates are plotted in Fig.4.23 to show the beamspot in a muon run. The spread of the spot depends both on the beam-spread and the GEM cluster-size. As the beam was defined mainly by the 3 mm $\times$ 3 mm finger scintillator, placed very close to the detector it therefore confines the beam mostly in one cell area of the chamber.

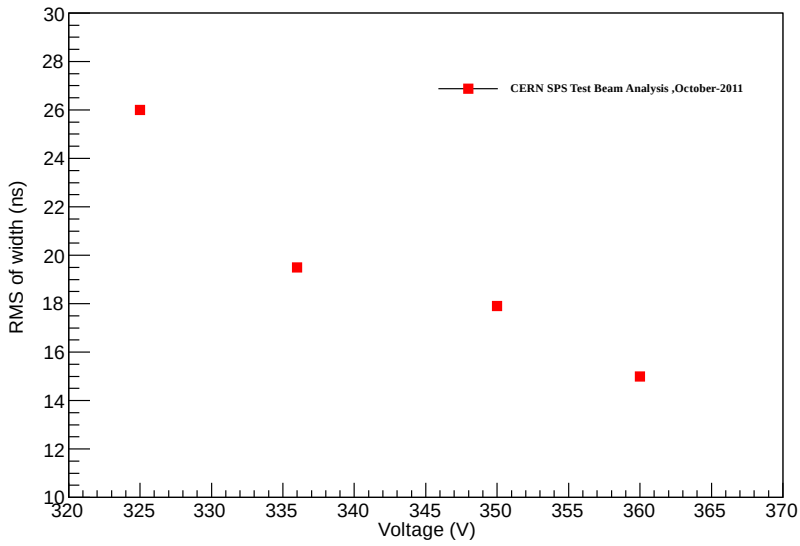

Figure 4.24. Variation of width of r.m.s of time-correlation with applied Voltage.

4.9.1 Efficiency

For the CBM-MUCH, attaining an efficiency $>$ 95 % is a prerequisite for effective detection of muons. Additionally, it is required that the efficiency remains stable over the operating range of HV, particle rate and other operating conditions. We have seen earlier that [90] an efficiency of 95 % is attained with cosmic rays using conventional electronics with a chamber of somewhat larger gap widths. In the test beam experiment reported here, the coincidence trigger signal is applied as an input to the auxiliary channel of ROC and the particles are taken to be detected if there is at least one hit in the time-correlation window corresponding to that trigger signal. The efficiency is therefore defined as,

$$Efficiency = \frac{N_{GEM}}{N_{trigger}} \tag{4.5}$$

where, N_{GEM} = Number of those events which are having at least one GEM hit in the time-correlation window and $N_{trigger}$ =Total number of trigger events. Fig.4.24 shows the variation of efficiency with ΔV_{GEM} for muon data. The efficiency reaches

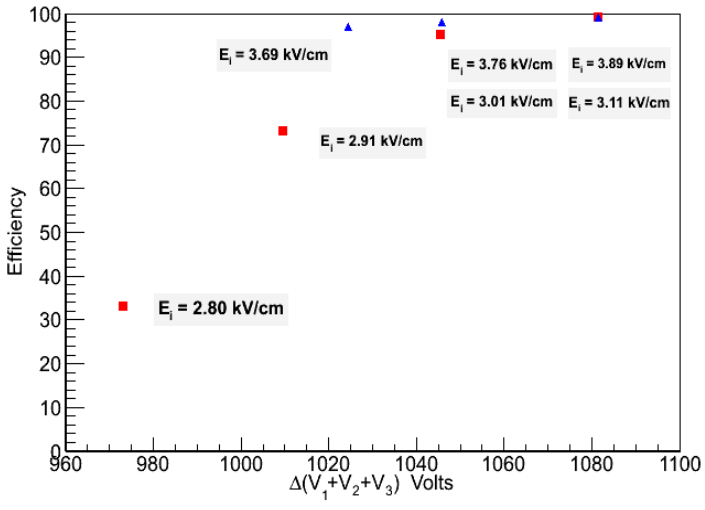

Figure 4.25. Variation of efficiency with applied Voltage.

Table 4.1. Values of induction voltage and their corresponding induction field (Blue points of the Figure 4.24.

Induction Voltage	Induction Field (E_i)	$\Delta V_{GEM}(V_1 = V_2 = V_3)$
V	kV/cm	V
545.76	3.69	336.552
565.32	3.76	348.61
584.64	3.89	360.65

Table 4.2. Values of induction voltage and their corresponding induction field (Red points of the Figure 4.24.

Induction Voltage	Induction Field (E_i)	$\Delta V_{GEM}(V_1 = V_2 = V_3)$
V	kV/cm	V
420.96	2.80	324.49
436.60	2.91	336.55
452.16	3.01	349.54
467.71	3.11	360.52

98 % at ΔV_{GEM} = 360V and then saturates. The efficiency depends on the Signal to Background ratio of the chamber and has dependence on the applied threshold on nXYTER. The gain estimated at ΔV_{GEM} of 360 V for a similar chamber is 4000 [90]. This therefore suggests a better signal to background ratio for muon runs. A detailed rate dependent study is the task of future beam tests. Reducing the threshold by 20 % does not change the saturation voltage appreciably.

4.9.2 Cell Multiplicity

As per literature, the GEM cluster size for comparable detector configuration is 600 μm [93]. For a cell-size of 3 mm $\times$ 3 mm, it is expected that for the beam particle incident at the middle of the cell, the cluster is expected to be confined inside one cell. At CBM the tracks reconstructed by STS will be projected on to the layers of MUCH and the hits lying within the field of interest will be taken as the track-hit. As CBM-MUCH is lying outside the magnetic field, so track parameters will not be updated after the inclusion of MUCH hits. The position resolution therefore does not play a crucial role unless the track overlap probability is significantly large resulting in track loss. For projecting tracks on GEM plane of CBM-MUCH, the cluster size which determines the position resolution is an important parameter and therefore requires detailed study. Fig. 4.25 shows the distribution of cell-multiplicity for a muon run. Fig.4.25 shows that the cell multiplicity for muon run increases slowly from 1.1 atΔV_{GEM} of 325 V to 1.4 at ΔV_{GEM} of 360V. With the increase in ΔV_{GEM} enhancement of gain results in a larger transverse size of the GEM profile which might be related to the increase in cell multiplicity with voltage.

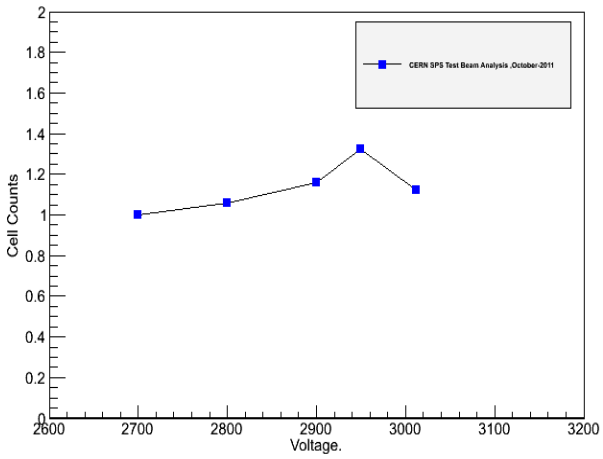

Figure 4.26. Variation of cell multiplicity with applied voltage.

4.10 Summary and Conclusions

Triple-GEM chamber because of its better reported spark-rate performance among others has been selected by several experiments for muon tracking. Such chambers are being developed at VECC and also very soon in BHU, Varanasi to be used as tracking devices in the muon detection system at the CBM experiment at FAIR. A prototype chamber made of 10 cm $\times$ 10 cm single-mask GEM foil with pad readout has been tested using muon beams at the H4 beamline at SPS-CERN. The detector has been readout by a self-triggered ASIC named nXYTER. In this self-triggered system, pad-hits produced by the beam particle are correlated in time with the trigger signal. The width of the time-correlation distribution decreases with applied voltage reaching a RMS of 15 ns at the operating voltage. The time resolution of the chamber demonstrates its capability in resolving hits of 10 MHz/cm^2 rate. The chamber operated with Ar-CO_2 gas mixture in 70:30 ratio gives $>$ 98 % efficiency for muons at ΔV_{GEM} = 360V. The cell-multiplicity for muon is 1.4. The cell multiplicity increases slowly with voltage sug-

gesting the increase of transverse profile of the GEM. The cell multiplicity close to one suggests that the position resolution for muon hits will be 860 μm as governed by the cell size only. In summary, we have tested a 10 cm $\times$ 10 cm triple GEM chamber with a self-triggered readout system. An efficiency 95 %, time resolution of 15 ns and cell multiplcity 1.4 satisfy the required criteria for CBM-MUCH chambers. Response of the detector to other set of parameters like rate handling capability, aging among others is a matter of further study.

Chapter 5

Particle Production in the CBM experiment

The main motivation of this chapter is to show what one should expect in context to particle multiplicities and particle ratios at CBM energies, in view of equilibrated statistical as well as transport models. Our main emphasis is on the hadron multiplicities and their ratios, the production of strange particles and asymmetry in the particle-antiparticle production as these are still unsettled issues pertaining to the QCD phase transition. At the end of this chapter, we summarize the results obtained from this study.

5.1 Introduction

Relativistic heavy ion collisions provide an unique way to create and investigate the QCD matter at extreme temperature (T) and/or density (ρ_B) [94, 95]. These experiments are expected to produce short lived bubbles of medium in which the quarks and gluons are the active degrees of freedom [96]. However the analysis of such collision events is complicated due to a transient nature of the reaction. In these reactions, the object of interest is the formation of a fireball which consists of a compressed and/or heated zone and it is of finite small size (order of few fermi) and further it fades away in a very short duration of less than 10^{-22} seconds [37]. The only observation comes through the particles (most abundantly hadrons) produced and emitted from the colli-

sion zone into the detectors. The main features of particle multiplicity i.e. the variation of number of particles produced with respect to collsion energy, the momentum spectra and the relative abundances of different species have led us in the understanding of the nature and properties of strong interactions [97]. Several experimental programmes were planned to explore the properties of strongly interacting matter and to search the possible existence of QGP. e.g. alternating gradient synchrotron (AGS) and relativistic heavy -ion collider (RHIC) experiment at BNL [98–100], super-proton-synchrotron (SPS) and large hadron collider (LHC) at CERN [101–103] etc. The compressed baryonic matter (CBM) experiment at Facility for antiproton and ion research (FAIR) machine will provide a similar hot, dense situation in the laboratory. The aim of the CBM experiment is to obtain vital information on (*i*) the properties of hadrons in dense or hot baryonic /hadronic matter, (*ii*) the restoration of chiral symmetry at high temperatures and high baryon densities, (*iii*) the deconfinement phase transistion from hadronic to quark -gluon matter at high temperatures and/or high baryon densities, and (iv) most importantly on the nuclear equation-of-state at high baryon densities [39, 104].

The experimental efforts always need reliable theoretical guidance to proceed in the right direction. Lattice QCD which is the first principle method to calculate the properties of QCD matter provides some quality information on the strongly interacting matter at finite temperature and zero (or very small) chemical potential (μ) [105, 106]. However, lattice QCD approach is severely limited at finite chemical potential due to a notorious sign problem. Perturbative calculations are only useful at very high temperatures as the QCD coupling constant becomes small. In recent years, Relativistic fluid dynamics and statistical mechanics emerged as two important theoretical tools to explore the properties of hot and dense QCD matter ceated in the heavy ion collision experiments. Standard statistical models or thermal models assume a system in global thermodynamical equilibrium. It means that the intensive variables like pressure (P), temperature (T), and chemical potential (μ) are constant throughout the volume of the system. The most popular thermal model is ideal hadron gas (IHG) model and its

modified versions are known as excluded volume models. These models assume that the hadrons are produced according to their statistical weights from an equilibrated hadron gas at freeze-out. These models were used in the recent past in order to deduce the multiplicities and ratios of hadrons and agreements with the experimental data were found to be excellent [107–110]. On the other hand, hydrodyanmical or transport models assumes that the system created at an initial time is in local thermodynamic equilibrium [111, 112]. It means that the thermodynamical variables such as pressure, temperature of the system vary with space-time point. However, the variation is so slow that for any point, one can assume thermodynamic equilibrium in some neighbourhood about that point. After this initial time, the system expands and cools-off until the hadronic freeze-out occurs and produces the hadrons. These models again show good agreement with the data obtained from RHIC and LHC [112].

In this chapter, our main motivation is to show what one should expect in context to particle multiplicities and particle ratios at CBM energies, in view of equilibrated statistical as well as transport models. We further compare the model results with the available experimental data of AGS and SPS energies. In the section 5.2, we will provide a brief description of a recently developed thermal model with excluded volume correction. Further Section 5.3 will provide the results regarding the hadron multiplicities and their ratios and comparison among various models. We mainly emphasize on the net baryon density created at freezeout, the production of strange particles and the asymmetry in the particle-antiparticle production etc. because these isuues are still unsettled in order to get information on the QCD phase transition. The last section will be devoted to the conclusion and future prospects drawn from this study.

5.2 EOS for a Hot and/or Dense Hadron Gas

Recently we have proposed a thermodynamically consistent excluded volume model for the hot and dense hadron gas (HG). In this model, the grand canonical partition function

for the HG with full quantum statistics and after suitably incorporating excluded volume correction is [113–117]:

$$lnZ_i^{ex} = \frac{g_i}{6\pi^2 T}\int_{V_i^0}^{V-\sum_j N_j V_j^0} dV \int_0^\infty \frac{k^4 dk}{\sqrt{k^2+m_i^2}} \frac{1}{[exp\left(\frac{E_i-\mu_i}{T}\right)+1]} \tag{5.1}$$

where g_i is the degeneracy factor of ith species of baryons,E_i is the energy of the particle ($E_i = \sqrt{k^2+m_i^2}$), V_i^0 is the eigenvolume of one baryon of ith species and $\sum_j N_j V_j^0$ is the total occupied volume and N_j represents total number of baryons of jth species.

Now we can write Eq.(5.1) as:

$$lnZ_i^{ex} = V(1-\sum_j n_j^{ex} V_j^0) I_i \lambda_i, \tag{5.2}$$

where I_i represents the integral:

$$I_i = \frac{g_i}{6\pi^2 T}\int_0^\infty \frac{k^4 dk}{\sqrt{k^2+m_i^2}} \frac{1}{\left[exp(\frac{E_i}{T})+\lambda_i\right]}, \tag{5.3}$$

and $\lambda_i = exp(\frac{\mu_i}{T})$ is the fugacity of the particle, n_j^{ex} is the number density of jth type of baryons after excluded volume correction and can be obtained from Eq.(5.2) as:

$$n_i^{ex} = \frac{\lambda_i}{V}\left(\frac{\partial lnZ_i^{ex}}{\partial \lambda_i}\right)_{T,V} \tag{5.4}$$

This leads to a transcendental equation :

$$n_i^{ex} = (1-R) I_i \lambda_i - I_i \lambda_i^2 \frac{\partial R}{\partial \lambda_i} + \lambda_i^2 (1-R) I_i^{'} \tag{5.5}$$

where $I_i^{'}$ is the partial derivative of I_i with respect to λ_i and $R = \sum_i n_i^{ex} V_i^0$ is the

fractional occupied volume depending on n_i^{ex}. We can write R in an operator equation as follows [113]:

$$R = R_1 + \hat{\Omega} R \tag{5.6}$$

where $R_1 = \frac{R^0}{1+R^0}$ with $R^0 = \sum n_i^0 V_i^0 + \sum I_i' V_i^0 \lambda_i^2$; n_i^0 is the density of pointlike baryons of ith species and the operator $\hat{\Omega}$ has the form :

$$\hat{\Omega} = -\frac{1}{1+R^0} \sum_i n_i^0 V_i^0 \lambda_i \frac{\partial}{\partial \lambda_i} \tag{5.7}$$

Using Neumann iteration method and retaining the series upto $\hat{\Omega}^2$ term, we get

$$R = R_1 + \hat{\Omega} R_1 + \hat{\Omega}^2 R_1 \tag{5.8}$$

Eq.(5.8) can be solved numerically. Finally, we get the total pressure [113, 114] of the hadron gas as:

$$p_{HG}^{ex} = T(1-R) \sum_i I_i \lambda_i + \sum_i P_i^{meson} \tag{5.9}$$

In Eq. (5.9), the first term represents the pressure due to all types of baryons where excluded volume correction is incorporated and the second term gives the total pressure due to all mesons in HG having a point like size. This makes it clear that we consider the hard-core repulsion arising between two baryons only. Essentially we consider that the mesons can interpenetrate each other but baryons can not owing to their hard-core size. In this calculation, we have taken an equal volume $V^0 = \frac{4\pi r^3}{3}$ for each type of baryon with a hard-core radius $r = 0.8$ fm. We have taken all baryons and mesons and their resonances having masses upto $2GeV/c^2$ in our calculation for the HG pressure. We have also imposed the condition of strangeness conservation by putting $\sum_i S_i(n_i^s - \bar{n}_i^s) = 0$, where S_i is the strangeness quantum number of the ith hadron, and $n_i^s(\bar{n}_i^s)$ is the strange (anti-strange) hadron density, respectively. Using this constraint equation, we get the value of strange chemical potential in terms of μ_B.

In relativistic heavy ion collisions, a hot, dense matter is formed and it is often referred as a "fireball". The physical variables of the fireball are the volume V, energy density ϵ and baryon density ρ_B, which are in fact related to T and μ_B of the fireball. When cooling or expansion of the fireball starts, it goes through two types of freeze-out stages, namely chemical freeze-out and thermal freeze-out. When inelastic collisions between constituents of the fireball cease we call this the chemical freeze-out stage. Later when elastic collisions are also stopped, this is called the thermal freeze-out. In our model we suppose that at the time of chemical freeze-out all the hadrons are emitted from the entire freeze-out hypersurface. Now the main point is to correlate thermodynamical variables T and μ_B of the fireabll to the experimental variable $\sqrt{s_{NN}}$. In our model we vary the T and μ_B of our model and observe how the experimental data of particle ratio are fitted at a given $\sqrt{s_{NN}}$. Similarly we repeat the exercise for all the data availaible ranging from SIS to RHIC energy and thus get a set of T and μ_B for a particular $\sqrt{s_{NN}}$. Now after such fitting procedure we get a parametrization between $\sqrt{s_{NN}}$ and μ_B or T as follows :

$$\mu_B = \frac{a}{1 + b\sqrt{s_{NN}}}, \tag{5.10}$$

$$T = c - d\mu_B^2 - e\mu_B^4. \tag{5.11}$$

where the parameters a, b, c, d, and e have been determined from the best fit: $a = 1.482 \pm 0.003$ GeV, $b = 0.351 \pm 0.009$ GeV^{-1}, $c = 0.163 \pm 0.002$ GeV, $d = 0.170 \pm 0.020$ GeV^{-1} , $e = 0.015 \pm 0.010$ GeV^{-3}. The details of the fitting procedure in thermal models can be found in Ref [107]. S.K. Tiwari et al. have done this fitting for various other hadron gas models in order to obtain the values of T and μ_B with respect to $\sqrt{s_{NN}}$ and all this is shown in Table I of Ref. [113]

5.3 Results and Discussion

The extracted freeze-out temperature in statistical thermal models of HG generally increases monotonically with the collision energy. However, the corresponding net baryon density exhibits a more complicated behaviour [118]. Fig.5.1 demonstrates the variation of ρ_B with $\sqrt{s_{NN}}$. To calculate ρ_B, we first use our parametrization given by Eqs. (5.10) and (5.11) to get the values of μ_B and T for given $\sqrt{s_{NN}}$. At this T and μ_B, we have calculated the value of net baryon density ρ_B. In the present excluded volume model, the net baryon density increases with $\sqrt{s_{NN}}$ (see Fig.5.1), reaches a maximum value near $\sqrt{s_{NN}} = 8 - 9$ GeV and then starts decreasing. The maximum freeze-out net baryon density is approximately half of the normal nuclear density $\rho_0 = 0.15$ fm^{-3}. We have compared our model results with the net baryon density obtained by Begun et al. [119] using excluded volume model based on Ref. [120]. They have calculated the baryon density at various $\sqrt{s_{NN}}$ using 0.5 fm as hard core radius (r_b) for each baryon and all the mesons are treated as point like particles ie.($r_m = 0$). On the other hand, we have taken the value of 0.8 fm as the hard-core radius for each baryon in calculating the excluded volume. The quantitative values of maximum freezeout density achieved in heavy ion collions are almost equal in both the models. However, the position of the maximum in the net baryon density is somewhat shifted towards the lower energy side in the results obtained by Begun et al. [119]. The maximum value of ρ_B obtained in our model as well as in the excluded volume model of Begun et al. is also lower than the value obtained in Ref. [118] where a HRG model is used without any excluded volume correction. Obviously the excluded volume effect shifts the net baryon density achieved at freezeout towards the lower value.

Fig.5.2 presents the variation of total multiplicity of π^+ with respect to $\sqrt{s_{NN}}$. In the CBM energy range, the fireball volume at freeze-out, extracted in the excluded volume model approach appears almost constant [121] for all emitted particles. We have taken a logistic value of 5000 fm^3 as the fireball volume in order to calculate

the total multiplicity of hadrons. We compare our results with the experimental data obtained at AGS and SPS [28, 122–126] at low energies. We have also shown the total multiplicity of π^+ obtained from transport models like HSD and UrQMD. Both HSD [127] and UrQMD [55, 128] models usually employ the concepts of string, quark, diquark, (q, $\bar{q}$, qq, $\bar{q}\bar{q}$) as well as the hadronic degrees of freedom. However, the numerical evaluations are quite different in HSD as compared to UrQMD. The UrQMD includes all baryonic resonances upto an invariant mass of 2 GeV as well as mesonic resonances upto 1.9 GeV [55, 128]. However, HSD incorporates only the baryon octet and decuplet states and N^* (1440), N^* (1535) as well as their antiparticles together with the 0^- and 1^- meson octets. Higher baryonic resonances are discarded as the resonance structure (above Δ peak) is not clearly seen experimentally even in the photo-absorption by light nuclei [129–131]. In contrast to the UrQMD at low energy baryon-baryon and meson-baryon collisions, HSD includes the direct (nonresonant) meson production.Our excluded volume model suitably describes the data upto 5 GeV. However, all three models yield larger multiplicity for π^+ relative to the data above 5 GeV. Although we notice that, the multiplicity of the produced π^+ in excluded volume model is closer to the data in comparison to other two models. In principle, the yield of each particle is mainly governed by the particle fugacity essentially determined from the chemical freeze-out parameters. It also depends on the size of the system (or volume V) in which some variations can always appear.

Fig.5.3 demonstrates the variation of K^+ multiplicity with respect to $\sqrt{s_{NN}}$. We have used the same freezeout volume ie., 5000 fm^3 as used in the π^+ multiplicity. We compare our model results with the results obtained from HSD and UrQMD simulations. We have also shown the experimental data from CERN-SPS and RHIC-AGS for comparison [28, 122–126]. The results obtained from both HSD and UrQMD do not match with the data beyond the energy 5 GeV. The overall level of agreement with the excluded volume model results is quite good. However, HSD results also suitably describe the data below 5 GeV. It should be emphasized here that the thermal statistical

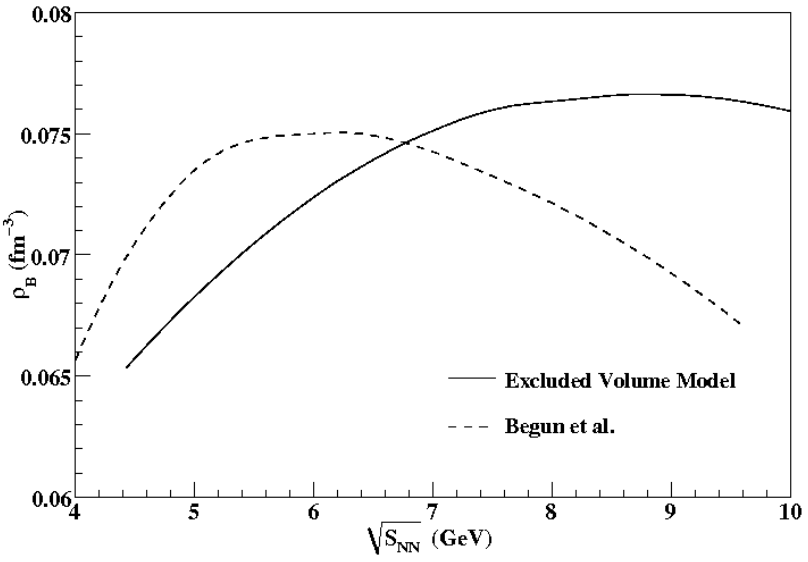

Figure 5.1. Variation of net-baryon density (ρ_B) at freezeout with respect to center of mass energy ($\sqrt{s_{NN}}$).

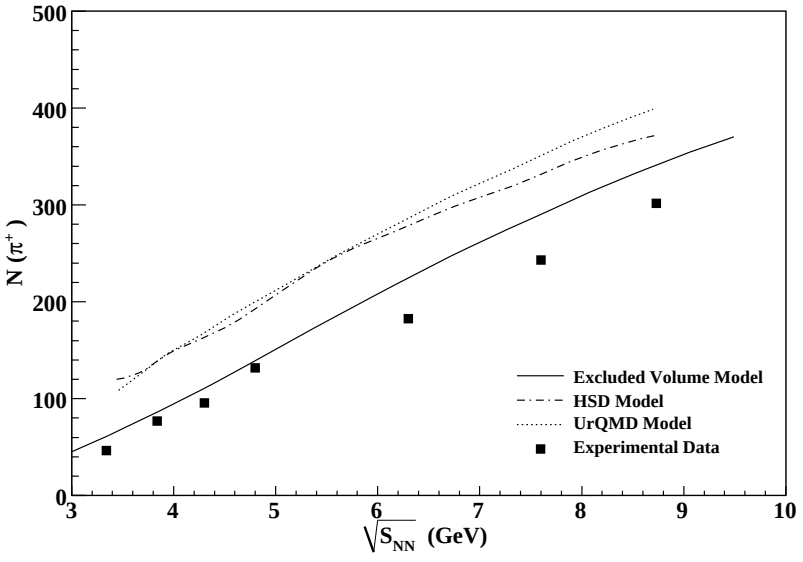

Figure 5.2. Variation of total multiplicity of produced π^+ with respect to $\sqrt{s_{NN}}$. Dash-dotted and dotted curve is the results obtained from HSD and UrQMD model, respectively [127]. Experimental data is taken from Ref. [28, 122–126].

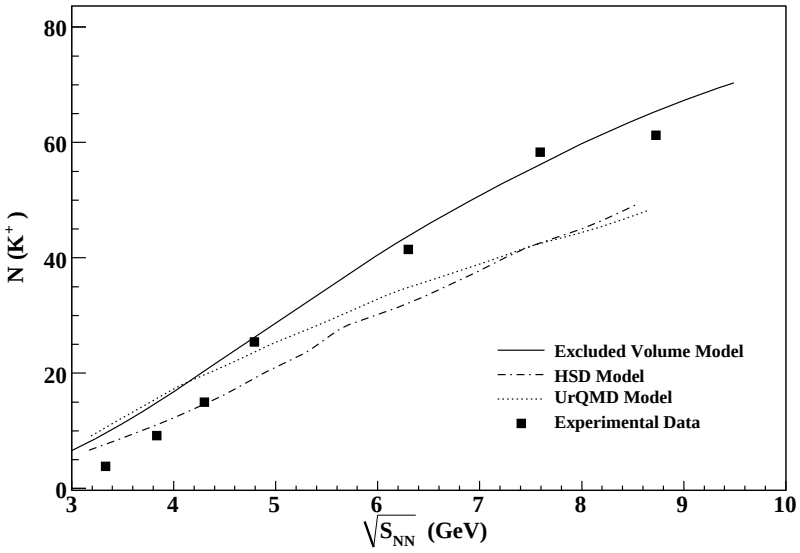

Figure 5.3. Variation of total multiplicity of produced K^+ with respect to $\sqrt{s_{NN}}$. Dash-dotted and dotted curve is the results obtained from HSD and UrQMD model, respectively [127]. Experimental data is taken from Ref. [28, 122–126].

model should be used with caution at lower energies since number of produced particles is very small.

In Fig.5.4, we present the variation of total multiplicity of K^- with $\sqrt{s_{NN}}$. The results obtained from our model is in excellent agreement with the data [28, 122–126]. However, HSD and UrQMD results satisfy the experimental data only below 5 GeV. Above 5 GeV, the total multiplicity of K^- obtained from HSD and UrQMD are relatively small and does not agree with the data.

Strangeness enhancement has been proposed as one of the early and important signals of QGP formation [26, 132–135]. It has been argued that if a quark gluon plasma is formed from compressed nuclear matter as may happen in the nuclear fragmentation region and/or in the low energy "stopping regime", then the abundance of s and $\bar{s}$ quark would be highly enhanced compared to that of light u or d quark [26, 132, 136, 137]. This is possibly due to the Pauli exclusion principle which strongly suppresses the

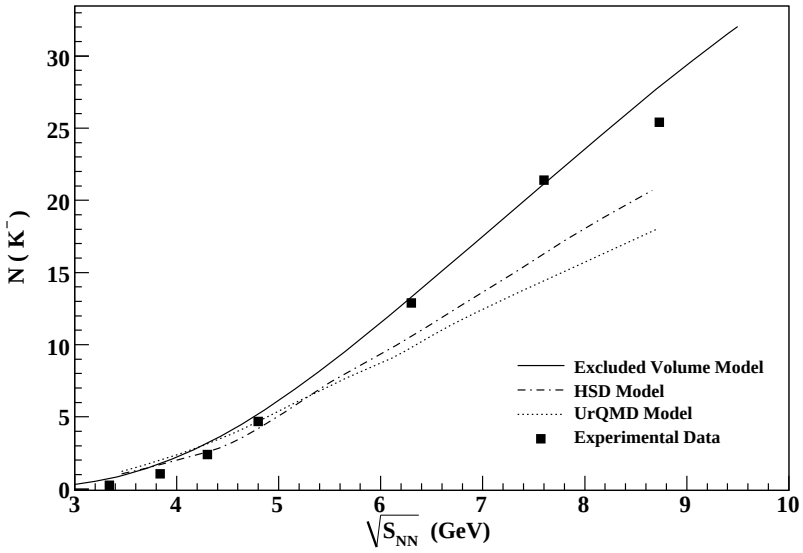

Figure 5.4. Variation of total multiplicity of produced K^- with respect to $\sqrt{s_{NN}}$. Dash-dotted and dotted curve is the results obtained from HSD and UrQMD model, respectively [127]. Experimental data is taken from Ref. [28, 122–126].

further creation of light-quark pairs [138] in the medium having abundant u, d quarks. This asymmetry in the flavour composition generated by a baryon-rich QGP should result in a large production of K^+, K^-, Λ, $\bar{\Lambda}$ etc [139]. This effect is even more evident in the case of the multistrange hyperons. A striking observation reported by NA49 collaboration is a pronounced and sharp maximum in the excitation function of K^+/π^+ ratio at 30 AGeV [122]. This sharp maximum which is also known as "horn", is not seen in p+p collisions. As K^+ is by far most abundant carrier of anti-strangeness at SPS energies, it also provides a good measure of the total strangeness produced in the collision. The ratio K^+/π^+ represents the strangeness to entropy ratio. A sharp maximum in this quantity was predicted by the statistical model indicating the early stage as a consequence of the transition to a deconfined state [139]. A similar maximum at the same beam energy is also reported by the same collaboration for other strange particles like Λ's and Ξ^- [123]. These observations confirm that this particular feature is not given by K^+ alone, but represent the total strangeness content of the

final state [140]. The measurement of the excitation function of strangeness production by NA49 collaboration have renewed a fresh stimulating discussion about the role of strangeness as a signature for the deconfinement phase transistion.

Fig.5.5 demonstrates the variation of K^+/π^+ ratio with respect to $\sqrt{s_{NN}}$. We have compared our model results with the experimental data obtained from SPS experiment [28, 122–126]. We have further compared them with the other results like HSD, UrQMD and Boltzmann-Uehling-Uhlenbeck (BUU) transport [141] models. We find that both the HSD as well as UrQMD model fail to give agreement with the experimental data. However, BUU model shows better results in comparison to HSD and UrQMD. Our model yields better results in agreement with the experimental data. The authors in Ref. [127] have suggested that the overestimation of π^+ multiplicity in thermal models give theoretical curve lying below the experimental data. The similar fireball volume used for K^+ and π^+ in the excluded volume model can also contribute for such disagreement. Here we use the same freeze-out volume for the emission of all kinds of hadrons from the fire-ball surface. CBM experiment will definitely provide an important insight in the understanding of strange particle production mechanism and more vitally address the mechanism for the existence of the "horn" like behaviour in the lower energy region.

In Fig.5.6, we present the variation of K^-/π^- with respect to $\sqrt{s_{NN}}$. Our model suitably describes the data but below 5 GeV, we again notice a large disagreement. However, HSD and UrQMD both also give complete disagreement with the experimental data almost in the entire energy range ie., from 3 to 9 GeV.

In heavy-ion collisions, a large production of anti-baryons with respect to baryons are also considered as the signal for the formation of deconfined QGP [142, 143]. In heavy ion collisions, the system has a non-zero baryon number density arising due to nuclear stopping. At small and moderate center-of-mass energies as existing in the case of CBM experiment, the nuclear stopping is large in comparison to the RHIC and/or

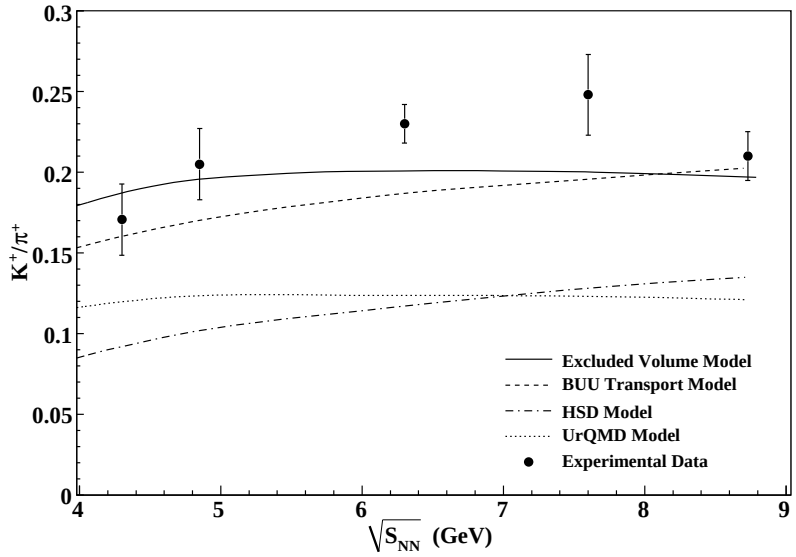

Figure 5.5. Variation of K^+/π^+ ratio with respect to $\sqrt{s_{NN}}$. The results obtained from HSD and UrQMD are taken from Ref. [127]. The results obtained from BUU transport model is extracted from Ref. [141]. Experimental data is taken from Ref. [28, 122–126].

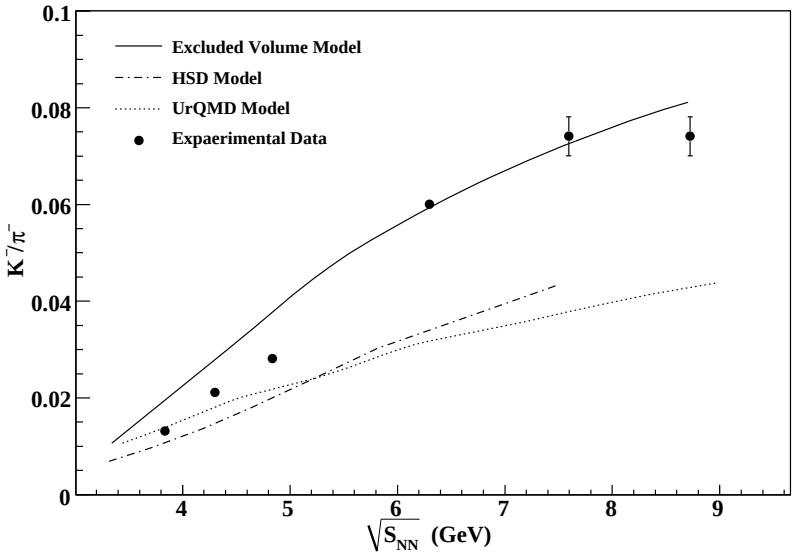

Figure 5.6. Variation of K^-/π^- ratio with respect to $\sqrt{s_{NN}}$. The results obtained from HSD and UrQMD are taken from Ref. [127]. Experimental data is taken from Ref. [28, 122–126].

LHC energies where nuclear transparency is found to dominate. Nuclear stopping leads to an asymmetry between the production of hadrons and antihadrons in the produced particles other than the initial finite baryon number. However, there is a possibility that hadronization can also generate additional particle-antiparticle asymmetry. This asymmetry can be measured by the ratio of yields of antihadrons to hadrons [144, 145]. Ratios of yield of antiprotons to protons ($\bar{p}/p$) and that of antikaons to kaons (K^-/K^+) are the representatives of two such significant observables measuring the hadron-antihadron asymmetry in heavy ion collisions [144, 145]. The ratio $\bar{p}/p$ carries the information regarding baryon-antibaryon asymmetry and the ratio K^-/K^+ almost cancels the effect of strangeness production and indicates the asymmetry between charged mesons and their antiparticles generated in the hot, dense medium.

In Fig.5.7 and Fig.5.8, we have shown the variations of $\bar{p}/p$ and K^-/K^+ with $\sqrt{s_{NN}}$, respectively as obtained in our excluded volume model with the center of mass energy. In both the cases, the production of antiparticle to particle is less at lowest CBM energy. However, the asymmetry in $\bar{p}$ and p production is larger as also observed between K^- and K^+. As the energy increases the production of antiparticle over particle increases since there is an increase in nuclear transparency. However, it is important to state here that excluded volume model does not agree with the experimental data for the net nucleon density at RHIC highest energy [113] also.

5.4 Summary and Conclusions

In summary, we have calculated the net baryon density at freeze-out in the CBM energy range in near future will be the maximum achievable density in heavy ion collisions. Further, we have calculated the total multiplicities of various produced hadrons e.g. π^+, K^+, K^- using a constant freeze-out volume equal to 5000 fm^3 for all the hadrons. We have also calculated the ratio of K^+/π^+ and K^-/π^- in CBM energy range. Almost all the models fail to reproduce the "horn" in K^+/π^+ ratio. Furthermore, we have also

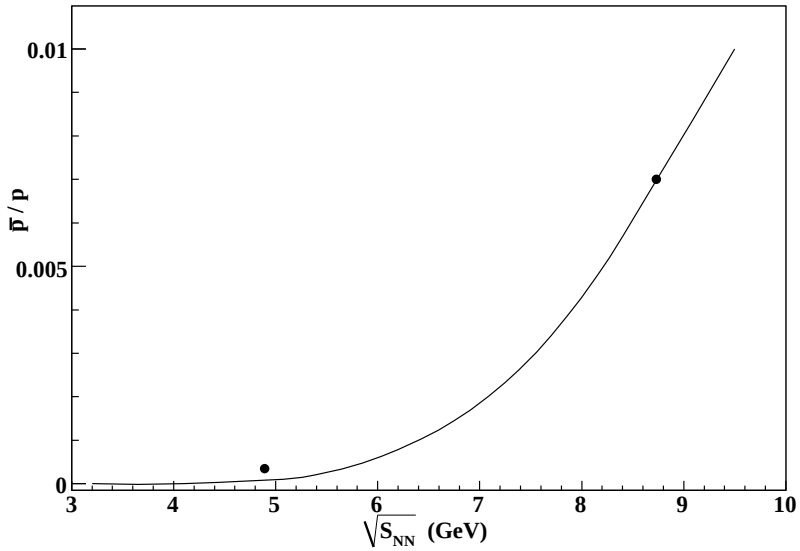

Figure 5.7. Variation of $\bar{p}/p$ with respect to $\sqrt{s_{NN}}$. Experimental data is taken from Ref. [28, 122–126].

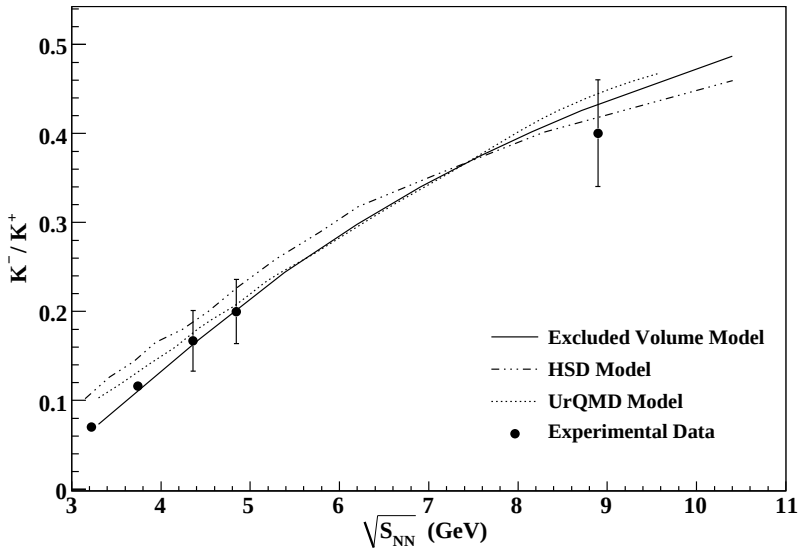

Figure 5.8. Variation of K^-/K^+ with respect to $\sqrt{s_{NN}}$. The results obtained from HSD and UrQMD are taken from Ref. [127]. Experimental data is taken from Ref. [28, 122–126].

calculated the particle to antiparticle ratio like $\bar{p}/p$ and K^-/K^+. In CBM energy range these ratios increase rapidly. However, due to lack of experimental data, we do not have any meaningful comparison and hence we cannot precisely understand the asymmetry between hadron and anti-hadron production in heavy ion collisions.

In conclusion, we face many worthwhile questions regarding particle production at CBM energy regime. More vital questions are regarding the formation of a thermal fireball and the applicability of thermal equilibrium in the statistical system. But it is intersting to investigate what we should precisely expect. So we should precisely know what we expect from various equlibrium-nonequilibrium models.

We conclude that our excluded volume model gives a better agreement with the available experimental data in comparison to other models. In the CBM energy range most of the multiplicities as well as particle ratios show somewhat peculiar behaviour. However, there is scarcity of experimental data. The data available suffer from poor statistics also. The upcoming CBM experiment having a high luminosity beam will provide a unique opportunity to perform systematic and comprehensive measurements, with better statistics, of bulk and rare particle behaviour. This will help us to understand the particle production mechanism and also possibly find the existence of QGP at CBM energy.

Chapter 6

Summary and Conclusions

The CBM collaboration at FAIR, Germany will systematically measure both dielectrons and dimuons in p+p, p+A and A+A collisions as function of beam energy and size of the collision system. The dielectron and dimuon high-precision data will complement each other, and will provide a complete picture on dilepton radiation off dense baryonic matter. Therefore, the CBM experiment has a large discovery potential both at SIS 100 and SIS 300.

Di-muon measurement is at the core of the CBM physics program. We have done a systematic study pertaining to the geometry and pad sizes of the muon chamber. Designs are mostly defined by requirements of Low Mass Vector Meson (LMVM) measurements. Charmonium measurements (with additional 1 m iron absorber) are less sensitive to the configuration details. Simulations of both lowest (minimum boost) and highest energy (maximum multiplicity) are performed. Even at the lowest energy there seems to be no inexpensive version capable for measurements of low mass vector mesons (LMVM). Segmentation with minimum pad dimension 4 mm $\times$ 4 mm is a suitable choice, given the fact that pads of this size are relatively easy to fabricate.

A detector based on micro-pattern technology, namely GEM's, has been proposed for the first few stations of MUCH in CBM, where the particle density is very high. Triple-GEM chamber because of its better reported spark-rate performance among others has been selected by several experiments for muon tracking. Such chambers are being developed at VECC and very soon at BHU, Varanasi, to be used as tracking devices in the muon detection system at the CBM experiment at FAIR. A prototype chamber

made of 10 cm $\times$ 10 cm single-mask GEM foil with pad readout has been tested using muon beams at the H4 beamline at SPS-CERN. The detector has been readout by a self-triggered ASIC named nXYTER. In this self-triggered system, pad-hits produced by the beam particle are correlated in time with the trigger signal. The width of the time-correlation distribution decreases with applied voltage reaching a RMS of 15 ns at the operating voltage. The time resolution of the chamber demonstrates its capability in resolving hits of 10 MHz/cm^2 rate. The chamber operated with Ar-CO_2 gas mixture in 70:30 ratio gives > 98 % efficiency for muons at $\Delta V_{GEM} = 360$V. The cell-multiplicity for muon is 1.4. The cell multiplicity increases slowly with voltage suggesting the increase of transverse profile of the GEM. The cell multiplicity close to one suggests that the position resolution for muon hits will be 860 micron as governed by the cell size only. In summary, we have tested a 10 cm x 10 cm triple GEM chamber with a self-triggered readout system. An efficiency > 95 %, time resolution of 15 ns and cell multiplicity 1.4 satisfy the required criteria for CBM-MUCH chambers. Response of the detector to other set of parameters like rate handling capability, aging among others is a matter of further study.

We have also calculated the net baryon density at freeze-out in the CBM energy range which comes out to be the maximum achievable density in heavy ion collisions. Further, we have calculated the total multiplicities of various produced hadrons e.g. π^+, K^+, K^- using a constant freeze-out volume which is equal to 5000 fm^3 for all the hadrons. We have also calculated the ratio of K^+/π^+ and K^-/π^- in CBM energy range. Almost all the models fail to reproduce the "horn" in K^+/π^+ ratio. Furthermore, we have also calculated the particle to antiparticle ratio like $\bar{p}/p$ and K^-/K^+. In CBM energy range these ratios increases rapidly. However, due to lack of experimental data, we do not have any meaningful comparison and hence we cannot precisely understand the asymmetry between hadron and anti-hadron production in heavy ion collisions.

We face many worthwhile questions regarding particle production at CBM energy regime. More vital questions are regarding the formation of a thermal fireball and

the applicability of thermal equilibrium in the statistical system. But it is interesting to investigate what we should precisely expect. We should distinguish between various equilibrium-non equilibrium models. We conclude that our excluded volume model gives a better agreement with the available experimental data in comparison to other models. In the CBM energy range most of the multiplicities as well as particle ratios show somewhat peculiar behaviour. However, there is scarcity of experimental data. The data available suffer from poor statistics also. The upcoming CBM experiment having a high luminosity beam will provide a unique opportunity to perform systematic and comprehensive measurements, with better statistics, of bulk and rare particle behaviour. This will help us to understand the particle production mechanism and also possibly find the existence of QGP at CBM energy.

Bibliography

[1] J. Adams et al., [STAR Collaboration], *Nucl. Phys.* **A 757**, 102-183 (2005).

[2] D. J. Gross and F. Wilczek, *Phys. Rev. Lett.* **30** 1343,(1973).

[3] H. D. Politzer, *Phys. Rev. Lett.* **30**, 1346 (1973).

[4] K. Fukushima and T. Hatsuda, *Rept. Prog. Phys.* **74**, 014001 (2011) [arXiv:1005.4814 [hep-ph]].

[5] Z. Fodor and S. D. Katz, *JHEP* **04**, 050 (2004).

[6] O. Philipsen, *Prog. Theor. Phys. Suppl.* **174**, 206 (2008).

[7] M. G. Alford, *Ann. Rev. Nucl. Part. Sci.* **51**, 131 (2001).

[8] B. C. Barrois, *Nucl. Phys.* **B 129**, 390 (1977)

[9] M. Coleman Miller, arXiv:1312.0029v1 [astro-ph.HE], 1-51 (2013).

[10] M. G. Alford, A. Schmitt, K. Rajagopal et al., *Rev. Mod. Phys.***80**, 1455 (2008).

[11] H. Stocker and C. Sturm, *Rom. Journ. Phys.* **vol 58 Nos. 9-10**, 1023-1030 (2013).

[12] J. Letessier and J. Rafelski, Hadrons and Quark-Gluon Plasma ,*Cambridge University Press*, 2002.

[13] W. Ehehalt and W. Cassing, *Nucl. Phys.* **A 602**, 449 (1996)

[14] D.N. Schramm, B. Fields and D. Thomas, *Nucl. Phys.* **A 544**, 267c (1992).

[15] G.D. Westfall et al., *Nuclear Instruments and Methods* **238**, 347 (1985).

[16] H. H. Gutbrod, A. M. Poskanzer and H. G. Ritter, *Rep. Prog. Phys.* **52**, 1267-1328 (1989).

[17] R. Rapp and J. Wambach, Chiral Symmetry Restoration and Dileptons in Relativistic Heavy-Ion Collisions, arXiv:hep-ph/9909229v1 (1999).

[18] V. Friese, *Mathematical Modeling and Computational Science Lecture Notes in Computer Science* **7125**, 17-27 (2012).

[19] M. Stephanov, K. Rajagopal, E. Shuryak, *Phys. Rev. Lett.* **81**, 4816 (1998)

[20] G. Agakishiev et al., (HADES Collaboration), *Phys. Lett.* **B 663**, 43 (2008).

[21] G. Agakishiev et al., (HADES Collaboration), *Phys.Lett.* **B 690**, 118 (2010).

[22] G. Agakishiev et al., (HADES Collaboration), *Phys. Rev.* **C 84**, 014902 (2011).

[23] T. Matsui and H. Satz, *Phys. Lett.* **B 178**, 416 (1986).

[24] M. Abreu et al., *Phys. Lett.* **B 477** (2000) 28.

[25] F. Klingl et al., *Phys. Rev. Lett.* **82**, 3396 (1999).

[26] J. Rafelski and B. Muller, *Phys. Rev. Lett.* **48**, 1066 (1982).

[27] G.E. Bruno et al., *J. Phys. G: Nucl. Part. Phys.* **30**, 717c (2004).

[28] M. Gazdzicki et al., *J. Phys. G: Nucl. Part. Phys.* **30**, 701c (2004).

[29] C. Pinkenburg et al., (E895 Collaboration), *Phys. Rev. Lett.* **83**, 1295 (1999).

[30] P. Danielewicz etal., *Phys. Rev. Lett.* **81**, 2438 (1998).

[31] G. Stoicea et al., (FOPI Collaboration) *Phys. Rev. Lett.* **92**, 072303 (2004).

[32] W. Reisdorf et al., (FOPI Collaboration), *Nucl. Phys.* **A 876**, 1 (2012).

[33] C. Sturm et al., (KaoS Collaboration), *Phys. Rev. Lett.* **86**, 39 (2001).

[34] C. Fuchs et al., *Phys. Rev. Lett.* **86**, 1974 (2001).

[35] F. Uhlig et al., (KaoS Collaboration), *Phys. Rev. Lett.* **95**, 012301 (2005).

[36] P. Chung et al., (E895 Collaboration), *Phys. Rev. Lett.* **85**, 940 (2000).

[37] B. Friman et al., (Eds.), The CBM Physics Book, Lect. Notes Phys. 814, Springer-Verlag Berlin Heidelberg 2011 .

[38] *FAIR Baseline Technical Report*, http://www.gsi.de/documents/DOC-2006-Dec-94-1.pdf, 2006.

[39] P. Senger, *Centr. Eur. J. Phys.* **10 (6)**, 1289-1294 (2012).

[40] J. M. Heuser. [CBM Collaboration] *Nucl. Phys.* **A 830**, 563c-566c (2009).

[41] C. Hohne. *Int. J. Mod. Phys.* **E16**, 2419 (2007).

[42] M. Deveaux et al. *Nucl. Instrum. Meth.* **A 718**, 305-306 (2013).

[43] J. M. Heuser, *Nucl. Instrum. Meth.* **A 582**, 910 (2007).

[44] J. M. Heuser et.al., *Technical Design Report for the CBM, Silicon Tracking System*, GSI Report **2013-4**, ISSN **0171-4546**, 1-161 (2013).

[45] C. Hohne et al., *Nucl. Instrum. Meth.* **A 595**, 187 (2008).

[46] M. Petris et al., *Nucl. Instrum. Meth.* **A 732**, 375-379 (2013).

[47] ALICE Technical Design Report of the Transition Radiation Detector (TRD), 2001, CERN-LHCC-2001-021.

[48] I. Deppner, *Nucl. Instrum. Meth.* **A 661**, S121-S124 (2012).

[49] Yu. M. Zaitsev, et al., Atomic Energy, Vol. 112, No. 2, June, 2012.

[50] W. F. J. Muller, *Journal of Physics: Conference Series* **50**, 371-376 (2006).

[51] J de Cuveland and V Lindenstruth, *Journal of Physics: Conference Series* **331**,022006 (2011).

[52] G. Agakichiev et al., [CERES/NA45 Coll.], *Eur. Phys.J.* **C 41**, 475 (2005).

[53] R. J. Porter et al., [DLS Collaboration], *Phys. Rev. Lett.* **79**, 1229 (1997).

[54] A. Prakash, P. P. Bhaduri, S. Chattopadhyay, A. Dubey, B. K. Singh *Nuclear Physics A.* **862-863**, 493-496 (2011).

[55] S. A. Bass et. al., *Prog. Part and Nucl. Phys* **41**, 225 (1998).

[56] R. Brun et. al., GEANT3, *CERN/DD/EE/84-1*, 1986, long writeup *W5013*, (1993).

[57] M. Ryzhinskiy, http://cbm-wiki.gsi.de/cgi-bin/view/CbmRoot/CbmMuchDigi

[58] I. Kisel, *Nucl. Instr. and Meth.* **A 566**, 85 (2006).

[59] R. Kalman *Transactions of the ASME, Journal of Basic Engineering Series* **D 82**, 35 (1960).

[60] R. Fruhwirth, *Nucl. Instr. and Meth.* **A 262**, 444 (1987).

[61] C. Amstel, *The Review of Particle Physics, Phys. Lett.* **B 667** (2008).

[62] W. Press, Numerical Recipes: The Art of Scientific Computing , *Cambridge Unv Press* (2007).

[63] R. Fruhwirth et. al., Data analysis techniques in high energy physics, *Cambridge Univ Press* (2000).

[64] A. Lebedev and G. Ososkov, LIT track propagation for CBM , *CBM Note* (2008).

[65] http://www-hades.gsi.de/computing/pluto.

[66] http://fairroot.gsi.de.

[67] D. Bertini, M. Al-Turany, I. Koenig and F. Uhlig, *Journal of Physics: Conference Series* **119**, 032011 (2008).

[68] A. Prakash, P. P. Bhaduri, B. K. Singh, S. Chattopadhyay, *CBM Progress Report*, **ISBN 978-3-9811298-8-5**, 35 (2010).

[69] A. Prakash, P. P. Bhaduri, S. Chattopadhyay, B. K. Singh, *Proceedings of the DAE Symp. On Nucl. Phys.* **55**, 642 (2010).

[70] F. Sauli, Principles of Operation of Multiwire Proportional and Drift Chambers, CERN, Geneva **77-09** (1977).

[71] J. F. Ziegler, *J. App. Phys / Rev. App. Phys.* **85**, 1249-1272 (1999).

[72] C. Grupen, Teilchendetektoren (BI Wissenschaftsverlag, Mannheim, Leipzig, Zurich, 1993).

[73] S. Lotze, Ion Backdrift Minimisation in a GEM-Based TPC Readout, PhD Thesis. III. Physikalisches Institut, RWTH Aachen; http://darwin.bth. rwth-aachen.de/opus3/volltexte/2006/1499/ (2006).

[74] F. Sauli, GEM: A new concept for electron amplification in gas detectors.*Nucl. Instr. Meth.* **A 386**, 531 (1997).

[75] Kapton is a registered trademark of DuPont, Delaware, USA, (http://www2.dupont.com/Kapton/en_US/index.html). The chemical denotation of the material is Polyimid.

[76] Technology was developed by A. Gandi and R. DeOliveira, CERN-EST-MT

[77] B. Ketzer et al., A fast tracker for COMPASS based on the GEM. *Nucl. Phys.* B (Proc. Suppl.) **125C**, 368 (2003).

[78] F. Simon, Commissioning of the GEM Detectors in the COMPASS Experiment. Diploma Thesis, TU Munchen (2001).

[79] S. Bachmann et al, Charge Amplification and Transfer Processes in the Gas Electron Multiplier. *Nucl. Instr. Meth.* **A 438**, 376 (1999).

[80] S. D. Pinto and J. Spanggard, arXiv:1309.2908v1 [physics.ins-det] (2013)

[81] R. Veenhof, http://garfield.web.cern.ch/garfield/

[82] M. Deile et al., [TOTEM Collaboration] *JINST* **3 S08007** (2008).

[83] I. Tserruya, *Nuclear Instruments and Methods in Physics Research* **A 546**, 466-480 (2005).

[84] P. Abbon et al., *Nuclear Instruments and Methods in Physics Research* **A 577**, 455-518 (2007).

[85] https://na61.web.cern.ch/na61/xc/index.html?O=detector/GEM-detector

[86] ATLAS Collaboration, The ATLAS experiment at the CERN Large Hadron Collider, *J. Instrum.* **3**, S08003 (2008).

[87] M. Tytgat et al., *JINST* **8 C12031** (2013).

[88] ALICE Collaboration, The ALICE experiment at the CERN LHC. *J. Instrum.* **2**, S08002 (2008).

[89] C. Matteuzzi, [LHCb Collaboration] *JINST* **3 S08005** 2008.

[90] A.K. Dubey, A. Prakash, S. Chattopadhyay, M.S. Ganti, R. Singaraju, J. Saini, B.K. Singh, Y.P. Viyogi, *Nuclear Instruments and Methods in Physics Research* **A 718**, 418-420 (2013).

[91] A. K. Dubey, A. Prakash, J. Saini, R. Singaraju, Z. Ahammad, S. Chattopadhyay, G. S. N. Murthy, Y. P. Viyogi, B. K. Singh, *Proceedings of the DAE Symp. On Nucl. Phys.* **56**, 640 (2011).

[92] A.S. Brogna et al., *Nucl. Instr. and Meth.* **A 568**,301 (2006).

[93] M. Tytgat et. al., RD51-Note-2011-012(arXiv:1111.7249v1), F. Simon et.al. arxiv:0711.3751v1.

[94] C. P. Singh, *Phys. Rept.* **236**, 147 (1993).

[95] C. P. Singh, *Int. J. Mod. Phys.* **A 7**, 7185 (1992).

[96] H. Satz, *Int. J. Mod. Phys.* **E 21**, 1230006 (2012).

[97] A. Kumar, P. K. Srivastava, B. K. Singh, C. P. Singh, Advances in High Energy Physics (In press) 2013; A. Kumar, B. K. Singh, P. K. Srivastava, C. P. Singh, Eur. J. Phys. Plus 128, 45 (2013).

[98] B. Mohanty, *J. Phys.* **G 38**, 124023 (2011).

[99] L. Adamczyk et al., *Phys. Rev. Lett.* **110**, 142301 (2013).

[100] B. B. Back et al., *Nucl. Phys.* **A 757**, 28 (2005).

[101] A. Laszlo, *PoS(CPOD07)*, 054 (2007).

[102] F. Antinori et al., *J. Phys.* **G 37**, 045105 (2010).

[103] R. Singh, L. Kumar, P. K. Netrakanti, B. Mohanty, Advances in High Energy Physics 2013, 761474 (2013).

[104] P. Senger, *Progress in Particle and Nuclear Physics* **62**, 375-380 (2009) .

[105] S. Borsanyi et.al., *J. High Energy Phys.* **11**, 077 (2010) .

[106] S. Borsanyi et.al., *J. High Energy Phys.* **01**, 138 (2012) ; *J. Phys.* **G 29**, 275 (2008) .

[107] A. Andronic, P. Braun-Munzinger, and J. Stachel, *Nucl. Phys.* **A 772**, 167 (2006).

[108] J. Cleymans, H. Oeschler, and K. Redlich, *Phys. Lett.* **B 485**, 27 (2000).

[109] F. Becattini, J. Cleymans, A. Keranen, E. Suhonen, and K. Redlich, *Phys. Rev.* **C 64**, 024901 (2001).

[110] W. Broniowski and W. Florkowski, *Phys. Rev.* **C 65**, 064905 (2002).

[111] J. Y. Ollitrault, *Eur. J. Phys.* **29**, 275 (2008) .

[112] U. Heinz and R. Snellings, *Ann. Rev. Nucl. Part. Sci.* **63**, 123 (2013) and reference therein .

[113] S. K. Tiwari, P. K. Srivastava, C. P. Singh, *Phys. Rev.* **C 85**, 014908 (2012).

[114] P. K. Srivastava, C. P. Singh, *Phys. Rev.* **D 85**, 114016 (2012).

[115] P. K. Srivastava and C. P. Singh, *Int. J. Mod. Phys.* **A 28**, 1350051 (2013).

[116] S. K. Tiwari and C. P. Singh, Advances in High Energy Physics 2013, 805413 (2013).

[117] A. Prakash, P. K. Srivastava and B. K. Singh, Advances in High Energy Physics 2014, 983861 (2014).

[118] J. Randrup and J. Cleymans, *Phys. Rev.* **C 74**, 047901 (2006).

[119] V. V. Begun, M. Gazdzicki and M. I. Gorenstein, *Phys. Rev.* **C 88**, 024092 (2013).

[120] D. H. Rischke, M. I. Gorenstein, H. Stocker, and W. Greiner, *Z. Phys.* **C 51**, 485 (1991).

[121] S. K. Tiwari, P. K. Srivastava, C. P. Singh, *J. Phys.* **G 40**, 045102 (2013).

[122] C. Alt et al., *Phys. Rev.* **C 77**, 024903 (2008).

[123] C. Alt et al., *Phys. Rev.* **C 78**, 034918 (2008).

[124] A. Andronic et al., *Nucl. Phys.* **A 837**, 65 (2010).

[125] C. Blume, *J. Phys.* **G 31**, S685 (2005).

[126] S. V. Afanasiev et al., *Phys. Rev.* **C 66**, 054902 (2002).

[127] H. Weber, E. L. Bratkovskaya, W. Cassing and H. Stocker, *Phys. Rev.* **C 67**, 014904 (2003).

[128] M. Bleicher et al., *J. Phys.* **G 25**, 1859 (1999).

[129] N. Bianchi et al., *Phys. Lett.* **B 309**, 5 (1993).

[130] N. Bianchi et al., *Phys. Lett.* **B 325**, 333 (1994).

[131] N. Bianchi et al., *Phys. Rev.* **C 54**, 1688 (1996).

[132] J. Rafelski, *Nucl. Phys.* **A 418**, 215c (1984).

[133] C. P. Singh and S. Uddin, *Phys. Rev.* **D 41**, 870 (1990).

[134] V. K. Tiwari and C. P. Singh, *Phys. Lett.* **B 411**, 225 (1997).

[135] C. P. Singh, *Phys. Rev. Lett.* **56**, 1750 (1986).

[136] T. S. Biro, J. Zimanyi, *Phys. Lett.* **113 B**, 6 (1982).

[137] T. S. Biro, J. Zimanyi, *Nucl. Phys.* **A 395**, 525 (1983).

[138] S. Margetis, K. Safarik, O. V. Baillie, *Ann. Rev. Nucl. Part. Sci.* **50**, 299 (2000).

[139] S. Uddin, C. P. Singh, *Phys. Lett.* **B 278**, 357 (1992).

[140] V.Friese, *PoS(CPOD09)*,005 (2009).

[141] M. Wagner, A. B. Larionov, and U. Mosel, *Phys. Rev.* **C 71**, 034910 (2005).

[142] U. Heinz, P. R. Subramanian, W. Greiner, *Z. Phys.* **A 318**, 247 (1984); P. Koch, B. Muller, H. Stocker, W. Greiner, *Mod. Phys. Lett.* **A 3**, 737 (1988); J. Ellis, U. Heinz, H. Kowalski, *Phys. Lett.* **B 233**, 223 (1989).

[143] S. Gavin, M. Gyulassy, M. Plumer, R. Venugopalan, *Phys. Lett.* **B 234**, 175 (1990); H. Sorge, A. V. Keitz, R. Mattiello, H. Stocker, W. Greiner, *Z. Phys.* **C 47**, 629 (1990).

[144] A. Tawfik, *Nucl. Phys.* **A 859**, 63 (2011).

[145] A. Tawfik, *Int.J.Theor.Phys.* **51**, 1396-1407 (2012).

List of Publications

Peer reviewed papers included in the present thesis

1. *Particle Production at CBM in a Thermal Model Approach*
   A. Prakash, P. K. Srivastava, B. K. Singh
   Advances in High Energy Physics **2014**, 983861 (2014).

2. *GEM detector development for CBM experiment at FAIR*
   A. K. Dubey, **A. Prakash**, S. Chattopadhyay, M. S. Ganti , R Singaraju, J. Saini, B. K. Singh, Y. P. Viyogi
   Nucl. Inst. and Meth. A **718**, 418-420 (2013).

3. *Di-muon measurements in CBM experiment at FAIR*
   A. Prakash, P. P. Bhaduri, S. Chattopadhyay, A. Dubey, B. K. Singh
   Nuclear Physics A. **862-863**, 493-496 (2011).

Proceedings included in the present thesis

1. *Net baryon density at FAIR energies in a thermal model approach*
   A. Prakash, P. K. Srivastava, B. K. Singh and C. P. Singh
   CBM Progress Report, **ISBN 978-3-9815227-1-6**,124 (2014).

2. *Technical Design Report for the CBM, Muon Chamber (MUCH)*
   S. Chattopadhyay, V. P. Viyogi, A. K. Dubey, P .P. Bhaduri, **A. Prakash** et.al.
   Submitted for Review to ECE-FAIR, 1-183, (December, 2013).

3. *Testing of a triple-GEM chamber with muon beams at CERN SPS*
   A. K. Dubey, **A. Prakash**, J. Saini, R. Singaraju, Z. Ahammad, S. Chattopadhyay, G. S. N. Murthy, Y. P. Viyogi, B. K. Singh
   Proceedings of the DAE Symp. On Nucl. Phys. **57**, 860 (2012).

4. *Geometry optimization for dimuon detection system in CBM experiment at FAIR*
   A. Prakash, P. P. Bhaduri, S. Chattopadhyay, B. K. Singh
   Proceedings of the DAE Symp. On Nucl. Phys. **55**, 642 (2010).

5. *Segmentation optimization for the MUCH detector*
   A. Prakash, P. P. Bhaduri, B. K. Singh, S. Chattopadhyay
   CBM Progress Report, **ISBN 978-3-9811298-8-5**, 35 (2010).

6. *MUCH layout optimization for SIS-100*
   P. P. Bhaduri, **A. Prakash**, S. Chattopadhyay
   CBM Progress Report, **ISBN 978-3-9811298-8-5**, 34 (2010).

7. *Preliminary simulation results of THGEM geometry and detector gas for CBM muon detector*
   P. Garg, **A. Prakash**, V. Singh, C. P. Singh B. K. Singh
   CBM Progress Report, **ISBN 978-3-9811298-6-1**, 30 (2008).

Peer reviewed papers not included in the present thesis

1. *Characteristics of disintegration of different emulsion nuclei by relativistic 28 Si nuclei at 3.7 A GeV*
   Ashwini Kumar, **A. Prakash**, Ashok Kumar, R. K. Jain, B. K. Singh
   Accepted in *Pramana J. Phys.* (2014).

2. *Design of segmented-absorber based muon detection system for high energy heavy ion collision experiment*
   S. Ahmad, P. P. Bhaduri, H. Jahan, A. Senger, R. Adak, S. Samanta, **A. Prakash**, K. Dey, A. Lebedev, E. Kryshen, S. Chattopadhyay, P. Senger, B. Bhattacharjee, S. K. Ghosh, M. Irfan, N. Ahmad, M. Farooq, B. K. Singh.
   Submitted to *Nuc. Inst. and Meth. A* (2013).

3. *VUV-induced radiation ageing processes in CsI photocathodes studied by microscopy and spectroscopy techniques*
   B. K. Singh, Triloki, P. Garg, **A. Prakash**, G. Di Santo, E. Nappi, M.A. Nitti,A. Valentini, R. Zanoni
   Nucl. Inst. and Meth. A **610**, 350-353 (2009).

Proceedings not included in the present thesis

1. *First Level Event Selection for MUCH using GPU*
   V. Singhal, P. P. Bhaduri, **A. Prakash**, S. Chattopadhyay S. K. Aggarwal
   CBM Progress Report, **ISBN 978-3-9815227-0-9**, 97 (2012).

2. *Sector layout of Muon Chambers (MUCH): First results*
   Subhasis Chattopadhyay, P. P. Bhaduri, Z. Ahammed, **A. Prakash**
   Proceedings of the DAE Symp. On Nucl. Phys. **56**, 640 (2011).

3. *Development of a trigger algorithm for the measurement of rare probes in the CBM Experiment at FAIR*
   P. P. Bhaduri, S. Chattopadhyay, **A. Prakash**, B. K. Singh
   Proceedings of the DAE Symp. On Nucl. Phys. **55**, 640 (2010).